Karlsruhe Institute of Technology

Time-domain poroelastic full-waveform inversion of shallow seismic data

Zur Erlangung des akademischen Grades eines

Doktors der Naturwissenschaften (Dr. rer. nat.)

von der KIT-Fakultät für Physik
des Karlsruher Instituts für Technologie (KIT)

genehmigte

Dissertation

von

M.Sc. Tingting Liu

aus Heilongjiang, V.R. China

Tag der mündlichen Prüfung: 10. Februar 2023
Erster Gutachter: Prof. Dr. Thomas Bohlen
Zweiter Gutachter: Prof. Dr. Erik Hans Saenger

This document is licensed under a Creative Commons Attribution 4.0 International License (CC BY 4.0): https://creativecommons.org/licenses/by/4.0/deed.en

Abstract

Among seismic imaging methods, Full-waveform inversion (FWI) is a high-resolution imaging technique to recover the geophysical parameters of the elastic subsurface from the entire content of the seismic signals. However, the subsurface material properties are less well estimated with only elastic constraints, especially for the near-surface structure, which usually contains fluid contents. Along with the deep-going research on FWI, its performance prospects on complex media with multiple parameters are urging to be investigated. On another side, Biot's theories, which consider the stress from the solid skeleton and the fluid environment, can provide a framework to describe seismic wave propagation in the poroelastic medium.

In this thesis, a 2D time-domain (TD) Rayleigh/Love wave poroelastic FWI (PFWI) algorithm is proposed by applying the fluid-saturated poroelastic equations to carve the physical mechanism in the shallow subsurface. A FORTRAN inversion package $IforPoro$ is developed to conduct the numerical reconstruction tests. To detect the contribution of the poroelastic parameters to shallow seismic wavefields, the scattered P-SV&SH wavefields corresponding to a single model parameter are derived explicitly by Born approximation and shown numerically afterward. The Fréchet kernels are derived and exhibited in P-SV&SH schemes to analyze the sensitivities of the objective function to different poroelastic parameters. A series of numerical tests on gradients with respect to different model parameters are performed to evaluate inter-parameter trade-offs further. The derivations are verified by the mono-parameter PFWI reconstructions when the target model contains a porous anomaly and layered poroelastic medium. For multi-parameter PFWI tests, a cross-target model is set up with changing patterns of combined anomalies. Both Rayleigh and Love wave PFWI are numerically implemented for comparisons.

The results indicate that the fluid information (e.g., fluid density ρ_f, porosity ϕ) can be recovered directly by PFWI, which behaves with strong nonlinearity. The poroelastic model parameterization should only contain rock physical properties (e.g., elastic modulus, bulk modulus, density, etc.) instead of updating effective velocities, which are strongly coupled with parameters. For different target areas, model parameters can be split into groups that get similar benefits from wave information.

Contents

Abstract . . . i

Nomenclature . . . vii

I. Introduction 1

1. Background and Motivation . . . 3

2. Achievement and structure of this thesis . . . 5

II. Mathematical physics problems on poroelastic medium at seismic frequencies 7

3. The forward problem . . . 9
- 3.1. Equations of motion . . . 10
- 3.2. Constitutive equations . . . 11
- 3.3. Seismic wave propagation in shallow fluid-saturated poroelastic subsurface . . . 12
  - 3.3.1. Poroelastodynamic P-SV/SH equations in differential velocity-Stress format . . . 14
    - 3.3.1.1. P-SV wave equations . . . 15
    - 3.3.1.2. SH wave equations . . . 16
  - 3.3.2. Boundary conditions . . . 17
    - 3.3.2.1. C-PML boundary . . . 18
    - 3.3.2.2. Free-surface boundary . . . 18
- 3.4. Benchmarking . . . 20
  - 3.4.1. Benchmark tests for the 2D P-SV forward solver . . . 21
  - 3.4.2. Benchmark tests for the 2D SH forward solver . . . 29

4. The structural inverse problem . . . **31**
- 4.1. Computing the gradients with augmented functional . . . 32
  - 4.1.1. Gradients derivation in poroelastic PSV/Rayleigh wave equations . . . 33
  - 4.1.2. Gradients derivation in poroelastic SH/Love wave equations 37

4.2. Computing the gradients with perturbation theory 39
4.2.1. Gradients and first-order scattering pulses in poroelastic PSV/Rayleigh wave equations 40
4.2.2. Gradients and first-order scattering pulses in poroelastic SH/Love wave equations 43

III. Sensitivity analysis **45**

5. Single-scattering problem **47**
5.1. Analysis of scattered wavefield produced by individual model parameter perturbations 47

6. Sensitivity kernels **53**
6.1. Fréchet kernels K_λ, K_{K_s}, K_{K_f} involving Rayleigh waves 53
6.2. Comparison of Fréchet kernels in P-SV and SH equations 55

7. Trade-off analysis **57**
7.1. Correlation tests of gradient gallery in P-SV equations 58
7.2. Cross-comparison of gradient panels in PSV&SH equations 60

IV. Numerical reconstructions **63**

8. Mono-parameter poroelastic FWI **65**
8.1. Inclusion model 65
8.1.1. Inversion setup 66
8.1.2. Rayleigh wave PFWI results: λ, K_s, K_f 67
8.1.3. Reconstruction results comparison of Rayleigh and Love wave PFWI 67
8.1.4. Summary 69
8.2. Layered model 70
8.2.1. Inversion setup 70
8.2.2. Rayleigh wave PFWI results: λ, K_s, K_f 71
8.2.3. Reconstruction results comparison of Rayleigh and Love wave PFWI 72
8.2.4. Summary 76

9. Multi-parameter PFWI **77**
9.1. Rayleigh wave PFWI 80
9.1.1. Parameter set: λ, K_s, K_f, μ, ρ_s, ρ_f, ϕ 80

9.1.2. Parameter set: λ, K_s, K_f . . . 82
9.1.3. Parameter set: λ, K_s, K_f, ϕ . . . 83
9.1.4. Parameter set: μ, ρ_s, ρ_f, ϕ . . . 84
9.1.5. Parameter set: λ, μ, ϕ . . . 85
9.1.6. Summary . . . 86
9.2. Love wave PFWI . . . 86
9.2.1. Parameter set: μ, ρ_s, ρ_f, ϕ . . . 87
9.2.2. Parameter set: ρ_s, ρ_f, ϕ . . . 89
9.2.3. Parameter set: μ, ϕ . . . 90
9.2.4. Summary . . . 90

10. Comparison with EFWI . . . 91
10.1. Model setup . . . 91
10.2. Results comparison . . . 92

V. Summary 95

11. Conclusions . . . 97

12. Outlook . . . 99

Bibliography . . . 101

A. Effects on Fréchet kernels . . . 109
A.1. Effects of frequency . . . 109
A.2. Kernels with/without surface waves . . . 110

B. Gradients tapering . . . 111

C. Multi-stage strategy . . . 113

D. Reconstruction test with/without surface waves . . . 115

E. Effective velocities . . . 117

List of Figures . . . 119

List of Tables . . . 125

Acknowledgement . . . 127

Nomenclature

Abbreviations

$C - PML$	Convolutional perfectly matched layer
CTM	Cross-target model
$EFWI$	Elastic full-waveform inversion
FD	Finite-difference
FE	Finite-element
FWI	Full-waveform inversion
$PFWI$	Poroelastic full-waveform inversion
TD	Time-domain

Notations

α	Biot-Wills coefficient
$\delta \mathbf{s}'$	Scattering source
Δt	Time step
Δx	Spatial grid space in x direction
δ_{ij}	Kronecker delta
$\delta \mathbf{u}$	Scattered wavefields
$\delta \mathbf{u}^*$	Adjoint wavefields
$\dot{v}$	Time differentiation of v
ϵ	Strain tensor
η	Fluid viscosity
γ_k	Step length at iteration k
κ_0	Hydrological permeability
λ	Lamé constant, elastic modulus

$\mathbf{d}_{obs}$	Observed data
$\mathbf{H}_0$	Hessian matrix
$\mathbf{I}_n$	Identity matrix of order n
$\mathbf{L}$	Forward differential operator
$\mathbf{L}^*$	Adjoint operator
$\mathcal{J}$	Error functional
$\mathcal{L}$	Augmented functional
$\mathcal{M}$	Model space: $\mathbf{m} \in \mathcal{M}$
$\mathcal{U}$	Data space: $\mathbf{u} \in \mathcal{U}$
$\mathcal{U}^*$	Dual space of $\mathcal{U}$: $\Lambda^* \in \mathcal{U}^*$
μ	Lamé constant, shear modulus
ϕ	Porosity
ρ	Effective mass density
ρ_f	Fluid mass density
ρ_s	Solid grain density
σ_{ij}	Stress tensor
τ	Tortuosity
C	Stiffness tensor
D_t^+	Forward time operator
D_x^+	Forward space operator in x direction
D_t^-	Backward time operator
D_x^-	Backward space operator in x direction
$G_{\mathbf{m}}$	gradient of the model parameter $\mathbf{m}$
K	Fréchet kernel
K_d	Drained bulk modulus of the solid skeleton

K_f	Bulk modulus of the fluid content
K_s	Bulk modulus of the solid grain
K_u	Undrained bulk modulus
M	Fluid storage coefficient
P	Fluid pressure
V_s	Shear wave velocity
V_{fp}	Fast-P wave velocity
V_{sp}	Slow-P wave velocity

Part I.

Introduction

1

Background and Motivation

Seismic waves contain the elastodynamic responses of subsurface materials, which are widely applied in exploring the geologic structure and locating deposits of energy resources (e.g., oil, gas, minerals, etc.) (R. E. Sheriff and Geldart 1995). For the near-surface (usually < 30 meters) exploration, surface waves (e.g., Rayleigh waves propagating along the free surface of a semi-infinite medium and horizontally polarized Love wave) with intense energies also take part in the investigations of environmental and geotechnical properties (locating buried cultural features and fracture zones; characterization of the critical structures like cavity and tunnel, etc.) (Butler 2005; Robert E. Sheriff 2002). To transform artificially measured seismic data from the "data/image space" to the "model/object space", full-waveform inversion (FWI), which considers any wave propagation and is with a high spatial resolution up to half wavelength, supplies a formalism to straightforwardly update medium properties along the directions of their gradient vectors (A. Tarantola 1984; J. Virieux, Asnaashari, et al. 2017). The physical system underground can be described by various physical theories (e.g., acoustic assumption, elastodynamic equations with/without viscous attenuation, anisotropy theory, etc.) so that the forward wavefields are predicted and prepare priory information to solve the nonlinear inverse problem (Russell 1988; Albert Tarantola 2005).

To extend FWI into the application of seismic reservoir characterization, Queißer and Singh (2013) employ the Gassmann model to relate P-wave velocity with CO_2 saturation directly in order to estimate CO_2 storage (Gassmann 1951). Dupuy et al. (2016) adopt a two-step workflow based on acoustic FWI to estimate rock-physics properties by inverting the effective medium properties. Hu et al. (2021) attempt to link the elastic properties with different rock-physics models to recover fluid properties (e.g., porosity ϕ) through elastic FWI. However, the rock properties related to the fluid information from the fluid-filled subsurface are still poorly considered by the elastodynamic FWI. The near-surface sediments are usually unconsolidated and composed of solid and fluid components. How to exploit the fluid information directly from the seismic waveforms has still not attracted enough attention.

Over the past decades, Biot's theory (Biot 1956a,b; Biot and Willis 1957) has been widely used as a reliable model to govern the poroelastic response since they build a framework relating poroelastic parameters to the seismic wave properties (Masson, S. R. Pride, and Nihei 2006; Morency and Tromp 2008; Zhu and McMechan 1991). Morency, Luo, and Tromp (2009) present sensitivity kernels for specific parameterizations in the poroelastic model based on adjoint methods. De Barros (2012) introduce Biot's theory into frequency-domain FWI, which is limited to utilizing reflected waves. Q. Yang, Malcolm, et al. (2018) discuss the radiation patterns for different parameterizations in poroelastic media and implement several synthetic reconstruction tests based upon frequency-domain poroelastic FWI (Q. Yang and Malcolm 2020). However, it is still an open question for time-domain FWI to directly employ Biot's theory to describe the physical mechanism of the near-surface structure. When surface waves are involved, the recovery performance of poroelastic full-waveform inversion (PFWI) on multiple parameters, including fluid information, needs to be investigated further.

2

Achievement and structure of this thesis

This thesis aims to develop the poroelastic full-waveform inversion (PFWI) method and detect its reconstruction ability on the unconsolidated shallow subsurface containing fluid characteristics. For this purpose, I utilize low-frequency Biot's poroelastic theory to describe the physical mechanism in the sediments and build a PFWI framework concerning both Rayleigh and Love wave types. $IforPoro$, a basic time-domain PFWI program package is developed to realize numerical reconstruct tests.

Except for the introduction, there are 4 main parts in this thesis.

- **Part 1: Mathematical physics problems on poroelastic medium at seismic frequencies**

  In this part, I will mainly focus on explaining the methodologies. Chapter 3 introduces the fluid-saturated poroelastic P-SV&SH equations and shows the shallow-seismic wavefields numerically. To validate the modeling accuracy, a series of benchmark tests are also performed. Chapter 4 contains the main part of FWI, which is searching the iteration direction for various model parameters to achieve the global minimum. Both the gradients in P-SV&SH equations are derived.

- **Part 2: Sensitivity analysis**

  As preparation for multi-parameter PFWI, this part contains the sensitivity analysis of poroelastic parameters. In chapter 5, I numerically compare the PSV&SH scattered wavefields generated by single-scattering sources from different model parameters. Chapter 6 detects the waveform contributions to different model parameters by visualizing their sensitivity kernels separately. And further, in chapter 7, the correlations between gradients of different parameters in anomaly body are discussed and compared in PSV&SH cases, which help to explore the trade-off issues between parameters during multi-parameter PFWI.

Related work:

Liu, T. & Bohlen, T. (2022) Time-domain poroelastic full-waveform inversion of shallow seismic data: methodology and sensitivity analysis. *Geophysical Journal International*, Oxford University Press (OUP). doi:10.1093/gji/ggac414

- **Part 3: Numerical reconstructions**

  This part mainly contains the synthetic data reconstruction tests by mono&multi-parameter Rayleigh&Love wave PFWI. Chapter 8 contains the mono-parameter reconstructions of the poroelastic anomaly body and layered model. Chapter 9 shows multi-parameter PFWI results for cross-target models. In chapter 10, I implement SH/Love wave PFWI compared with the results from conventional SH/Love wave EFWI.

  Related work:

  Liu, T. & Bohlen, T. (2022) Mono-Parameter Poroelastic FWI for the Reconstruction of the Shallow-Seismic Data. Presented at the 83rd EAGE Annual Conference & Exhibition, European Association of Geoscientists & Engineers. doi:10.3997/2214-4609.202210532
  Liu, T. & Bohlen, T. Time-domain poroelastic full-waveform inversion of shallow seismic data: synthetic reconstructions. *In preparing for submission to Geophysical Journal International.*

- **Part 4: Summary**

  Conclusions are drawn in chapter 11, and chapter 12 contains some perspectives.

Part II.

Mathematical physics problems on poroelastic medium at seismic frequencies

3

The forward problem

The Earth is regarded as an integrity of the continuous mass in the fields of geophysics. The kinematics of motion and deformation governs the behavior of wave propagation in the subsurface. In the meanwhile, seismic waves can provide information about the structure and distribution of rock types. The dynamic response of seismic waves propagating in porous media is of interest in reservoir characterization and near-surface geophysics. Within continuum porous media mechanics, the deformable porous medium can be made of a solid skeleton and one or more partially/fully saturated fluids (e.g., gases and liquids) at different spatial scales, which are microscale, mesoscale, and macroscale, from experimentally scope to measurable world (Biot 1962; S. R. Pride, J. G. Berryman, and Harris 2004; White 1975). Unlike the previous work, which focuses on effective properties and fluid substitution when dealing with the fluid mechanism in a porous medium (James G. Berryman 1999; Gassmann 1951), Biot's theory (Biot 1956a,b) has been verified to employ the fundamental model governing the poroelastic response (Corapcioglu 1991; Steven R. Pride, Gangi, and Morgan 1992) within the continuum mechanics when the porous frame is fully saturated with fluid at the macroscopic scale (Carcione 2015).

In this chapter, the propagation of seismic waves in a fluid-saturated porous medium is described by Biot's theory at low frequencies under the assumptions (1) The porous material has well-defined porosity and the frame is mostly isotropic in bulk modulus, density, and permeability; (2) The liquid phase is continuous and the disconnected pores in solid do not contribute to the porosity; (3) The conditions are isothermal (ibid.). With the help of laws of motion and Newton's laws (section 3.1-3.2), the poroelastic forward problems related to surface waves are solved numerically by finite-difference (FD) method both in P-SV and SH schemes (section 3.3). In section 3.4, I present some benchmark tests to validate the accuracy of the numerical simulation package $IforPoro$ developed for this thesis.

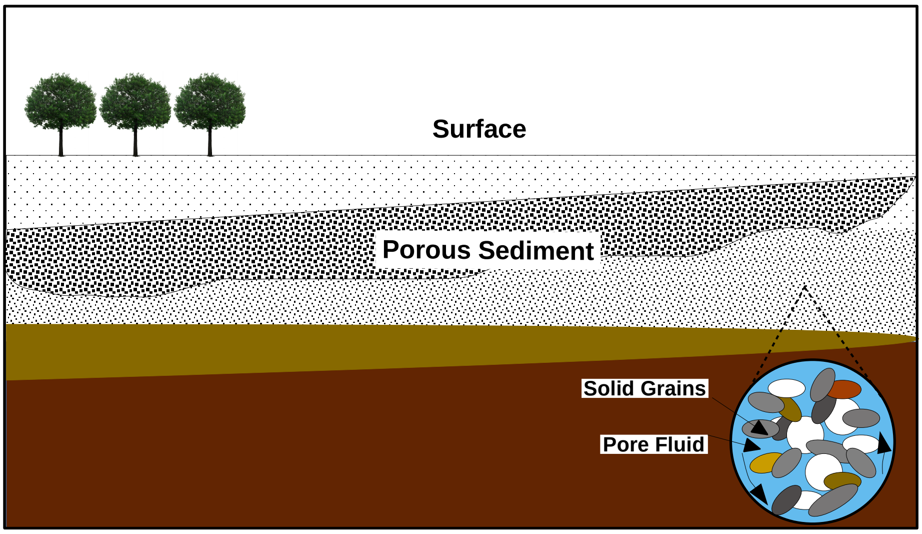

Figure 3.1.: Porous subsurface illustration

3.1. Equations of motion

The theory of poroelasticity is on the basis of the classical theory of elasticity. Following the steps of Biot's theory (Biot 1956a,b; Biot and Willis 1957), the macroscopic equations of motion (Eqs. 3.1-3.2) can describe the saturated solid-fluid system across the seismic band of frequencies. Within the Biot's characteristic frequency, the fluid flow regime is laminar and treated as Poiseuille type, where the internal drag forces on the solid/fluid interface are negligible.

$$\rho \dot{v}_i + \rho_f \dot{w}_i = \partial_j \sigma_{ij} \tag{3.1}$$

$$\rho_f \dot{v}_i + m \dot{w}_i = -\partial_i P - \frac{\eta}{\kappa_0} w_i, \quad \textbf{s.t.} \quad i, j \in [1, 3] \tag{3.2}$$

The dots above variables denote the time differentiation and Einstein notation is applied in the equations. The generalized Darcy's law is employed to explain the relative movement between the solid frame and fluid phase in this low-frequency band, and w_i is the Darcy filtration velocity (Eq. 3.3). v_i is the solid particle velocity. ϕ is the effective porosity of the porous medium and v^f is the fluid velocity. The mass coupling coefficient $m = \tau \rho_f / \phi$, where the tortuosity $\tau > 1$ is a dimensionless parameter concerns pore geometry (Ghanbarian et al. 2013). The average density ρ is comprised of the fluid density ρ_f and the solid particle density ρ_s (Eq. 3.4). η denotes the fluid viscosity and κ_0 is the hydrological permeability, which is a static permeability differs from the dynamic permeability (JKD) model (Johnson, Koplik, and Dashen 1987). The stress tensor σ_{ij} and fluid pressure P are formatted by Biot constitutive equations in section 3.2.

$$w_i = \phi(v_i^f - v_i) \tag{3.3}$$

The bulk density,

$$\rho = \rho_1 + \rho_2 = (1 - \phi)\rho_s + \phi\rho_f. \tag{3.4}$$

3.2. Constitutive equations

The generalized Hooke's law makes the elastic stress-strain relations as Eq. 3.5.

$$\sigma_{ij} = C_{ijkl}\epsilon_{kl}, \quad \textbf{s.t.} \quad i, j, k, l \in [1, 3], \tag{3.5}$$

where C_{ijkl} is the symmetrical stiffness tensor, while

$$C_{ijkl} = C_{klij} = C_{jikl} = C_{ijlk} \tag{3.6}$$

with 21 independent components. For isotropic media, the elasticity tensor can be represented by 2 independent parameters. The strain tensor

$$\dot{\epsilon}_{ij} = \frac{1}{2}(\partial_j v_i + \partial_i v_j). \tag{3.7}$$

When a porous medium saturated by a single-phase fluid is considered, the additional stress tensor from fluid phase

$$\sigma = -\alpha_{ij}P, \tag{3.8}$$

where α_{ij} is the Biot-Wills coefficient and the total tensor in poroelastic medium is

$$\sigma_{ij} = c_{ijkl}\epsilon_{kl} + \sigma\delta_{ij}, \tag{3.9}$$

where δ_{ij} is the Kronecker delta

$$\delta_{ij} = \begin{cases} 1 & i = j \\ 0 & i \neq j. \end{cases} \tag{3.10}$$

The fluid pressure

$$-\dot{P} = M_{ij}(\alpha_{ij}\partial_i v_i + \partial_i w_i). \tag{3.11}$$

For isotropic material,

$$\alpha_{ij} = \alpha = 1 - \frac{K_d}{K_s}, \tag{3.12}$$

and the fluid storage coefficient

$$M_{ij} = M = (\frac{\phi}{K_f} + \frac{\alpha - \phi}{K_s})^{-1}, \tag{3.13}$$

where K_s and K_f are the bulk moduli of solid grain and pore fluid, separately.

$$K_d = \lambda_d + \frac{2}{3}\mu \tag{3.14}$$

is the drained bulk modulus, and the undrained (saturated) bulk modulus

$$K_u = K_d + \alpha^2 M. \tag{3.15}$$

Similarly, the undrained Lamé modulus

$$\lambda_u = \lambda_d + \alpha^2 M, \tag{3.16}$$

where $\lambda_d = \lambda$ in elastic equations. The drained shear modulus μ_d and the undrained shear modulus μ_u are postulated to be equal (= μ) when the fluid has no influence on shear rigidity. Then for isotropic porous medium, the stress-strain relation is

$$\dot{\sigma}_{ij} = \lambda \delta_{ij} \nabla \cdot \mathbf{v} + 2\mu \dot{\epsilon}_{ij} - \alpha \dot{P} \delta_{ij}. \tag{3.17}$$

The external source term has not been specified in the equations above. Since the fluid phase is also considered in the poroelasticity equations, there are three ways of source applications (Carcione, Morency, and Santos 2010). (1) The source is partitioned between solid and fluid phases. (2) The source is applied in the solid. (3) The source is applied in the fluid. In the following numerical experiments, the solid source is considered only.

3.3. Seismic wave propagation in shallow fluid-saturated poroelastic subsurface

In previous work, Biot equations and their extensions have been numerically solved by different methods, e.g., finite-difference (FD) (Masson, S. R. Pride, and Nihei 2006), finite-element (FE) (Santos and Sheen 2007) and spectral finite-elements methods (Morency and Tromp 2008). Among these numerical modeling techniques, the explicit finite-difference methods have been widely used as a straightforward way to directly discretize the arbitrary geological model in a finite number of grids (Thomas Bohlen 2002; Carcione, Herman, and Kroode 2002). In this section, seismic wave propagation in 2D isotropic fluid-saturated porous media will be numerically simulated by the staggered-grid FD method, which is an essential part of the following seismic inversion algorithms. To be noticed, surface waves such as Rayleigh waves and Love waves are also involved in shallow-seismic studies.

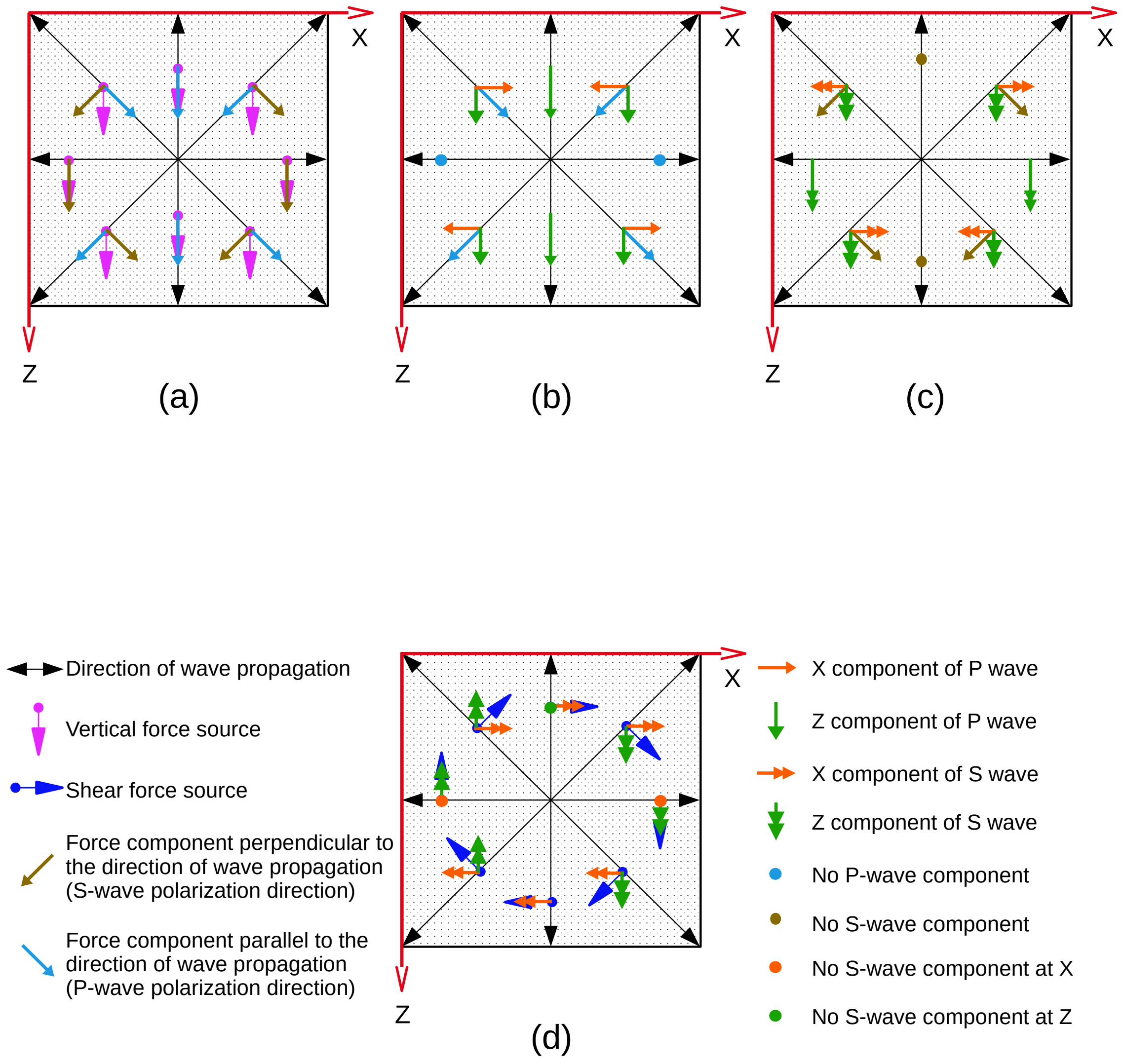
X
Z
(a)
X
Z
(b)
X
Z
(c)
Direction of wave propagation
Vertical force source
Shear force source
Force component perpendicular to the direction of wave propagation (S-wave polarization direction)
Force component parallel to the direction of wave propagation (P-wave polarization direction)
X
Z
(d)
X component of P wave
Z component of P wave
X component of S wave
Z component of S wave
No P-wave component
No S-wave component
No S-wave component at X
No S-wave component at Z

Figure 3.2.: Implementation of different source types

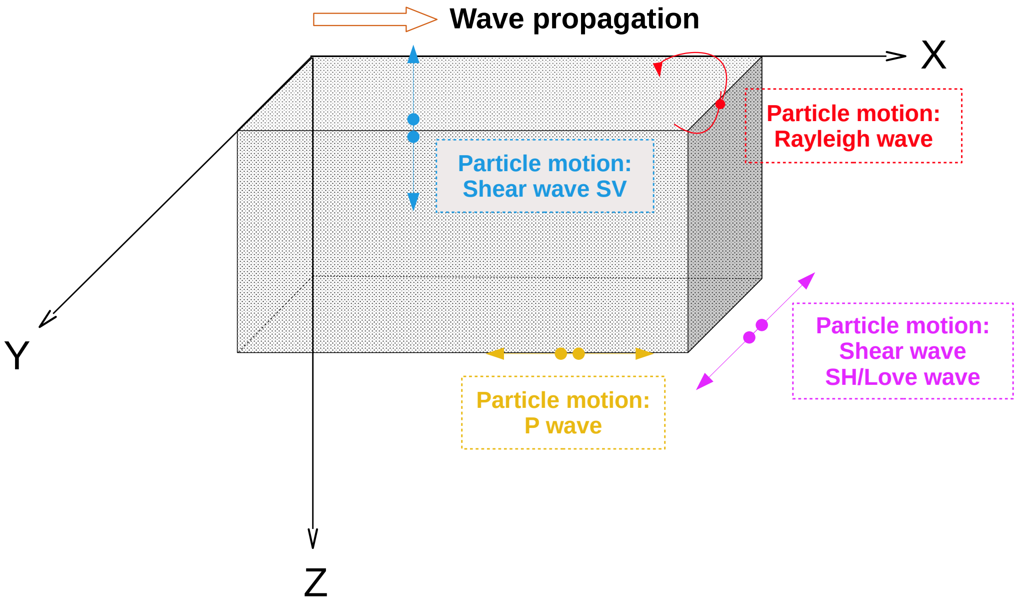
Wave propagation
X
Y
Z
Particle motion: Rayleigh wave
Particle motion: Shear wave SV
Particle motion: Shear wave SH/Love wave
Particle motion: P wave

Figure 3.3.: Cartesian coordinate system and surface waves

3.3.1. Poroelastodynamic P-SV/SH equations in differential velocity-Stress format

Based on section 3.1 and 3.2, 2D poroelastic forward velocity-stress formulations are summarized and discretized in the Cartesian coordinate (Fig. 3.3). Except for seismic body waves (longitudinal waves and shear waves), surface waves will travel along and below the fluid(or air)/solid interface with rolling and side-to-side movements when the free-surface boundary is considered.

Similar to the elastic case, the poroelastic P-SV&SH wavefield variables are distributed on a standard staggered grid in Figs. 3.4 and 3.5, respectively (J. Virieux 1984; Jean Virieux 1986). For a continuous function $f(x)$, the 4th order Taylor staggered forward space operator D_x^+ and backward operator D_x^- are shown in equations (3.18) and (3.19) (Levander 1988).

$$\left.\frac{\partial f(x)}{\partial x}\right|_{(i+1/2)\Delta x} \approx D_x^+[f(i)] = \frac{1}{24\Delta x}[-f(i+2)+27(f(i+1)-f(i))+f(i-1)], \quad (3.18)$$

$$\left.\frac{\partial f(x)}{\partial x}\right|_{(i-1/2)\Delta x} \approx D_x^-[f(i)] = \frac{1}{24\Delta x}[-f(i+1)+27(f(i)-f(i-1))+f(i-2)], \quad (3.19)$$

where Δx is the spatial grid space and $i^+ = (i+1/2)\Delta x$, $i^- = (i-1/2)\Delta x$. Similarly, the 2nd-order forward and backward Taylor coefficients in time are shown in

Eqs. (3.20) and (3.21), separately. n is the time index, while $n^+ = (n + 1/2)\Delta t$, $n^- = (n - 1/2)\Delta t$. Δt is the time interval.

$$D_t^+[f(n)] = \frac{1}{\Delta t}[f(n+1) - f(n)] \tag{3.20}$$

$$D_t^-[f(n)] = \frac{1}{\Delta t}[f(n) - f(n-1)] \tag{3.21}$$

In the staggered-grid differential scheme, the neighboring model parameters need to be averaged in order to smooth the boundary effects. For any parameter p at a half grid point, it follows the rules

$$p_{i+,k} = \frac{1}{2}(p_{i,k} + p_{i+1,k}), \tag{3.22}$$

$$p_{i,k+} = \frac{1}{2}(p_{i,k} + p_{i,k+1}), \tag{3.23}$$

$$p_{i+,k+} = \frac{1}{4}(p_{i,k} + p_{i,k+1} + p_{i+1,k} + p_{i+1,k+1}). \tag{3.24}$$

3.3.1.1. P-SV wave equations

The explicit differential format of 2nd order in time and 4th order in space P-SV poroelastic equations is shown below. i, j, k represent spatial space (x, y, z), respectively.

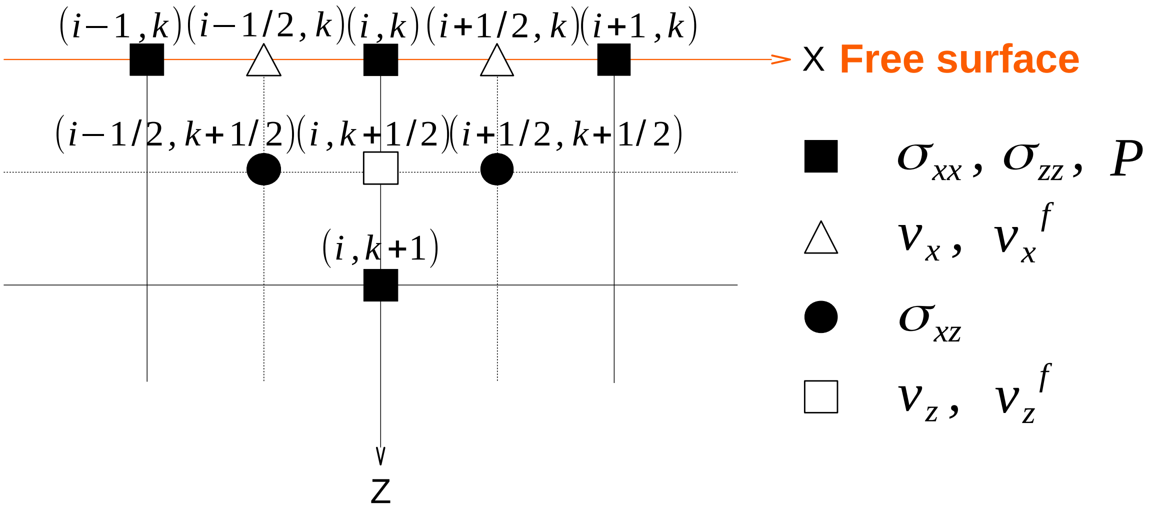
(i−1,k)(i−1/2,k)(i,k)(i+1/2,k)(i+1,k)
X Free surface
(i−1/2,k+1/2)(i,k+1/2)(i+1/2,k+1/2)
(i,k+1)
Z
■ σ_{xx}, σ_{zz}, P
△ v_x, v_x^f
● σ_{xz}
□ v_z, v_z^f

Figure 3.4.: Staggered grid and spatial position of variables in P-SV poroelastic equations

For velocities,

$$\begin{aligned}\frac{(v_x)^{n^+}_{i^+,k} - (v_x)^{n^-}_{i^+,k}}{\Delta t} &= (A\phi m)_{i^+,k}(D_x^+[(\sigma_{xx})^n_{i,k}] + D_z^-[(\sigma_{xz})^n_{i^+,k^+}]) \\ &\quad +(A\rho_2)_{i^+,k}D_x^+[P^n_{i,k}],\end{aligned} \tag{3.25}$$

$$\begin{aligned}\frac{(v_x^f)^{n^+}_{i^+,k} - (v_x^f)^{n^-}_{i^+,k}}{\Delta t} &= [-A(\rho_f - \phi m)]_{i^+,k}(D_x^+[(\sigma_{xx})^n_{i,k}] + D_z^-[(\sigma_{xz})^n_{i^+,k^+}]) \\ &\quad -(A\rho_1)_{i^+,k}D_x^+[P^n_{i,k}],\end{aligned} \tag{3.26}$$

$$\begin{aligned}\frac{(v_z)^{n^+}_{i,k^+} - (v_z)^{n^-}_{i,k^+}}{\Delta t} &= (A\phi m)_{i,k^+}(D_x^-[(\sigma_{xz})^n_{i^+,k^+}] + D_z^+[(\sigma_{zz})^n_{i,k}]) \\ &\quad +(A\rho_2)_{i,k^+}D_z^+[P^n_{i,k}],\end{aligned} \tag{3.27}$$

$$\begin{aligned}\frac{(v_z^f)^{n^+}_{i,k^+} - (v_z^f)^{n^-}_{i,k^+}}{\Delta t} &= [-A(\rho_f - \phi m)]_{i,k^+}(D_x^-[(\sigma_{xz})^n_{i^+,k^+}] + D_z^+[(\sigma_{zz})^n_{i,k}]) \\ &\quad -(A\rho_1)_{i,k^+}D_z^+[P^n_{i,k}].\end{aligned} \tag{3.28}$$

For stresses,

$$\frac{(\sigma_{xx})^n_{i,k} - (\sigma_{xx})^{n-1}_{i,k}}{\Delta t} = (\lambda + 2\mu)_{i,k}D_x^-[(v_x)^{n^-}_{i^+,k}] + \lambda_{i,k}D_z^-[(v_z)^{n^-}_{i,k^+}] - \alpha_{i,k}D_t^-[P^n_{i,k}], \tag{3.29}$$

$$\frac{(\sigma_{zz})^n_{i,k} - (\sigma_{zz})^{n-1}_{i,k}}{\Delta t} = \lambda_{i,k}D_x^-[(v_x)^{n^-}_{i^+,k}] + (\lambda + 2\mu)_{i,k}D_z^-[(v_z)^{n^-}_{i,k^+}] - \alpha_{i,k}D_t^-[P^n_{i,k}], \tag{3.30}$$

$$\frac{(\sigma_{xz})^n_{i^+,k^+} - (\sigma_{xz})^{n-1}_{i^+,k^+}}{\Delta t} = \mu_{i^+,k^+}(D_z^+[(v_x)^{n^-}_{i^+,k}] + D_x^+[(v_z)^{n^-}_{i,k^+}]). \tag{3.31}$$

For fluid pressure,

$$\begin{aligned}-\frac{P^n_{i,k} - P^{n-1}_{i,k}}{\Delta t} &= (\phi M)_{i,k}(D_x^-[(v_x^f)^{n^-}_{i^+,k}] + D_z^-[(v_z^f)^{n^-}_{i,k^+}]) \\ &\quad +[(\alpha - \phi)M]_{i,k}(D_x^-[(v_x)^{n^-}_{i^+,k}] + D_z^-[(v_z)^{n^-}_{i,k^+}]).\end{aligned} \tag{3.32}$$

Apart from $A = 1/(\rho_f(\tau\rho - \phi\rho_f))$, most of the parameters have been explained in sections 3.1 and 3.2.

3.3.1.2. SH wave equations

As shown in Fig. 3.3, the particle displacement of SH- and Love waves is perpendicular to the x-z plane. In the 2D x-z plane, the main stress σ_{yy} is excluded and the fluid pressure will play no effects on the shear stress as well. Similar to P-SV equations, the differential format of SH poroelastic wave equations is as follows.

For velocity,

$$\frac{(v_y)^{n^+}_{i,k} - (v_y)^{n^-}_{i,k}}{\Delta t} = (A\phi m)_{i,k}(D_x^-[(\sigma_{xy})^n_{i^+,k}] + D_z^-[(\sigma_{yz})^n_{i,k^+}]). \tag{3.33}$$

For shear stresses,

$$\frac{(\sigma_{xy})^n_{i^+,k} - (\sigma_{xy})^{n-1}_{i^+,k}}{\Delta t} = \mu_{i^+,k} D_x^+[(v_y)^{n^-}_{i,k}], \tag{3.34}$$

$$\frac{(\sigma_{yz})^n_{i,k^+} - (\sigma_{yz})^{n-1}_{i,k^+}}{\Delta t} = \mu_{i,k^+} D_z^+[(v_y)^{n^-}_{i,k}]. \tag{3.35}$$

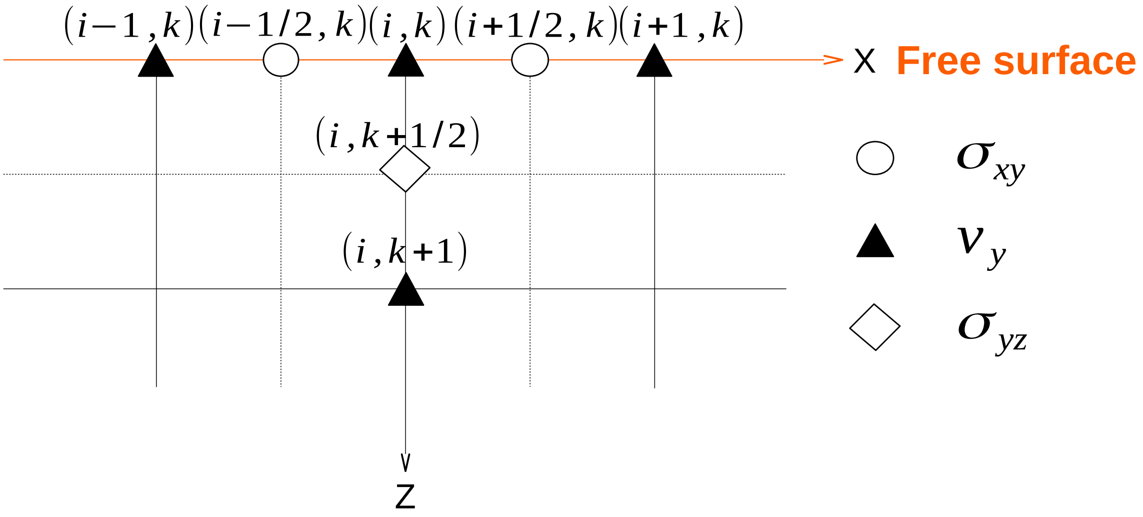

Figure 3.5.: Staggered grid and spatial position of variables in SH poroelastic equations

3.3.2. Boundary conditions

In the case of the numerical modeling is performed in a finite domain with a Dirichlet boundary condition, the reflected energies from the artificial boundaries need to be absorbed during the wave propagation. Among the previous techniques, the unsplit convolutional perfectly matched layer (C-PML) has been developed and implemented to efficiently absorb outgoing waves researching the boundaries in various medium (Berenger 1994; Cerjan et al. 1985; Collino and Tsogka 2001; Komatitsch and Martin 2007; Martin, Komatitsch, and Ezziani 2008; Zeng, He, and Q. H. Liu 2001). For a shallow 2D target area, there are three model boundaries except for the free-surface interface on the top.

3.3.2.1. C-PML boundary

In the finite-difference code, each spatial derivative ∂_X will be replaced by $\partial_{\tilde{X}}$ when

$$\partial_{\tilde{X}} = \frac{1}{\kappa_X}\partial_X + \psi_X, \quad \textbf{s.t.} \quad X \in \{x, y, z\}, \tag{3.36}$$

where ψ_X is a memory variable governed by Eq. (3.37),

$$\psi_X^n = b_X \psi_X^{n-1} + a_X(\partial_X)^{n+\frac{1}{2}}, \tag{3.37}$$

with

$$b_X = e^{-(\frac{d_X}{\kappa_X}+\alpha_X)\Delta t}, \tag{3.38}$$

and

$$a_X = \frac{d_X}{\kappa_X(d_X + \kappa_X \alpha_X)}(b_X - 1), \tag{3.39}$$

where $\alpha_X(\geq 0)$ and $\kappa_X(\geq 0)$ are real variables. For example, the classical PML coordinate transformation is represented when $\kappa_X = 1$ and $\alpha_X = 0$ (Komatitsch and Martin 2007). For the damping profile d_X,

$$d_X = d_0(\frac{X}{\delta})^N, \tag{3.40}$$

and

$$d_0 = log(\frac{1}{R})\frac{(N+1)V_{max}}{2\delta}, \tag{3.41}$$

where R is the theoretical reflection coefficient and can be set as a certain value. δ is the width of the absorbing layer. V_{max} represents the maximum velocity reaching the boundaries, which can be approximated as the fast compressional wave velocity in a poroelastic medium. When the damping profile parameter $N = 2$, Eq. (3.40) is a classical second-order damping function.

3.3.2.2. Free-surface boundary

At the boundary of the air-earth, the surface is free from external stress, which means the tractions perpendicular to the surface are zero. This so-called traction-free condition will lead to the presence of Raylaigh-type surface wave from P-SV elastic equations and Love-type surface wave from SH elastic equations (Aki and

Richards 1980; Igel 2016). In $x - z$ coordinate plane, this free-surface boundary satisfy

$$\sigma_{ij} = 0, \qquad (i = \{1,2,3\} \equiv \{x,y,z\}, j = 3 \equiv z). \tag{3.42}$$

Since the shallow subsurface mainly consists of unconsolidated materials, the air-earth interface is possibly under pervious circumstances so that the porous frame is drained with an open-pore system (Deresiewicz 1960; Tajuddin 1984). In the absence of dissipation ($\eta = 0$), the fluid pressure at the free surface will satisfy

$$P = 0. \tag{3.43}$$

The efficient implementation of the free surface is the key to generating surface waves during numerical modeling. Basically, there are mainly three ways of implementation. (1) Vacuum formalism, which tries to apply a vacuum or air layer at the top of the model straightforwardly. Nevertheless, it seems unstable when dealing with higher order (> 2) spatial FD operators (Groos 2013; Zahradník and Priolo 1995). (2) Classical stress image method, which follows the rules in Eq. (3.44), where N represents the spatial differential order and f_0 gives the grid number of the free surface location. i is defined as any integer grid number.

$$\begin{gathered}
\begin{cases}(\sigma_{zz})_{i,f_0} = 0\\ (\sigma_{zz})_{i,f_0-k} = -(\sigma_{zz})_{i,f_0+k}\end{cases} \quad \begin{cases}P_{i,f_0} = 0\\ P_{i,f_0-k} = -P_{i,f_0+k}\end{cases}\\
\begin{cases}(\sigma_{xz})_{i,f_0} = 0\\ (\sigma_{xz})_{i,f_0+\frac{1}{2}-k} = -(\sigma_{xz})_{i,f_0+\frac{1}{2}+k}\end{cases} \quad \begin{cases}(\sigma_{yz})_{i,f_0} = 0\\ (\sigma_{yz})_{i,f_0+\frac{1}{2}-k} = -(\sigma_{yz})_{i,f_0+\frac{1}{2}+k}\end{cases}\\
k = 1, \ldots, N/2,
\end{gathered} \tag{3.44}$$

$(\sigma_{xx})_{i,f_0}$ will be further calculated under the above rules (Levander 1988; Y. Zhang, Ping, and S.-X. Zhang 2017). Apparently, $\sigma_{iz}, i \in \{x,y,z\}$ and P are odd functions with respect to the free surface, and there is an artificial exterior domain above the free surface. (3) Air-earth boundary implementation by transversely isotropic (TI) medium using the long-wavelength approximation (Mittet 2002), which is further modified by explicit acoustic-elastic boundary approach (Xu, Xia, and Miller 2007). The concept of this method is to modify material properties on the free surface nodes, which is easily implemented in the FD scheme. However, this method appears to be less accurate for surface waves (e.g., Rayleigh waves) modeling. Overall, the stress image method can achieve good accuracy, especially for surface wave modeling with at least nine grid points per minimum wavelength in the 4th-order ($O(2,4)$) staggered-grid scheme (Thomas Bohlen and Saenger 2006). For a planar free surface, the stress image method is also further combined by vertically refining grids near the free surface, which makes no use of virtual grids above the free surface and can simulate surface waves accurately (Kristek, Moczo, and Archuleta 2002). In this work, I take advantage of this modified method to implement free surface in FD schemes ($O(2,4)$).

For the staggered-grid schemes in Figures 3.4 and 3.5 (H formulation, main stresses are set at the integer grids), except for following the rules in Eq. (3.44), the adjusted 4th-order finite-difference approximations to the z-derivatives are summarized below.

For calculations of $\frac{\partial \sigma_{xz}}{\partial z}$ and $\frac{\partial \sigma_{yz}}{\partial z}$ at the free-surface grid location f_0,

$$\begin{aligned} f'(z_0) \approx \frac{1}{\Delta z}[-\frac{352}{105}f(z_0) + \frac{35}{8}f(z_0+\frac{1}{2}\Delta z) \\ -\frac{35}{24}f(z_0+\frac{3}{2}\Delta z) + \frac{21}{40}f(z_0+\frac{5}{2}\Delta z) - \frac{5}{56}f(z_0+\frac{7}{2}\Delta z)]. \end{aligned} \tag{3.45}$$

For calculations of $\frac{\partial \sigma_{zz}}{\partial z}$, $\frac{\partial P}{\partial z}$, $\frac{\partial v_x}{\partial z}$, $\frac{\partial v_y}{\partial z}$, $\frac{\partial v_x^f}{\partial z}$ at the depth of half grid,

$$\begin{aligned} f'(z_0) \approx \frac{1}{\Delta z}[-\frac{11}{12}f(z_0-\frac{1}{2}\Delta z) + \frac{17}{24}f(z_0+\frac{1}{2}\Delta z) \\ +\frac{3}{8}f(z_0+\frac{3}{2}\Delta z) - \frac{5}{24}f(z_0+\frac{5}{2}\Delta z) + \frac{1}{24}f(z_0+\frac{7}{2}\Delta z)]. \end{aligned} \tag{3.46}$$

For calculations of $\frac{\partial v_z}{\partial z}$ and $\frac{\partial v_z^f}{\partial z}$ at the depth of one grid,

$$\begin{aligned} f'(z_0) \approx \frac{1}{\Delta z}[-\frac{1}{22}\Delta z f'(z_0-\Delta z) - \frac{577}{528}f(z_0-\frac{1}{2}\Delta z) \\ +\frac{201}{176}f(z_0+\frac{1}{2}\Delta z) - \frac{9}{176}f(z_0+\frac{3}{2}\Delta z) + \frac{1}{528}f(z_0+\frac{5}{2}\Delta z)], \end{aligned} \tag{3.47}$$

and for calculations of $\frac{\partial \sigma_{xz}}{\partial z}$, and $\frac{\partial \sigma_{yz}}{\partial z}$ at the depth of one grid,

$$\begin{aligned} f'(z_0) \approx \frac{1}{\Delta z}[\frac{16}{105}f(z_0-\Delta z) - \frac{31}{24}f(z_0-\frac{1}{2}\Delta z) \\ +\frac{29}{24}f(z_0+\frac{1}{2}\Delta z) - \frac{3}{40}f(z_0+\frac{3}{2}\Delta z) + \frac{1}{168}f(z_0+\frac{5}{2}\Delta z)]. \end{aligned} \tag{3.48}$$

3.4. Benchmarking

In order to represent the fluctuations aroused from the earth's properties on seismic data theoretically, the usefulness and accuracy of the numerical modeling on wavefields are vital for both the forward solver and inversion methods afterward. In this section, several benchmark tests were performed with the help of the code *IforPoro* to validate the accuracy of the forward modeling algorithm adopted in this thesis, especially to make sure to model surface waves in shallow poroelastic subsurface accurately. *IforPoro* is a developing FORTRAN 90 package to implement 2D P-SV/SH poroelastic FWI including surface waves with the FD method in the time domain. All the numerical results obtained from *IforPoro* for benchmark tests are calculated under a 2nd-order in time and 4th-order in space accuracies ($O(2,4)$) with staggered-grid schemes.

3.4.1. Benchmark tests for the 2D P-SV forward solver

When a traction-free surface is considered, the analytical solutions of the fluid-saturated poroelastic equations become more complicated. To validate the accuracy of the poroelastic forward solver in modeling shallow seismic wavefields, the concepts here are following two steps. Firstly, I simplify the poroelastic equations into the elastic case and make sure the numerical results are consistent with the elastic analytical solutions and the free surface condition is implemented correctly, in case surface waves (Rayleigh waves in the P-SV scheme) are simulated precisely. The analytical solution code is described by Berg et al. 1994 (`http://www.spice-rtn.org/library/software/EX2DVAEL.html`). Since the free boundary is initiatively satisfied in the numerical solutions of finite-element methods with flexible nodes (Caprili 1983), secondly, I compare the numerical results obtained from *IforPoro* and *SPECFEM2D* (Tromp, Komatitsch, and Q. Liu 2008, `https://geodynamics.org/`) when solving fluid-saturated poroelastic equations in a homogeneous half-space.

Model size (m^2)	**Source type**	**Central frequency (Hz)**
30×60	Vertical point	20
$\rho(kg/m^3)$	$V_p(m/s)$	$V_s(m/s)$
2200	500	280

Table 3.1.: Modeling parameters used for elastic benchmarking in section 3.4.1. The source signal is Ricker wavelet.

Table 3.1 contains the model parameters for the elastic benchmark tests. Fig. 3.7 shows the shallow-seismic elastic wavefields calculated by *IforPoro*. The source is located at the free surface and the width of the C-PML boundary is 10 meters. Fig. 3.6 gives seismogram comparisons in Z and X directions, which shows that the numerical results are in good agreement with the analytical solutions. In order to quantify the relative difference between the numerical and analytical solutions in Fig. 3.6, the L2 norm errors varied with offset and ppw number are calculated as well and shown in Fig. 3.8. The L2 norm error is calculated by Eq. 3.49, where q is the analytical solution and l is the time point (Thomas Bohlen and Saenger 2006).

$$E = \frac{\sum_{l=1}^{N}(f(l\Delta t) - q(l\Delta t))^2}{\sum_{l=1}^{N} q(l\Delta t)^2} \tag{3.49}$$

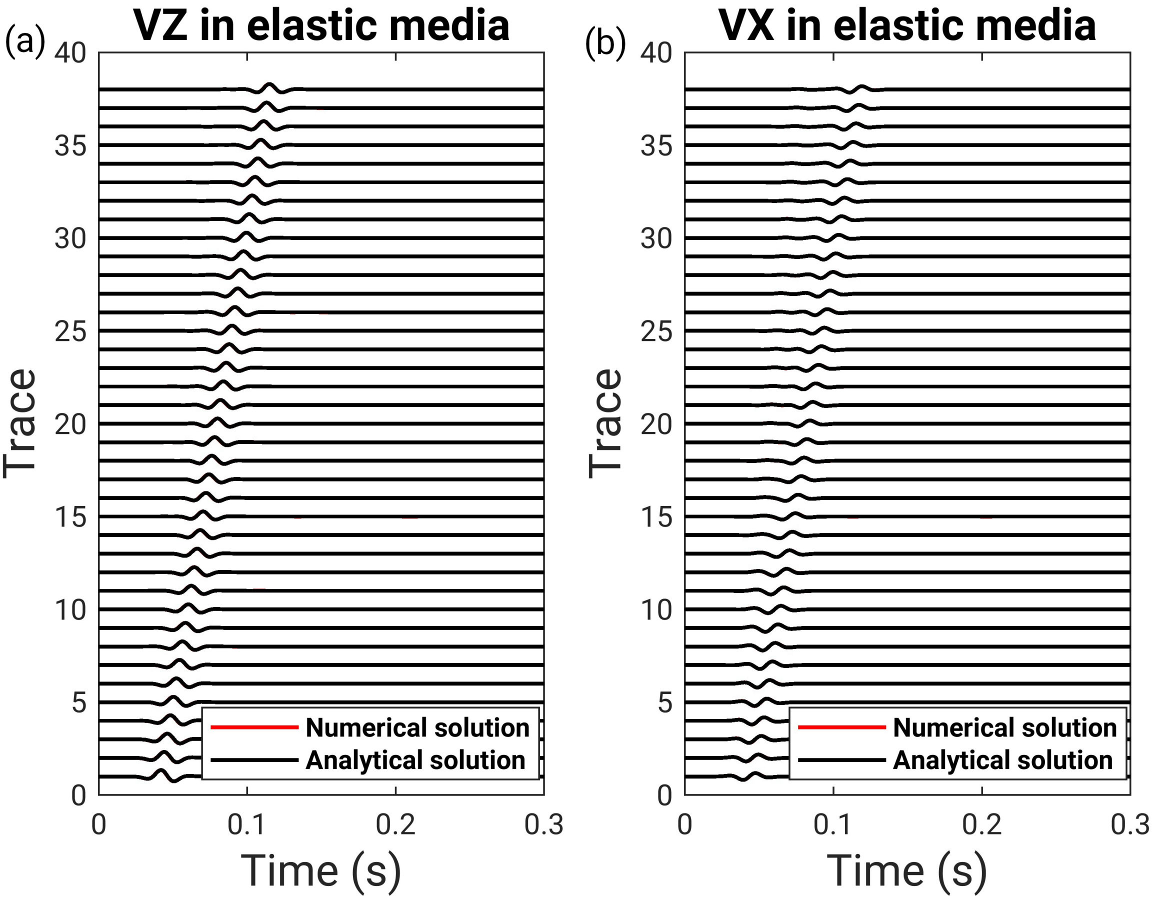

Figure 3.6.: Waveform comparisons of the synthetic data (in Fig. 3.7) and analytical solution of elastic wave equations. (a) Solid vertical velocity; (b) Solid horizontal velocity.

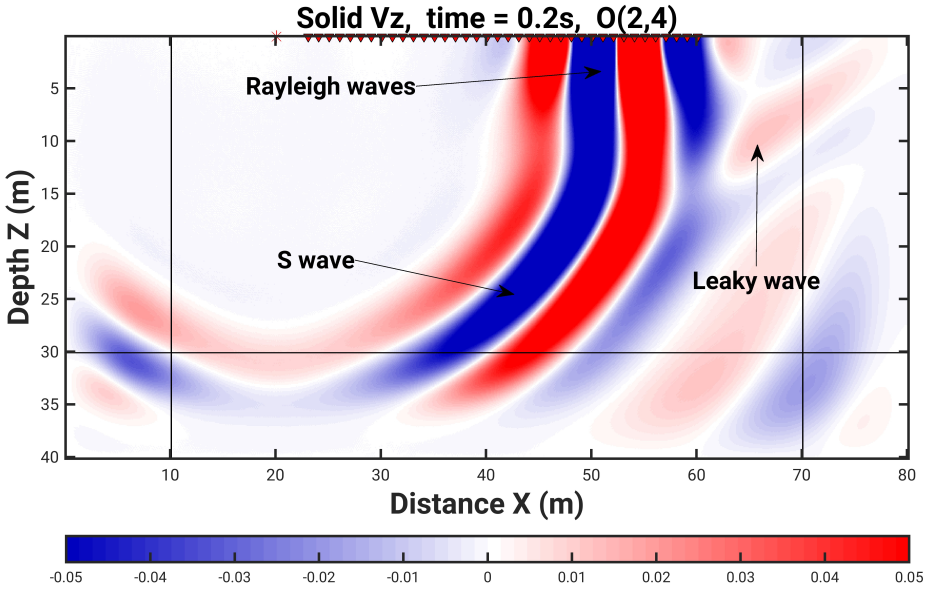

(a) Solid velocity in direction Z

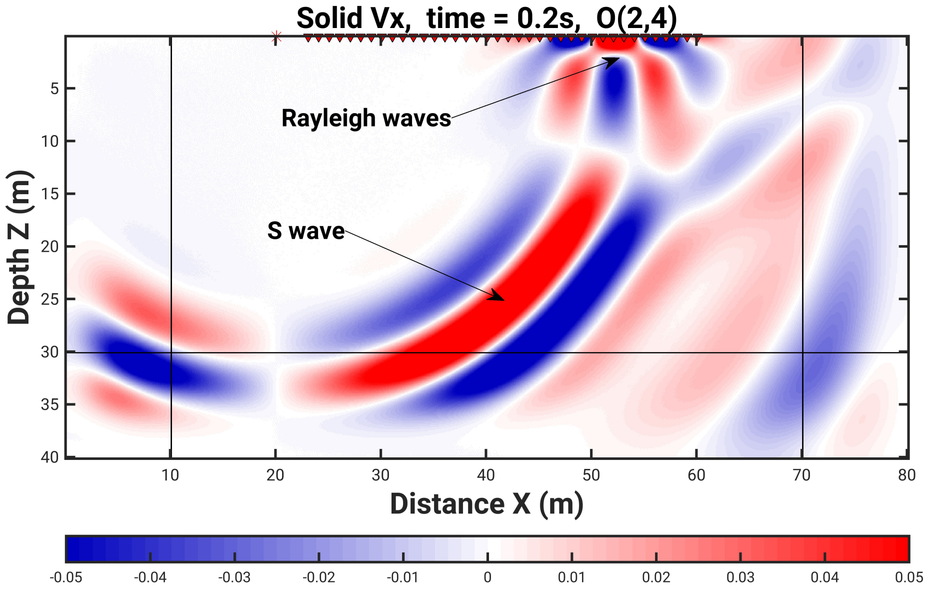

(b) Solid velocity in direction X

Figure 3.7.: Snapshots of the shallow-seismic wavefields in homogeneous elastic subsurface when the point per minimum wavelength number is 56. The red cross is the source location and the inverted triangles are 38 receivers.

Fig. 3.8 illustrates that the numerical accuracy will increase when the wavelength is finer defined by space grids. The minimum relative errors between numerical and analytical solutions will be below 1‰, which proves that *IforPoro* can give accurate results for modeling surface waves.

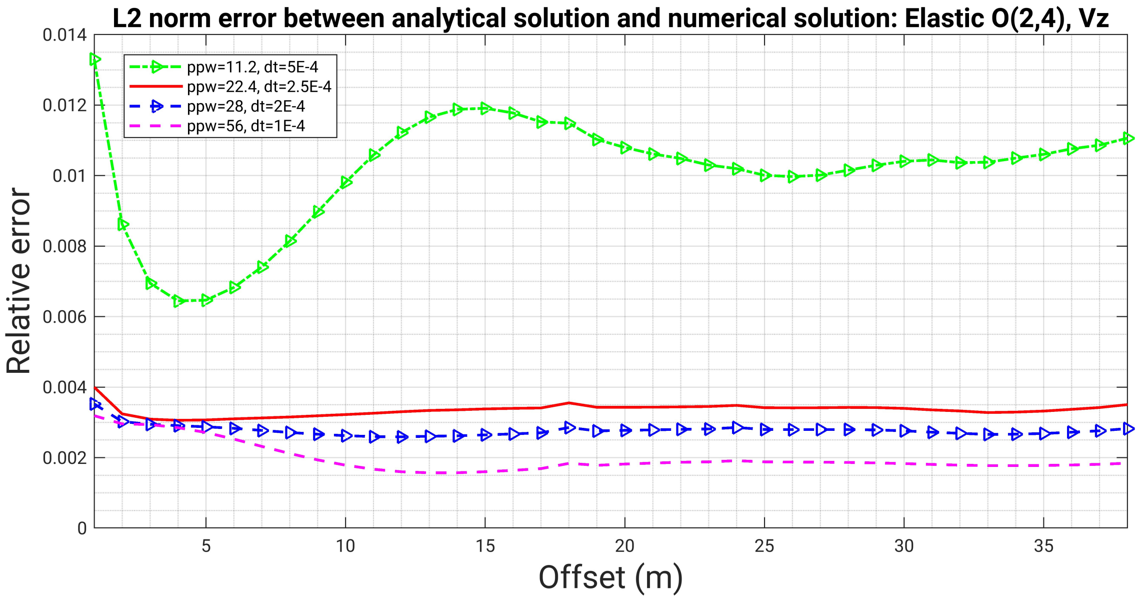

(a) L2 norm error of solid vertical velocity

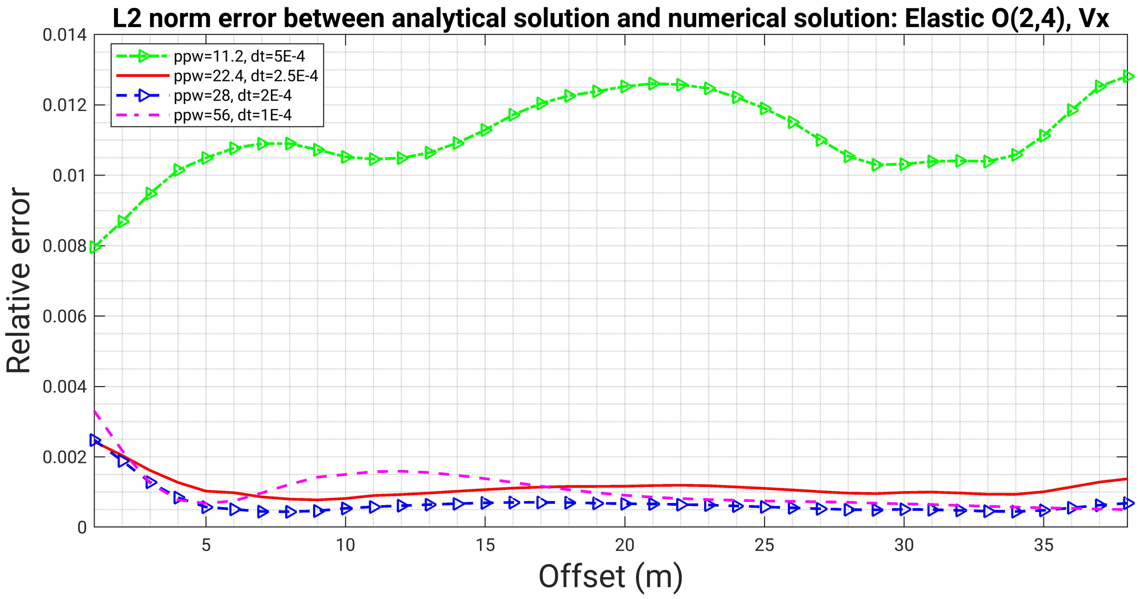

(b) L2 norm error of solid horizontal velocity

Figure 3.8.: L2 norm error varied with offset and ppw number for comparisons of elastic results.

For the poroelastic benchmark test, the model parameters are shown in Table.3.2. The acquisition geometry is a $1000m \times 1000m$ square poroelastic subsurface and triggered by a Ricker source wavelet at the free surface with a central frequency of 30 Hz. The source is implemented as a vertical point source in the solid phase.

The numerical results obtained by *SPECFEM2D* are compared with the results of *IforPoro* and shown in Figs. 3.9-3.11.

	Parameter	**Symbol**	**Unit**	**Value**
Grain	Bulk modulus	K_s	Pa	1.22×10^{10}
	Density	ρ_s	kg/m³	2650
Matrix	Bulk modulus	K_d	Pa	9.6×10^9
	Shear modulus	μ	Pa	5.1×10^9
	Porosity	ϕ	/	0.1
	Tortuosity	τ	/	2
Fluid	Bulk modulus	K_f	Pa	1.985×10^9
	Density	ρ_f	kg/m³	880
	Viscosity	η	N·s/m²	-
Velocity	Fast P wave	V_{fp}	m/s	2639
	Slow P wave	V_{sp}	m/s	961
	Shear wave	V_s	m/s	1449

Table 3.2.: Modeling parameters used for poroelastic benchmarking in section 3.4.1 (Morency and Tromp 2008).

Fig. 3.9 shows the poroelastic wavefields when Rayleigh waves are involved. Three main seismic wave types in the poroelastic subsurface, fast P wave, S wave, and slow P wave, are clearly displayed in the numerical results. Besides, Rayleigh waves are generated in the P-SV profile when a free surface boundary exists on the top. Take the solid vertical velocity profile as an example, numerical solutions calculated from *SPECFEM2D* and *IforPoro* are agreed well with each other from the waveform comparison in Fig. 3.10. Same as Fig. 3.8, the intuitive error comparison from Fig. 3.10 is further displayed in Fig. 3.11. The tiny errors prove that *IforPoro* is also a reliable poroelastic forward solver considering surface waves in the P-SV scheme.

Besides Fig. 3.9, Fig. 3.12 also show the snapshots of the other three velocity components both in solid and fluid phases. There are three types of non-geometric waves observed as leaky waves. One velocity is between the fast P wave and S wave, which is similar to elastic wavefields, and one velocity is between the slow P wave and the fast P wave. Another one is between the slow P wave and S wave/Rayleigh waves. The comparison of Fig.3.7 and Fig. 3.12 illustrates that poroelastic wavefields containing surface waves are much more complicated than elastic wavefields, which can also bring more rock physical information from the subsurface.

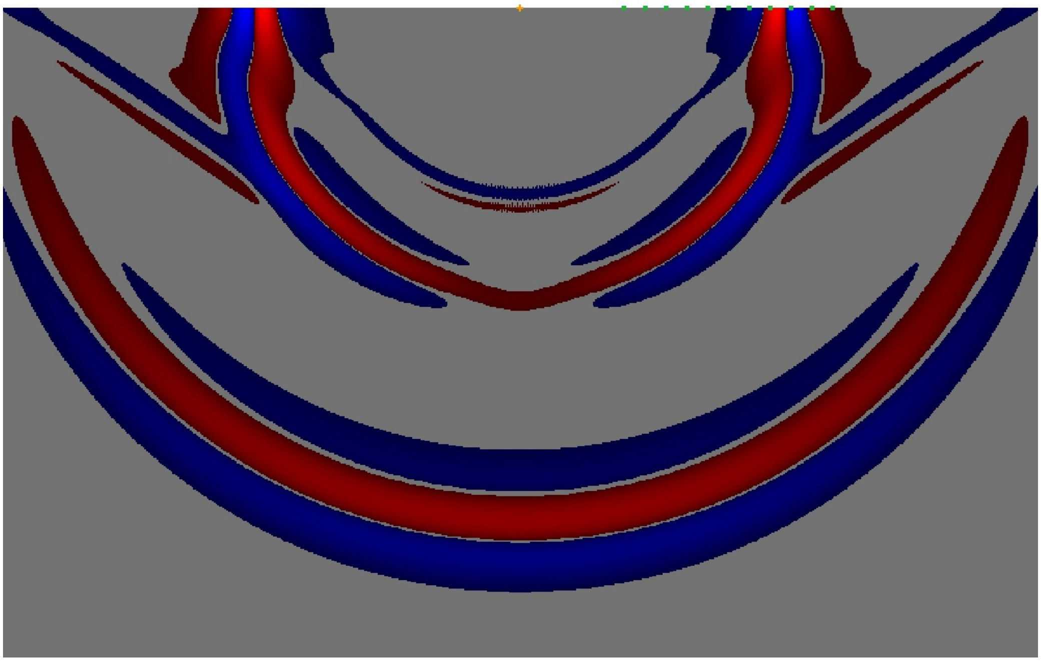

(a) Solid vertical velocity obtained from *SPECFEM2D* with spectral element method (SE)

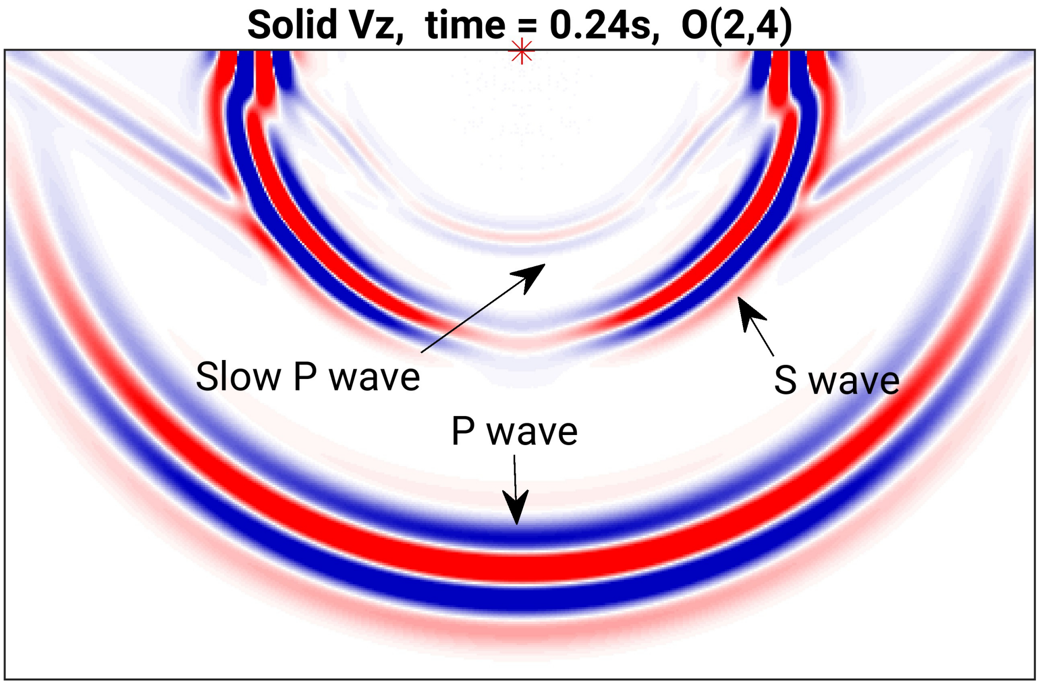

(b) Solid vertical velocity obtained from *IforPoro* with finite difference method (FD)

Figure 3.9.: Poroelastic wavefields including surface waves at time = 0.24 s. The source locates at the free surface in the middle, and the horizontal distance is 1000 m.

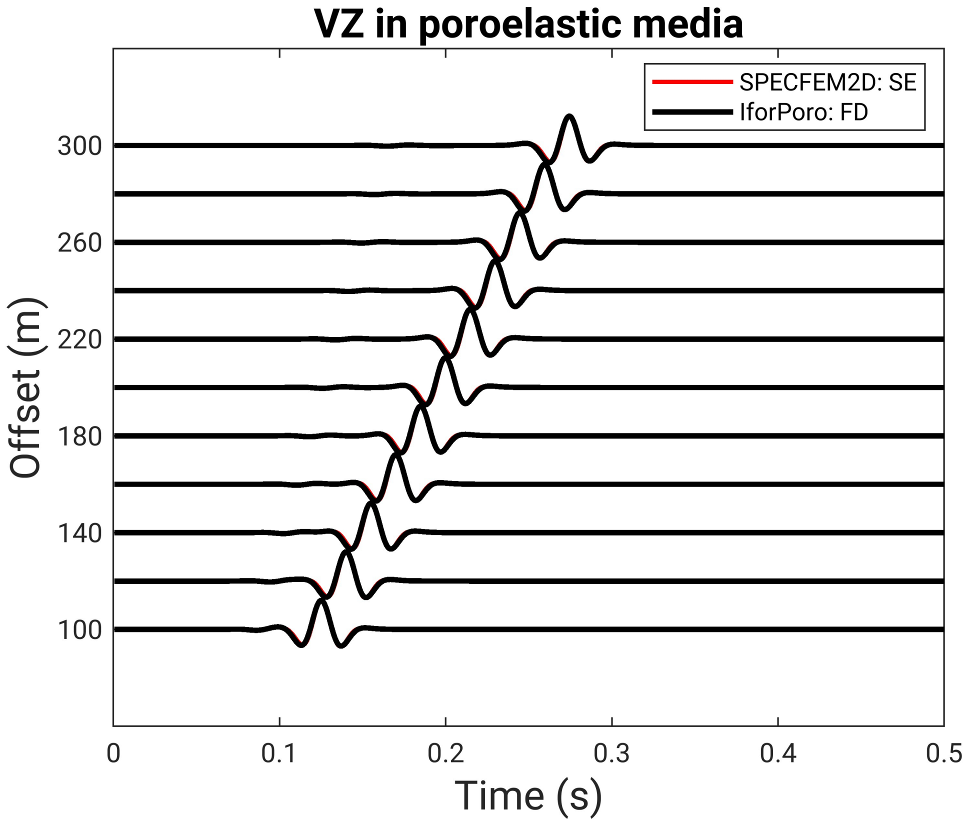

Figure 3.10.: Waveform comparison of the synthetic data obtained from *SPECFEM2D* and *IforPoro*: solid vertical velocity VZ displayed in 11 traces.

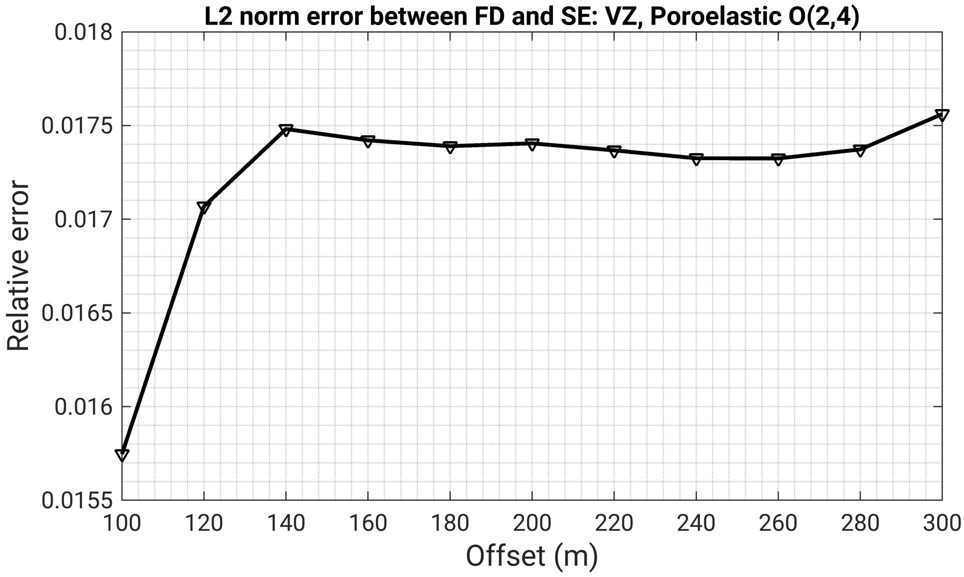

Figure 3.11.: L2 norm error between the numerical results of SE and FD methods.

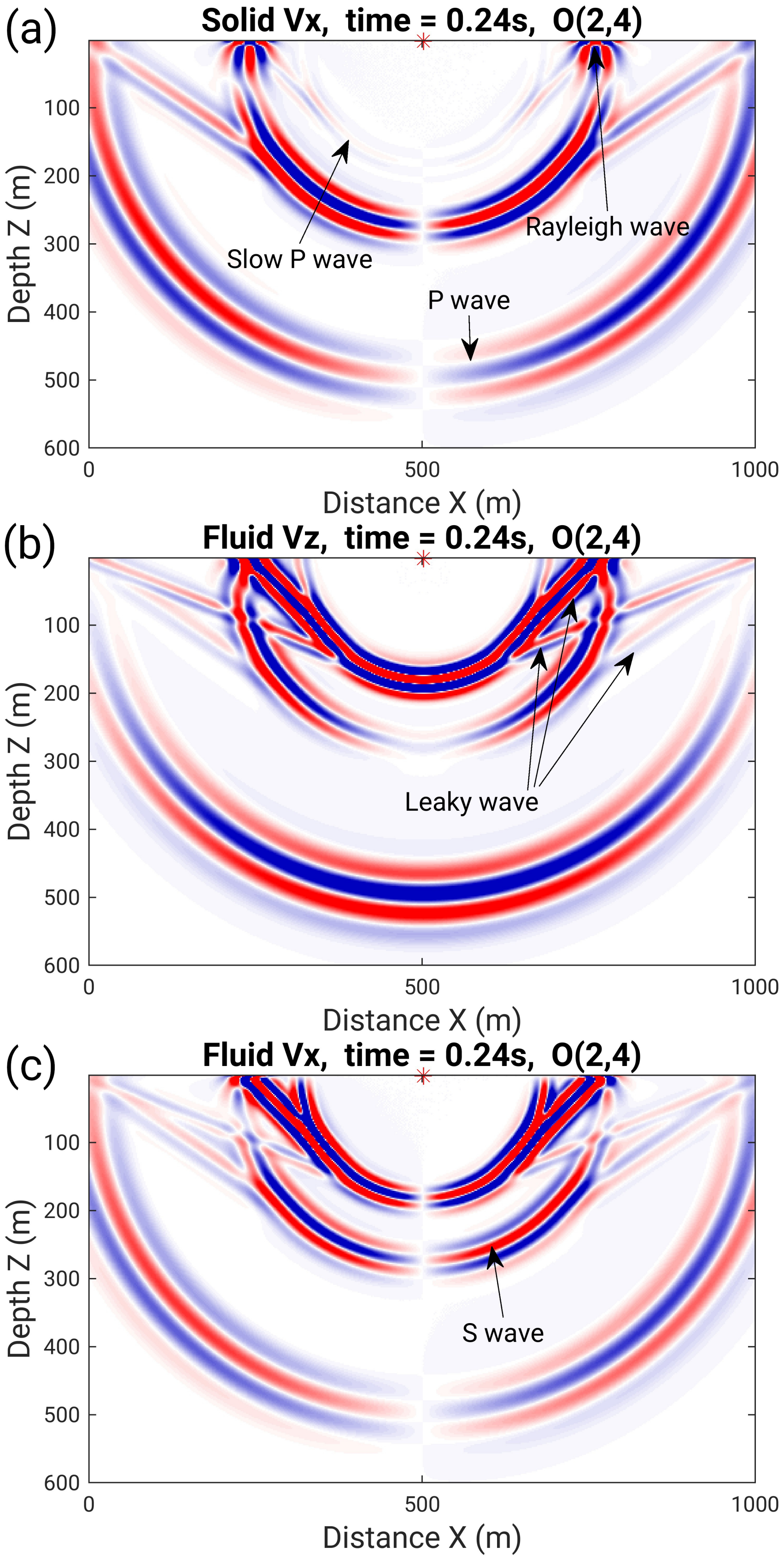

Figure 3.12.: Snapshots of the poroelastic wavefields from *IforPoro*: (a) Horizontal velocity in solid phase; (b) Vertical velocity in fluid phase; (c) Horizontal velocity in fluid phase.

3.4.2. Benchmark tests for the 2D SH forward solver

Love wave is a kind of horizontally polarized surface wave, which is trapped at the free surface boundary in the heterogeneous medium (e.g., layered subsurface). In the case of 2D, Love wave can be simulated based on the SH-wave equations. The 2D poroelastic SH-wave equations and their differential formats are explained in section 3.3.1.2. According to the stress-strain relation, the force from fluid pressure is excluded in SH-wave equations in the 2D X-Z plane so that the elastodynamics systems in the poroelastic and elastic medium are similar under this circumstance.

Layer	**Vs** (m/s)	**Density** (kg/m^3)	**Depth** (m)
1	400	2000	4.5
2	570	2000	-

Table 3.3.: Modeling parameters used for SH forward solver benchmarking in section 3.4.2. The source signal is Ricker wavelet with the central frequency of 30 Hz.

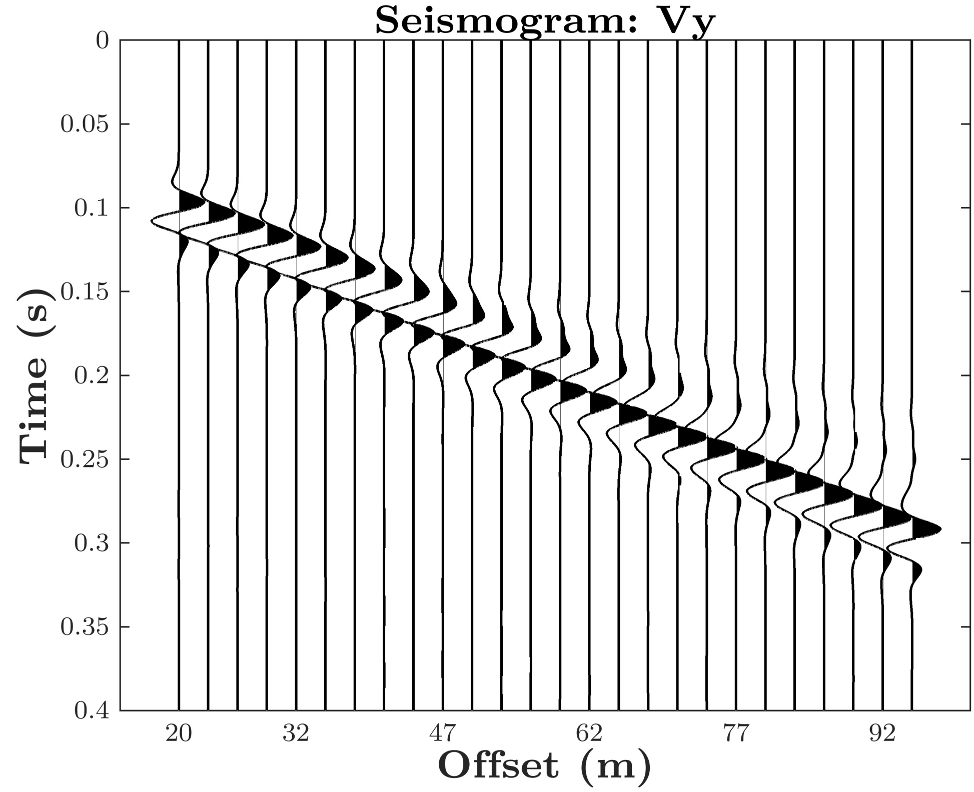

Figure 3.13.: Synthetic data obtained from $IforPoro$: Solid velocity in Y direction. The sampling rate is 0.2 ms, and the duration time is 0.4 s.

In the benchmark tests for the 2D SH forward solver by $IforPoro$, I conduct several numerical simulations on a $100 \times 150m^2$ two-layer elastic model and compare the results of different forward solvers. The elastic model parameters are shown in Table. 3.3. The shear source and 26 receivers are at the free surface. Fig. 3.13 shows the synthetic seismograms simulated by $IforPoro$ after a shear source makes disturbances in the test model. To test the accuracy of these numerical results, I make some waveform comparisons between different modeling packages and calculate their L2 norm errors as in section 3.4.1. In Fig. 3.14, subfigure (a) displays the L2 norm errors between the numerical results of $IforPoro$ and $SOFI2D - Sh$ (Geophysical Institute 2015), while subfigure (b) shows the errors between $IforPoro$ and a Matlab test code with stress image method. Similarly, the relative errors become increasing with larger offsets. Both the L2 norm errors are below 1‰, which indicates Love wave can also be generated accurately by $IforPoro$.

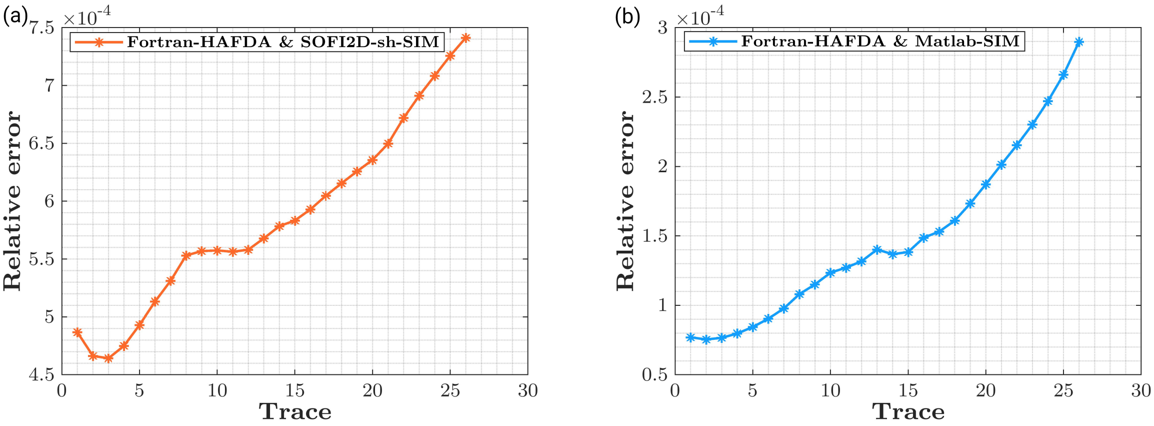

Figure 3.14.: L2 norm error between the numerical results of $IforPoro$ (Fortran 90), $SOFI2D - Sh$ (C language) and Matlab scripts. HAFDA is a method introduced in section 3.3.2.2 for free surface implementation, and SIM means stress image method.

4

The structural inverse problem

The accurate estimation of the Earth's subsurface properties is a challenging task for seismic exploration. Since seismic waves carry the underground structural heterogeneities information, Full-waveform inversion (FWI) has become a multi-parameter reconstruction technique that can exploit the entire information contents of seismograms (J. Virieux and Operto 2009). In general, the main interest in seismic detection is to extract the information on the physical material properties (e.g., lithology, porosity, and fluid content) from different seismic attributes (e.g., P- and S-wave velocities) based on rock physical relations (Butler 2005). The seismic inverse problem theory is stated that if the seismic data taken from a seismic survey based on a model with priory information are as close as possible to the data from field measurements, this model is expected to be a precise description of the unknown earth model. The model could be improved by an iterative algorithm, which contains a classical prestack migration and a forward modeling step (Pratt 1999; A. Tarantola 1984). To find this "best" model, an appropriate physical assumption needs to be made while minimizing an error functional in data space. A. Tarantola (1984) takes an acoustic assumption and linearizes the inverse problem with the perturbation method. If the minimization is regarded as a non-linear problem, the adjoint-state method can be applied to compute the gradient of an error functional with respect to the model parameters in order to avoid massive computing on the high order Fréchet derivatives (Chavent 1974; Plessix 2006).

The error functional representing data residuals is in a classic L2-norm format in Eq. 4.1.

$$\mathcal{J}(\mathbf{m}) = \frac{1}{2}\|\mathbf{u}(\mathbf{m}) - \mathbf{d}_{obs}\|^2 = \frac{1}{2}\sum_{sources}\int_0^T dt \sum_{r=1}^{N}\|\mathbf{u}(\mathbf{x}_\mathbf{r}, t) - \mathbf{d}_{obs}(\mathbf{x}_\mathbf{r}, t)\|^2 \tag{4.1}$$

T is the recording time and N indicates the number of receivers at the receiver position $\mathbf{r}$, $\mathbf{u}$ is the predicted data and $\mathbf{d}_{obs}$ is the recorded data. Since the observed data for fluid components can not be obtained separately, the fluid adjoint sources are not estimated in Eq. 4.1. In this chapter, the physical system of the subsurface is treated as a porous system, which is approximated with the fluid-saturated poroelastic equations introduced in chapter 3, and connects the model space $\mathcal{M} : \mathbf{m}$

with data space $\mathcal{U} : \mathbf{u}$. Then the minimization of the misfit function $\mathcal{J}(\mathbf{m})$ has become an optimization problem. The goal is to find a model $\mathbf{m}_1 = \mathbf{m}_0 + \delta\mathbf{m}_0$ around initial model $\mathbf{m}_0$, which will minimize $\mathcal{J}(\mathbf{m})$, so the misfit function in quadratic form can be extended into Taylor series in Eq. 4.2 (Köhn 2011).

$$\mathcal{J}(\mathbf{m}_1) \approx \mathcal{J}(\mathbf{m}_0) + \delta\mathbf{m}_0 \frac{\partial \mathcal{J}(\mathbf{m}_0)}{\partial m_0} + \frac{1}{2}\delta\mathbf{m}_0 \frac{\partial^2 \mathcal{J}(\mathbf{m}_0)}{\partial {m_0}^2} \delta\mathbf{m}_0^T, \tag{4.2}$$

and the partial derivative of Eq. 4.2 with respect to $\delta\mathbf{m}_0$ is zero, which leads to

$$\frac{\partial^2 \mathcal{J}(\mathbf{m}_0)}{\partial {m_0}^2} \delta\mathbf{m}_0 = -\frac{\partial \mathcal{J}(\mathbf{m}_0)}{\partial m_0}, \tag{4.3}$$

where $\frac{\partial^2 \mathcal{J}(\mathbf{m}_0)}{\partial {m_0}^2}$ represents Hessian matrix $\mathbf{H}_0$ and $G_{\mathbf{m}_0} = \frac{\partial \mathcal{J}(\mathbf{m}_0)}{\partial m_0}$ is the gradient of model parameter $\mathbf{m}_0$. According to the local optimization methods, model space $\mathbf{m}$ can be updated iteratively as shown in Eq. 4.4, where $\mathbf{m}_k$ represents the model parameter at iteration k, and $\delta\mathbf{m}_k$ is its corresponding model corrections (Kurzmann 2012).

$$\mathbf{m}_{k+1} = \mathbf{m}_k + \gamma_k \delta\mathbf{m}_k = \mathbf{m}_k - \gamma_k \mathbf{H}_k^{-1} G_{\mathbf{m}_k}, \tag{4.4}$$

where γ_k is the step length at iteration k. The inverse Hessian matrix can be solved by multiple optimization methods (Nocedal and Wright 2006). For example, $\mathbf{H}^{-1}$ is going to be set as a constant value such as 1 in the gradient methods. The step length γ can be determined by linear search and parabolic fitting methods, etc (Gauthier, Jean Virieux, and Albert Tarantola 1986; Pica, Diet, and A. Tarantola 1990). As the key parts, the derivations of the adjoint poroelastic wave equations and gradients of the objective functions are the main issues that need to be solved, which will be explained in sections 4.1 and 4.2.

4.1. Computing the gradients with augmented functional

Since the objective functional $\mathcal{J}(\mathbf{m})$ depends on $\mathbf{u}(\mathbf{m})$, it can be represented with the functional h in Eq. 4.5 (Plessix 2006).

$$\mathcal{J}(\mathbf{m}) = h(\mathbf{u}(\mathbf{m}), \mathbf{m}), \tag{4.5}$$

here h is a functional from space $\mathcal{U} \times \mathcal{M}$ to real space $\mathcal{R}$. For a poroelastic forward system, f maps an element of model space $\mathcal{M}$ to the element of data space $\mathcal{U}$. For a state variable $\mathbf{u}$, the state equations will satisfy

$$f(\mathbf{u}(\mathbf{m}), \mathbf{m}) = 0 \tag{4.6}$$

to achieve a physical realization. Then an augmented functional $\mathcal{L}$ from space $\mathcal{U} \times \mathcal{U}^* \times \mathcal{M}$ to $\mathcal{R}$ can be defined as

$$\mathcal{L}(\widetilde{\mathbf{u}}, \widetilde{\mathbf{\Lambda}}^*, \mathbf{m}) = h(\widetilde{\mathbf{u}}, \mathbf{m}) - \langle \widetilde{\mathbf{\Lambda}}^*, f(\widetilde{\mathbf{u}}, \mathbf{m}) \rangle_{\mathcal{U}}, \quad (\widetilde{\mathbf{u}} \in \mathcal{U}, \widetilde{\mathbf{\Lambda}}^* \in \mathcal{U}^*) \tag{4.7}$$

where $\widetilde{\mathbf{u}}$ is any element of $\mathcal{U}$. $\widetilde{\mathbf{\Lambda}}^*$ is any element of $\mathcal{U}^*$ and independent from $\mathbf{m}$. $\mathcal{U}^*$ is a dual space of $\mathcal{U}$. For two functions A and B over the spatial domain Ω (P. Yang et al. 2016),

$$\langle A, B \rangle_{\Omega} = \int_{\Omega} A(\mathbf{x}) B(\mathbf{x}) d\mathbf{x}. \tag{4.8}$$

For a state variable $\mathbf{u}$ described in Eq. 4.6, Eq. 4.7 can be rewritten below.

$$\mathcal{L}(\mathbf{u}, \widetilde{\mathbf{\Lambda}}^*, \mathbf{m}) = h(\mathbf{u}, \mathbf{m}) = \mathcal{J}(\mathbf{m}) \tag{4.9}$$

and

$$\frac{\partial \mathcal{L}(\mathbf{u}, \widetilde{\mathbf{\Lambda}}^*, \mathbf{m})}{\partial \mathbf{m}} = \frac{\mathcal{J}(\mathbf{m})}{\partial \mathbf{m}} \tag{4.10}$$

In this way, the original objective functional $\mathcal{J}(\mathbf{m})$ is extended with a model independent dual space $\mathcal{U}^*$ and replaced by $\mathcal{L}(\mathbf{u}, \widetilde{\mathbf{\Lambda}}^*, \mathbf{m})$. For any element $\widetilde{\mathbf{u}}$, Eq. 4.7 is rewritten by

$$\mathcal{L}(\widetilde{\mathbf{u}}, \widetilde{\mathbf{\Lambda}}^*, \mathbf{m}) = \frac{1}{2} \| \widetilde{\mathbf{u}}(\mathbf{m}) - \mathbf{d}_{obs} \|^2 - \langle \widetilde{\mathbf{\Lambda}}^*, f(\widetilde{\mathbf{u}}, \mathbf{m}) \rangle_{\mathcal{U}}. \tag{4.11}$$

For a sate variable $\mathbf{u}$,

$$\mathcal{L}(\mathbf{u}, \mathbf{\Lambda}^*, \mathbf{m}) = \mathcal{J}(\mathbf{m}) = \frac{1}{2} \| \mathbf{u}(\mathbf{m}) - \mathbf{d}_{obs} \|^2 - \langle \mathbf{\Lambda}^*, f(\mathbf{u}, \mathbf{m}) \rangle_{\mathcal{U}}, \quad \mathbf{\Lambda}^* \in \mathcal{U}^*. \tag{4.12}$$

4.1.1. Gradients derivation in poroelastic PSV/Rayleigh wave equations

Based on Eq. 4.6, here f maps the 2D fluid-saturated isotropic poroelastic Rayleigh/PSV-wave equations, and their displacement-stress format is explained in Eq. 4.15. The model parameters have been described in detail in chapter 3. Similar to variable $\mathbf{u}$, the dual variables

$$\mathbf{\Lambda}^* = (\Lambda^*_{sx}, \Lambda^*_{fx}, \Lambda^*_{sz}, \Lambda^*_{fz}, \Lambda^*_{xx}, \Lambda^*_{zz}, \Lambda^*_{xz}, \Lambda^*_{P}). \tag{4.13}$$

Then Eq. 4.12 becomes

$$\begin{aligned} \mathcal{L}(\mathbf{u}, \mathbf{\Lambda}^*, \mathbf{m}) = \frac{1}{2} \int_{x,z \in \Omega} \int_t [(u_x - u_{x,obs})^2 + (u_z - u_{z,obs})^2] d\Omega dt - \\ \int_{x,z \in \Omega} \int_t (\Lambda^*_{sx} F_{sx} + \Lambda^*_{fx} F_{fx} + \Lambda^*_{sz} F_{sz} + \Lambda^*_{fz} F_{fz} \\ + \Lambda^*_{xx} F_{xx} + \Lambda^*_{zz} F_{zz} + \Lambda^*_{xz} F_{xz} + \Lambda^*_{P} F_{P}) d\Omega dt \end{aligned} \tag{4.14}$$

$$
\begin{aligned}
F_{sx} &= \frac{\partial^2 u_x}{\partial t^2} - A\phi m(\frac{\partial \sigma_{xx}}{\partial x} + \frac{\partial \sigma_{xz}}{\partial z}) - A\rho_2 \frac{\partial P}{\partial x} \\
F_{fx} &= \frac{\partial^2 u_x^f}{\partial t^2} + A(\rho_f - \phi m)(\frac{\partial \sigma_{xx}}{\partial x} + \frac{\partial \sigma_{xz}}{\partial z}) + A\rho_1 \frac{\partial P}{\partial x} \\
F_{sz} &= \frac{\partial^2 u_z}{\partial t^2} - A\phi m(\frac{\partial \sigma_{xz}}{\partial x} + \frac{\partial \sigma_{zz}}{\partial z}) - A\rho_2 \frac{\partial P}{\partial z} \\
F_{fz} &= \frac{\partial^2 u_z^f}{\partial t^2} + A(\rho_f - \phi m)(\frac{\partial \sigma_{xz}}{\partial x} + \frac{\partial \sigma_{zz}}{\partial z}) + A\rho_1 \frac{\partial P}{\partial z} \\
F_{xx} &= \sigma_{xx} - (\lambda + 2\mu)\frac{\partial u_x}{\partial x} - \lambda \frac{\partial u_z}{\partial z} + \alpha P \\
F_{zz} &= \sigma_{zz} - \lambda \frac{\partial u_x}{\partial x} - (\lambda + 2\mu)\frac{\partial u_z}{\partial z} + \alpha P \\
F_{xz} &= \sigma_{xz} - \mu(\frac{\partial u_z}{\partial x} + \frac{\partial u_x}{\partial z}) \\
F_P &= P + \phi M(\frac{\partial u_x^f}{\partial x} + \frac{\partial u_z^f}{\partial z}) + (\alpha - \phi)M(\frac{\partial u_x}{\partial x} + \frac{\partial u_z}{\partial z})
\end{aligned}
\tag{4.15}
$$

when the unknown data variables in the misfit function are the velocity differences. From the integration by parts, in the physical spatial domain Ω within the time duration $[0, T]$, we have

$$
\begin{aligned}
\langle \mathbf{\Lambda}^*, \partial_t \mathbf{u} \rangle_T &= -\langle \partial_t \mathbf{\Lambda}^*, \mathbf{u} \rangle_T \\
\langle \mathbf{\Lambda}^*, \partial_x \mathbf{u} \rangle_\Omega &= -\langle \partial_x \mathbf{\Lambda}^*, \mathbf{u} \rangle_\Omega \\
\langle \mathbf{\Lambda}^*, \partial_z \mathbf{u} \rangle_\Omega &= -\langle \partial_z \mathbf{\Lambda}^*, \mathbf{u} \rangle_\Omega
\end{aligned}
\tag{4.16}
$$

and further second order

$$
\langle \mathbf{\Lambda}^*, \partial_{tt} \mathbf{u} \rangle_T = \langle \partial_{tt} \mathbf{\Lambda}^*, \mathbf{u} \rangle_T \tag{4.17}
$$

when the zero-valued boundary condition and initial condition $\mathbf{\Lambda}^*|_{t=T} = \mathbf{u}|_{t=0} = 0$ are satisfied. Based on Eq. 4.14, the derivative of augmented objective functional $\mathcal{L}$ respect to data $\mathbf{u}$ has become

$$\begin{aligned}
\frac{\partial \mathcal{L}}{\partial u_x}\delta u_x = \frac{\partial \mathcal{J}(\mathbf{m})}{\partial u_x}du_x - \int_{x,z\in\Omega}\int_t [\Lambda^*_{sx}\frac{\partial^2 u_x}{\partial t^2} - \Lambda^*_{xx}(\lambda+2\mu)\frac{\partial u_x}{\partial x} - \Lambda^*_{zz}\lambda\frac{\partial u_x}{\partial x}& \\
-\Lambda^*_{xz}\mu\frac{\partial u_x}{\partial z} + \Lambda^*_{P}(\alpha-\phi)M\frac{\partial u_x}{\partial x}],& \\
\frac{\partial \mathcal{L}}{\partial u^f_x}\delta u^f_x = \frac{\partial \mathcal{J}(\mathbf{m})}{\partial u^f_x}du^f_x - \int_{x,z\in\Omega}\int_t [\Lambda^*_{fx}\frac{\partial^2 u^f_x}{\partial t^2} + \Lambda^*_{P}\phi M\frac{\partial u^f_x}{\partial x}],& \\
\frac{\partial \mathcal{L}}{\partial u_z}\delta u_z = \frac{\partial \mathcal{J}(\mathbf{m})}{\partial u_z}du_z - \int_{x,z\in\Omega}\int_t [\Lambda^*_{sz}\frac{\partial^2 u_z}{\partial t^2} - \Lambda^*_{xx}\lambda\frac{\partial u_z}{\partial z} - \Lambda^*_{zz}(\lambda+2\mu)\frac{\partial u_z}{\partial z}& \\
-\Lambda^*_{xz}\mu\frac{\partial u_z}{\partial x} + \Lambda^*_{P}(\alpha-\phi)M\frac{\partial u_z}{\partial z}],& \\
\frac{\partial \mathcal{L}}{\partial u^f_z}\delta u^f_z = \frac{\partial \mathcal{J}(\mathbf{m})}{\partial u^f_z}du^f_z - \int_{x,z\in\Omega}\int_t [\Lambda^*_{fz}\frac{\partial^2 u^f_z}{\partial t^2} + \Lambda^*_{P}\phi M\frac{\partial u^f_z}{\partial z}],& \\
\frac{\partial \mathcal{L}}{\partial \sigma_{xx}}\delta \sigma_{xx} = -\int_{x,z\in\Omega}\int_t [-\Lambda^*_{sx}A\phi m\frac{\partial \sigma_{xx}}{\partial x} + \Lambda^*_{fx}A(\rho_f-\phi m)\frac{\partial \sigma_{xx}}{\partial x} + \Lambda^*_{xx}\sigma_{xx}],& \\
\frac{\partial \mathcal{L}}{\partial \sigma_{zz}}\delta \sigma_{zz} = -\int_{x,z\in\Omega}\int_t [-\Lambda^*_{sz}A\phi m\frac{\partial \sigma_{zz}}{\partial z} + \Lambda^*_{fz}A(\rho_f-\phi m)\frac{\partial \sigma_{zz}}{\partial z} + \Lambda^*_{zz}\sigma_{zz}],& \\
\frac{\partial \mathcal{L}}{\partial \sigma_{xz}}\delta \sigma_{xz} = -\int_{x,z\in\Omega}\int_t [-\Lambda^*_{sx}A\phi m\frac{\partial \sigma_{xz}}{\partial z} + \Lambda^*_{fx}A(\rho_f-\phi m)\frac{\partial \sigma_{xz}}{\partial z}& \\
-\Lambda^*_{sz}A\phi m\frac{\partial \sigma_{xz}}{\partial x} + \Lambda^*_{fz}A(\rho_f-\phi m)\frac{\partial \sigma_{xz}}{\partial x} + \Lambda^*_{xz}\sigma_{xz}],& \\
\frac{\partial \mathcal{L}}{\partial P}\delta P = -\int_{x,z\in\Omega}\int_t [-\Lambda^*_{sx}A\rho_2\frac{\partial P}{\partial x} + \Lambda^*_{fx}A\rho_1\frac{\partial P}{\partial x} - \Lambda^*_{sz}A\rho_2\frac{\partial P}{\partial z} + \Lambda^*_{fz}A\rho_1\frac{\partial P}{\partial z}& \\
+\Lambda^*_{xx}\alpha P + \Lambda^*_{xx}\alpha P + \Lambda^*_{P}P].&
\end{aligned} \tag{4.18}$$

When $(\mathbf{u}, \mathbf{\Lambda}^*, \mathbf{m})$ is the saddle point of $\mathcal{L}(\mathbf{u}, \mathbf{\Lambda}^*, \mathbf{m})$,

$$\frac{\partial \mathcal{L}}{\partial \mathbf{u}} = 0, \quad \frac{\partial \mathcal{L}}{\partial \mathbf{m}} = 0. \tag{4.19}$$

Eq. 4.18 can be summarized in Eq. 4.20, which represents the adjoint system corresponding to forward wavefields $\mathbf{u}$.

$$\begin{aligned}
\frac{\partial^2 \Lambda^*_{sx}}{\partial t^2} &= -(\lambda + 2\mu)\frac{\partial \Lambda^*_{xx}}{\partial x} - \lambda\frac{\partial \Lambda^*_{zz}}{\partial x} - \mu\frac{\partial \Lambda^*_{xz}}{\partial z} + (\alpha - \phi)M\frac{\partial \Lambda^*_P}{\partial x} + (u_x - u_{x,obs}) \\
\frac{\partial^2 \Lambda^*_{fx}}{\partial t^2} &= \phi M\frac{\partial \Lambda^*_P}{\partial x} \\
\frac{\partial^2 \Lambda^*_{sz}}{\partial t^2} &= -\lambda\frac{\partial \Lambda^*_{xx}}{\partial z} - (\lambda + 2\mu)\frac{\partial \Lambda^*_{zz}}{\partial z} - \mu\frac{\partial \Lambda^*_{xz}}{\partial x} + (\alpha - \phi)M\frac{\partial \Lambda^*_P}{\partial z} + (u_z - u_{z,obs}) \\
\frac{\partial^2 \Lambda^*_{fz}}{\partial t^2} &= \phi M\frac{\partial \Lambda^*_P}{\partial z} \\
\Lambda^*_{xx} &= -A\phi m\frac{\partial \Lambda^*_{sx}}{\partial x} + A(\rho_f - \phi m)\frac{\partial \Lambda^*_{fx}}{\partial x} \\
\Lambda^*_{zz} &= -A\phi m\frac{\partial \Lambda^*_{sz}}{\partial z} + A(\rho_f - \phi m)\frac{\partial \Lambda^*_{fz}}{\partial z} \\
\Lambda^*_{xz} &= -A\phi m(\frac{\partial \Lambda^*_{sx}}{\partial z} + \frac{\partial \Lambda^*_{sz}}{\partial x}) + A(\rho_f - \phi m)(\frac{\partial \Lambda^*_{fx}}{\partial z} + \frac{\partial \Lambda^*_{fz}}{\partial x}) \\
\Lambda^*_P &= -A(\rho_2 - \alpha\phi m)(\frac{\partial \Lambda^*_{sx}}{\partial x} + \frac{\partial \Lambda^*_{sz}}{\partial z}) + A[\rho_1 - \alpha(\rho_f - \phi m)](\frac{\partial \Lambda^*_{fx}}{\partial x} + \frac{\partial \Lambda^*_{fz}}{\partial z})
\end{aligned} \tag{4.20}$$

In poroelastic P-SV equations,

$$\mathbf{m}^{PSV} = \{\lambda, \mu, \rho_s, \rho_f, K_s, K_f, \phi\}. \tag{4.21}$$

Therefore, based on Eqs. 4.14 and 4.19, the gradients of the objective function with respect to the model parameters can be derived as below.

$$\begin{aligned}
\frac{\partial \mathcal{J}}{\partial \lambda} = -\sum_{sources}\int_0^T dt\{A\rho_f[\tau(\frac{\partial \Lambda^*_{sx}}{\partial x} + \frac{\partial \Lambda^*_{sz}}{\partial z}) + (\tau - 1)(\frac{\partial \Lambda^*_{fx}}{\partial x} + \frac{\partial \Lambda^*_{fz}}{\partial z})] \\
+\frac{M}{K_s}\Lambda^*_P\}(\frac{\partial u_x}{\partial x} + \frac{\partial u_z}{\partial z} + \frac{1}{K_s}P),
\end{aligned} \tag{4.22}$$

$$\begin{aligned}
\frac{\partial \mathcal{J}}{\partial \mu} = -\sum_{sources}\int_0^T dt\{A\rho_f[\tau[2(\frac{\partial \Lambda^*_{sx}}{\partial x}\frac{\partial u_x}{\partial x} + \frac{\partial \Lambda^*_{sz}}{\partial z}\frac{\partial u_z}{\partial z}) + (\frac{\partial \Lambda^*_{sz}}{\partial x} + \frac{\partial \Lambda^*_{sx}}{\partial z}) \\
(\frac{\partial u_z}{\partial x} + \frac{\partial u_x}{\partial z})] + (\tau - 1)[2(\frac{\partial \Lambda^*_{fx}}{\partial x}\frac{\partial u_x}{\partial x} + \frac{\partial \Lambda^*_{fz}}{\partial z}\frac{\partial u_z}{\partial z}) + (\frac{\partial \Lambda^*_{fz}}{\partial x} + \frac{\partial \Lambda^*_{fx}}{\partial z}) \\
(\frac{\partial u_z}{\partial x} + \frac{\partial u_x}{\partial z})]] + \frac{2}{3K_s}[\frac{1}{\alpha}P[A(\rho_2(\frac{\partial \Lambda^*_{sx}}{\partial x} + \frac{\partial \Lambda^*_{sz}}{\partial z}) - \rho_1(\frac{\partial \Lambda^*_{fx}}{\partial x} + \frac{\partial \Lambda^*_{fz}}{\partial z})) - \Lambda^*_P] \\
+M\Lambda^*_P(\frac{\partial u_x}{\partial x} + \frac{\partial u_z}{\partial z} + \frac{1}{K_s}P)]\},
\end{aligned} \tag{4.23}$$

$$\begin{aligned}\frac{\partial \mathcal{J}}{\partial \rho_s} = -\sum_{sources}\int_0^T & dt A\rho_f(1-\phi)\{\frac{\partial v_x}{\partial t}[\tau\Lambda^*_{sx}+(\tau-1)\Lambda^*_{fx}] \\ & +\frac{\partial v_z}{\partial t}[\tau\Lambda^*_{sz}+(\tau-1)\Lambda^*_{fz}]\},\end{aligned} \tag{4.24}$$

$$\begin{aligned}\frac{\partial \mathcal{J}}{\partial \rho_f} = -\sum_{sources}\int_0^T & dt\{A(\tau-1)[\frac{\partial v_x}{\partial t}(\rho_2\Lambda^*_{sx}-\rho_1\Lambda^*_{fx}) \\ +\frac{\partial v_z}{\partial t}(\rho_2\Lambda^*_{sz}-\rho_1\Lambda^*_{fz})] & +\frac{1}{\rho_f}(\frac{\partial v^f_x}{\partial t}\Lambda^*_{fx}+\frac{\partial v^f_z}{\partial t}\Lambda^*_{fz})\},\end{aligned} \tag{4.25}$$

$$\begin{aligned}\frac{\partial \mathcal{J}}{\partial K_s} = \sum_{sources}\int_0^T dt\frac{1-\alpha}{K_s}\{A\rho_f P[\tau(\frac{\partial \Lambda^*_{sx}}{\partial x}+\frac{\partial \Lambda^*_{sz}}{\partial z}) \\ +(\tau-1)(\frac{\partial \Lambda^*_{fx}}{\partial x}+\frac{\partial \Lambda^*_{fz}}{\partial z})]+M\Lambda^*_P[\frac{\partial u_x}{\partial x}+\frac{\partial u_z}{\partial z}+\frac{1-2\alpha+\phi}{K_s(1-\alpha)}P]\},\end{aligned} \tag{4.26}$$

$$\frac{\partial \mathcal{J}}{\partial K_f} = -\sum_{sources}\int_0^T dt\frac{\phi M}{K_f^2}P\Lambda^*_P, \tag{4.27}$$

$$\begin{aligned}\frac{\partial \mathcal{J}}{\partial \phi} = \sum_{sources}\int_0^T dt\{-A\rho_f[(\rho_f\frac{\partial v^f_x}{\partial t}-\rho_s\frac{\partial v_x}{\partial t})(\tau\Lambda^*_{sx}+(\tau-1)\Lambda^*_{fx}) \\ +(\rho_f\frac{\partial v^f_z}{\partial t}-\rho_s\frac{\partial v_z}{\partial t})(\tau\Lambda^*_{sz}+(\tau-1)\Lambda^*_{fz})]-\frac{\alpha M}{\phi}\Lambda^*_P(\frac{\partial u_x}{\partial x}+\frac{\partial u_z}{\partial z}+\frac{1}{K_s}P)\}.\end{aligned} \tag{4.28}$$

4.1.2. Gradients derivation in poroelastic SH/Love wave equations

In the 2D case at $X-Z$ plane, based on Fig. 3.3, only the shear stresses related to horizontal direction Y take part in the constitutive equation, and the fluid pressure is excluded as well. Similar to section 4.1.1, the state equations in displacement-stress format are as follows.

$$\begin{aligned}F_{sy} &= \frac{\partial^2 u_y}{\partial t^2}-A\phi m(\frac{\partial \sigma_{xy}}{\partial x}+\frac{\partial \sigma_{yz}}{\partial z}) \\ F_{xy} &= \sigma_{xy}-\mu\frac{\partial u_y}{\partial x} \\ F_{yz} &= \sigma_{yz}-\mu\frac{\partial u_y}{\partial z}\end{aligned} \tag{4.29}$$

The dual variables in poroelastic SH/Love equations

$$\mathbf{\Lambda}^* = (\Lambda^*_{sy},\Lambda^*_{xy},\Lambda^*_{yz}), \tag{4.30}$$

and the model parameters are reduced to

$$\mathbf{m}^{SH} = \{\mu, \rho_s, \rho_f, \phi\}. \tag{4.31}$$

Now the Lagrangian augmented objective functional has become

$$\begin{aligned}\mathcal{L}(\mathbf{u}^{SH}, \mathbf{\Lambda}^*, \mathbf{m}^{SH}) = \frac{1}{2}\int_{x,z\in\Omega}\int_t (u_y - u_{y,obs})^2 d\Omega dt - \\ \int_{x,z\in\Omega}\int_t (\Lambda^*_{sy}F_{sy} + \Lambda^*_{xy}F_{xy} + \Lambda^*_{yz}F_{yz}) d\Omega dt,\end{aligned} \tag{4.32}$$

which will also satisfy the condition in Eq. 4.19 for a state saddle point $(\mathbf{u}^{SH}, \mathbf{\Lambda}^*, \mathbf{m}^{SH})$. The derivatives of $\mathcal{L}$ respect to data variable $\mathbf{u}^{sh}$ are

$$\begin{aligned}\frac{\partial\mathcal{L}}{\partial u_y}\delta u_y = \frac{\partial\mathcal{J}(\mathbf{m}^{SH})}{\partial u_y}du_y - \int_{x,z\in\Omega}\int_t [\Lambda^*_{sy}\frac{\partial^2 u_y}{\partial t^2} - \Lambda^*_{xy}\mu\frac{\partial u_y}{\partial x} - \Lambda^*_{yz}\mu\frac{\partial u_y}{\partial z}], \\ \frac{\partial\mathcal{L}}{\partial\sigma_{xy}}\delta\sigma_{xy} = -\int_{x,z\in\Omega}\int_t [-\Lambda^*_{sy}A\phi m\frac{\partial\sigma_{xy}}{\partial x} + \Lambda^*_{xy}\sigma_{xy}], \\ \frac{\partial\mathcal{L}}{\partial\sigma_{yz}}\delta\sigma_{yz} = -\int_{x,z\in\Omega}\int_t [-\Lambda^*_{sy}A\phi m\frac{\partial\sigma_{yz}}{\partial z} + \Lambda^*_{yz}\sigma_{yz}].\end{aligned} \tag{4.33}$$

The state equations 4.29 are obtained when $\frac{\partial\mathcal{L}}{\partial\Lambda^*} = 0$, similarly, the adjoint equations will be derived in Eq. 4.34 when $\frac{\partial\mathcal{L}}{\partial\mathbf{u}^{sh}} = 0$ is satisfied.

$$\begin{aligned}\frac{\partial^2\Lambda^*_{sy}}{\partial t^2} = -\mu(\frac{\partial\Lambda^*_{xy}}{\partial x} + \frac{\partial\Lambda^*_{yz}}{\partial z}) + (u_y - u_{y,obs}), \\ \Lambda^*_{xy} = -A\phi m\frac{\Lambda^*_{sy}}{\partial x}, \\ \Lambda^*_{yz} = -A\phi m\frac{\Lambda^*_{sy}}{\partial z}.\end{aligned} \tag{4.34}$$

The gradients $\frac{\partial\mathcal{L}}{\mathbf{m}^{SH}}$, which are the derivatives of $\mathcal{L}$ respect to model parameter $\mathbf{m}^{SH}$ are explained below.

$$\frac{\partial\mathcal{J}}{\partial\mu} = -\sum_{sources}\int_0^T dt A\tau\rho_f(\frac{\partial\Lambda^*_{sy}}{\partial x}\frac{\partial u_y}{\partial x} + \frac{\partial\Lambda^*_{sy}}{\partial z}\frac{\partial u_y}{\partial z}), \tag{4.35}$$

$$\frac{\partial\mathcal{J}}{\partial\rho_s} = -\sum_{sources}\int_0^T dt A\tau\rho_f(1-\phi)\Lambda^*_{sy}\frac{\partial v_y}{\partial t}, \tag{4.36}$$

$$\frac{\partial\mathcal{J}}{\partial\rho_f} = -\sum_{sources}\int_0^T dt A(\tau - 1)\rho_2\Lambda^*_{sy}\frac{\partial v_y}{\partial t}, \tag{4.37}$$

$$\frac{\partial \mathcal{J}}{\partial \phi} = -\sum_{sources} \int_0^T dt A \rho_f [(\tau - 1)\rho_f - \tau \rho_s] \Lambda_{sy}^* \frac{\partial v_y}{\partial t}, \tag{4.38}$$

where v_y represents velocity in Y direction, and the model parameters are explained in chapter 3.

4.2. Computing the gradients with perturbation theory

As introduced before, here f maps an element of model space $\mathbf{m}$ to the element of data space $\mathbf{u}$.

$$f(\mathbf{u}, \mathbf{m}) = \mathbf{L}\mathbf{u} - \mathbf{s} = 0, \tag{4.39}$$

where $\mathbf{L}$ is the forward differential operator, and $\mathbf{s}$ is the external force. Following the work of A. Tarantola (1984), the inverse problem is linerlized and a perturbed data $\delta\mathbf{u}$ is defined as the differences between the wavefields corresponding to predicted data and observed data. Then f shows the mapping below. The total fields $\mathbf{u}$ can be decomposed into the primary fields $\mathbf{u_0}$ and scattered fields $\delta\mathbf{u}$ linearly.

$$f : \mathbf{m} = \mathbf{m_0} + \delta\mathbf{m} \longrightarrow \mathbf{u} = \mathbf{u_0} + \delta\mathbf{u} \tag{4.40}$$

Thus, the misfit functional Eq. 4.1 can be reformed in Eq. 4.41,

$$\mathcal{J}(\mathbf{m}) = \frac{1}{2}\|\mathbf{u}(\mathbf{m}) - \mathbf{d}_{obs}\|^2 = \frac{1}{2}\delta\mathbf{u}\delta\mathbf{u}^*, \tag{4.41}$$

where $\delta\mathbf{u}^*$ represents the adjoint wavefield impulsed by the data differences $\mathbf{u}(\mathbf{m}) - \mathbf{d}_{obs}$. Then the derivatives of the misfit functional $\mathcal{J}$ respect to the model parameters $\mathbf{m}$

$$\frac{\partial \mathcal{J}(\mathbf{m})}{\partial \mathbf{m}} = \frac{\partial \delta\mathbf{u}}{\partial \delta\mathbf{m}}(\mathbf{u} - \mathbf{d}_{obs}). \tag{4.42}$$

Based on Eqs. 4.39 and 4.40, the scattered wavefields $\delta\mathbf{u}$ is generated from the perturbed model $\delta\mathbf{m}$ following the mapping f. The response of the perturbation $\delta\mathbf{m}$ can be considered as the excitation of secondary sources (Wu and Aki 1989). Thus, the perturbation problem can also be written in compact notation as

$$\mathbf{L}\delta\mathbf{u} = \delta\mathbf{m}\mathbf{s}', \tag{4.43}$$

where $\delta\mathbf{m}\mathbf{s}'$ represents the external source. Similarly, the adjoint wavefields $\delta\mathbf{u}^*$ can follow the rules below.

$$\mathbf{L}^*\mathbf{\Lambda}^* = \mathbf{u} - \mathbf{d}_{obs}, \tag{4.44}$$

where $\mathbf{L}^*$ is the adjoint operator for the adjoint wave component $\mathbf{\Lambda}^* \in \delta\mathbf{u}$. Combined with Eqs. 4.42 and 4.43,

$$\frac{\partial \mathcal{J}(\mathbf{m})}{\partial \mathbf{m}} = (\mathbf{L}^{-1}\mathbf{s}')^T\mathbf{L}^*\mathbf{\Lambda}^*, \tag{4.45}$$

where $\mathbf{L}^{-1}$ is the inverse matrix of forward operator $\mathbf{L}$. When $\mathbf{L}^{*} = \mathbf{L}^{T}$, which is the transpose matrix of $\mathbf{L}$,

$$\frac{\partial \mathcal{J}(\mathbf{m})}{\partial \mathbf{m}} = (\mathbf{s}')^{T}\mathbf{\Lambda}^{*}, \tag{4.46}$$

$\mathbf{\Lambda}^{*}$ represents the inverse time propagating adjoint wavefields, which can be solved by Eq. 4.44.

4.2.1. Gradients and first-order scattering pulses in poroelastic PSV/Rayleigh wave equations

From the equations of motion and constitutive law for the fluid-saturated porous media in chapter 3, the forward operator for P-SV wave equations

$$\mathbf{L}^{PSV} = \mathbf{A} + \mathbf{B} + \mathbf{C}. \tag{4.47}$$

In the meanwhile, the data space

$$\mathbf{u}^{PSV} = (v_x, v_x^f, v_z, v_z^f, \sigma_{xx}, \sigma_{zz}, \sigma_{xz}, P)^{\mathrm{T}} \tag{4.48}$$

consists of solid phase $\mathbf{u_s}$ and fluid phase $\mathbf{u_f}$ and can decompose into velocity-stress components in Eq. 4.48. Correspondingly, the external pulses will be given by

$$\mathbf{s}^{PSV} = (s_x, s_x^f, s_z, s_z^f, s_{xx}, s_{zz}, s_{xz}, s_p)^{\mathrm{T}}. \tag{4.49}$$

When considering the isotropic medium,

$$\mathbf{A} = \begin{bmatrix} \mathbf{0}_4 & \mathbf{D}^1 \\ \mathbf{D}^2 & \mathbf{0}_4 \end{bmatrix} \partial_x, \tag{4.50}$$

$$\mathbf{D}^1 = \begin{bmatrix} -A\phi m & 0 & 0 & -A\rho_2 \\ A(\rho_f - \phi m) & 0 & 0 & A\rho_1 \\ 0 & 0 & -A\phi m & 0 \\ 0 & 0 & A(\rho_f - \phi m) & 0 \end{bmatrix}, \tag{4.51}$$

$$\mathbf{D}^2 = \begin{bmatrix} -(\lambda + 2\mu) & 0 & 0 & 0 \\ -\lambda & 0 & 0 & 0 \\ 0 & 0 & -\mu & 0 \\ M(\alpha - \phi) & M\phi & 0 & 0 \end{bmatrix}, \tag{4.52}$$

$$\mathbf{B} = \begin{bmatrix} \mathbf{0}_4 & \mathbf{D}^3 \\ \mathbf{D}^4 & \mathbf{0}_4 \end{bmatrix} \partial_z, \tag{4.53}$$

$$\mathbf{D}^3 = \begin{bmatrix} 0 & 0 & -A\phi m & 0 \\ 0 & 0 & A(\rho_f - \phi m) & 0 \\ 0 & -A\phi m & 0 & -A\rho_2 \\ 0 & A(\rho_f - \phi m) & 0 & A\rho_1 \end{bmatrix}, \tag{4.54}$$

$$\mathbf{D}^4 = \begin{bmatrix} 0 & 0 & -\lambda & 0 \\ 0 & 0 & -(\lambda + 2\mu) & 0 \\ -\mu & 0 & 0 & 0 \\ 0 & 0 & M(\alpha - \phi) & M\phi \end{bmatrix}, \tag{4.55}$$

$$\mathbf{C} = \begin{bmatrix} \mathbf{I}_4 & \mathbf{0}_4 \\ \mathbf{0}_4 & \mathbf{D} \end{bmatrix} \partial_t, \qquad \mathbf{D} = \begin{bmatrix} 1 & 0 & 0 & \alpha \\ 0 & 1 & 0 & \alpha \\ 0 & 0 & 1 & 0 \\ 0 & 0 & 0 & 1 \end{bmatrix}, \tag{4.56}$$

The model parameters have been explained in chapter 3. $\rho_1 = (1 - \phi)\rho_s$ and $\rho_2 = \phi\rho_f$ are the mass per unit volume of aggregate for the solid phase and the fluid phase, respectively. When the porosity $\phi = 0$, the forward operator f is able to map the elastic wavefields. The symbol $\mathbf{0}_n$ represents the $n \times n$ zero matrix, while $\mathbf{I}_n$ is the identity matrix. Suppose that a corresponding first-order perturbation is applied on a random parameter of the reference model $\mathbf{m}_0$, the scattered wavefields δu perturbated by single parameter $\delta\mathbf{m}^{PSV}$ are obtained by Eqs. 4.43, 4.47 under Born approximation.

$$\begin{aligned} \delta\mathbf{m}^{PSV} &\in \{\delta\lambda, \delta\mu, \delta\rho_s, \delta\rho_f, \delta K_s, \delta K_f, \delta\phi\}, \\ \delta\mathbf{s}'_{PSV} &\in \{\delta\mathbf{s}'_\lambda, \delta\mathbf{s}'_\mu, \delta\mathbf{s}'_{\rho_s}, \delta\mathbf{s}'_{\rho_f}, \delta\mathbf{s}'_{K_s}, \delta\mathbf{s}'_{K_f}, \delta\mathbf{s}'_\phi\}. \end{aligned} \tag{4.57}$$

For example, if there is a small scattered variable $\delta\lambda$ added on the reference parameter λ, the corresponding excitation of the scattered wavefields can be summarized as Eq. 4.58 after derivation, which is one of the first-order scattering pulses for poroelastic P-SV equations. The perturbated body such as $\delta\lambda$ can be treated as a point scatterer when the size of the scatterer is much smaller than the wavelength (Wu and Aki 1989). ${\mathbf{u}_0}^{PSV}$ is the reference unperturbed wavefield following the rules in Eqs. 4.39 and 4.48. Similarly, based on Eq. 4.57, the explicit expressions of secondary sources $\mathbf{s}'$, for the remained single perturbated parameter in the fluid-saturated isotropic porous medium are derived and obtained in Eqs. 4.58-4.64.

$$\delta \mathbf{s}'_{\lambda} = \underbrace{\begin{bmatrix} & & & & & & \\ & & & & & & \\ & & & & & & \\ & & & & & & \\ \partial_x & 0 & \partial_z & 0 & \cdots & 0 & \frac{1}{K_s}\partial_t \\ \partial_x & 0 & \partial_z & 0 & \cdots & 0 & \frac{1}{K_s}\partial_t \\ 0 & & & \cdots & & & 0 \\ \frac{M}{K_s}\partial_x & 0 & \frac{M}{K_s}\partial_z & 0 & \cdots & 0 & \frac{M}{K_s^2}\partial_t \end{bmatrix}}_{(8\times8)} \mathbf{u_0}^{PSV}, \tag{4.58}$$

$$\delta \mathbf{s}'_{\mu} = \underbrace{\begin{bmatrix} & & & & & & & \\ & & & & & & & \\ & & & & & & & \\ & & & & & & & \\ 2\partial_x & 0 & \cdots & 0 & \cdots & 0 & \frac{2}{3K_s}\partial_t \\ 0 & 0 & 2\partial_z & 0 & \cdots & 0 & \frac{2}{3K_s}\partial_t \\ \partial_z & 0 & \partial_x & 0 & \cdots & & 0 \\ \frac{2M}{3K_s}\partial_x & 0 & \frac{2M}{3K_s}\partial_z & 0 & \cdots & 0 & \frac{2M}{3K_s^2}\partial_t \end{bmatrix}}_{(8\times8)} \mathbf{u_0}^{PSV}, \tag{4.59}$$

$$\delta \mathbf{s}'_{\rho_s} = -A\rho_f(1-\phi) \underbrace{\begin{bmatrix} \tau\partial_t & 0 & \cdots & & & 0 \\ (\tau-1)\partial_t & 0 & \cdots & & & 0 \\ 0 & 0 & \tau\partial_t & 0 & \cdots & 0 \\ 0 & 0 & (\tau-1)\partial_t & 0 & \cdots & 0 \\ & & & & & \\ & & & & & \\ & & & & & \\ & & & & & \end{bmatrix}}_{(8\times8)} \mathbf{u_0}^{PSV}, \tag{4.60}$$

$$\delta \mathbf{s}'_{\rho_f} = A \underbrace{\begin{bmatrix} -(\tau-1)\rho_2\partial_t & 0 & \cdots & & & & 0 \\ (\tau-1)\rho_1\partial_t & -\frac{1}{A\rho_f}\partial_t & 0 & \cdots & & & 0 \\ 0 & 0 & -(\tau-1)\rho_2\partial_t & 0 & \cdots & & 0 \\ 0 & 0 & (\tau-1)\rho_1\partial_t & -\frac{1}{A\rho_f}\partial_t & 0 & \cdots & 0 \\ & & & & & & \\ & & & & & & \\ & & & & & & \\ & & & & & & \end{bmatrix}}_{(8\times8)} \mathbf{u_0}^{PSV}, \tag{4.61}$$

$$\delta \mathbf{s}'_{K_s} = \frac{\alpha - 1}{K_s} \underbrace{\begin{bmatrix} & & & & & & & \\ & & & & & & & \\ & & & & & & & \\ 0 & & \cdots & & & 0 & & \partial_t \\ 0 & & \cdots & & & 0 & & \partial_t \\ 0 & & & & \cdots & & & 0 \\ M\partial_x & 0 & M\partial_z & 0 & \cdots & 0 & & M\frac{1-2\alpha+\phi}{K_s(1-\alpha)}\partial_t \end{bmatrix}}_{(8\times 8)} \mathbf{u_0}^{PSV}, \tag{4.62}$$

$$\delta \mathbf{s}'_{K_f} = \underbrace{\begin{bmatrix} & & & \\ & & & \\ & & & \\ & & & \\ & & & \\ 0 & \cdots & 0 & \frac{\phi M}{K_f^2}\partial_t \end{bmatrix}}_{(8\times 8)} \mathbf{u_0}^{PSV}, \tag{4.63}$$

$$\delta \mathbf{s}'_{\phi} = A\rho_f \underbrace{\begin{bmatrix} \tau\rho_s\partial_t & -\tau\rho_f\partial_t & 0 & \cdots & & & 0 \\ (\tau-1)\rho_s\partial_t & -(\tau-1)\rho_f\partial_t & 0 & \cdots & & & \vdots \\ 0 & 0 & \tau\rho_s\partial_t & -\tau\rho_f\partial_t & 0 & \cdots & \\ 0 & 0 & (\tau-1)\rho_s\partial_t & -(\tau-1)\rho_f\partial_t & 0 & \cdots & 0 \\ & & & & & & \\ & & & & & & \\ \frac{\alpha M}{A\rho_f\phi}\partial_x & 0 & \frac{\alpha M}{A\rho_f\phi}\partial_z & 0 & \cdots & 0 & \frac{\alpha M}{A\rho_f\phi K_s}\partial_t \end{bmatrix}}_{(8\times 8)} \mathbf{u_0}^{PSV}. \tag{4.64}$$

Consequently, the gradients of misfit functional $\mathcal{J}$ with respect to the model parameters in P-SV equations are obtained by Eq. 4.46, and the results coincide with the explicit expressions in section 4.1.1.

4.2.2. Gradients and first-order scattering pulses in poroelastic SH/Love wave equations

Similarly, the forward operator for SH wave equations

$$\mathbf{L}^{SH} = \mathbf{M} + \mathbf{N} + \mathbf{P}, \tag{4.65}$$

and

$$\mathbf{M} = \begin{bmatrix} 0 & -A\phi m & 0 \\ -\mu & 0 & 0 \\ 0 & 0 & 0 \end{bmatrix} \partial_x, \qquad \mathbf{N} = \begin{bmatrix} 0 & 0 & -A\phi m \\ 0 & 0 & 0 \\ -\mu & 0 & 0 \end{bmatrix} \partial_z, \tag{4.66}$$

$$\mathbf{P} = \mathbf{I}_3 \partial_t. \tag{4.67}$$

Following the Eq. 4.43, the data space

$$\mathbf{u}^{SH} = (v_y, \sigma_{xy}, \sigma_{zy})^{\mathrm{T}}, \tag{4.68}$$

and the scattered model parameter

$$\mathbf{m}^{SH} \in \{\delta\mu, \delta\rho_s, \delta\rho_f, \delta\phi\}. \tag{4.69}$$

The corresponding scattering pulse

$$\delta\mathbf{s}'_{SH} \in \{\delta\mathbf{s}^{SH}_{\mu}, \delta\mathbf{s}^{SH}_{\rho_s}, \delta\mathbf{s}^{SH}_{\rho_f}, \delta\mathbf{s}^{SH}_{\phi}\}. \tag{4.70}$$

Upon using Born approximation, the explicit first-order scattering pulses for poroelastic SH equations are derived in Eqs.

$$\delta\mathbf{s}^{SH}_{\mu} = \underbrace{\begin{bmatrix} & & \\ \partial_x & 0 & 0 \\ \partial_z & 0 & 0 \end{bmatrix}}_{(3\times3)} \mathbf{u_0}^{SH}, \tag{4.71}$$

$$\delta\mathbf{s}^{SH}_{\rho_s} = -AT\rho_f(1-\phi) \underbrace{\begin{bmatrix} \partial_t & 0 & 0 \\ & & \\ & & \end{bmatrix}}_{(3\times3)} \mathbf{u_0}^{SH}, \tag{4.72}$$

$$\delta\mathbf{s}^{SH}_{\rho_f} = -A(\tau-1)\rho_2 \underbrace{\begin{bmatrix} \partial_t & 0 & 0 \\ & & \\ & & \end{bmatrix}}_{(3\times3)} \mathbf{u_0}^{SH}, \tag{4.73}$$

$$\delta\mathbf{s}^{SH}_{\phi} = -A\rho_f[(\tau-1)\rho_f - \tau\rho_s] \underbrace{\begin{bmatrix} \partial_t & 0 & 0 \\ & & \\ & & \end{bmatrix}}_{(3\times3)} \mathbf{u_0}^{SH}. \tag{4.74}$$

Here, $\mathbf{u_0}^{SH}$ represents the reference unperturbed wavefield following the rules in Eqs. 4.39 and 4.68. All the parameters have been explained in chapter 3. Thus, the gradients of misfit functional $\mathcal{J}$ with respect to the model parameter $\mathbf{m}^{SH}$ can be obtained from Eq. 4.46 and are same with the results in section 4.1.2.

Part III.

Sensitivity analysis

5

Single-scattering problem

The subsurface materials can be decomposed into the background medium and the perturbations. The scattered wavefields generated by small diffractors can give direct insight into the sensitivity of different parameters (Wu and Aki 1989). Although the wavefront shapes of the scattered wavefields can be described by the radiation patterns, which build a connection between the incident and scattering angles (Operto et al. 2013; Q. Yang, Malcolm, et al. 2018), the radiation patterns of surface waves also depend on the source depth and frequencies, which makes difficulties on the analytical derivation of the radiation patterns concerns surface waves (Ben-Menahem and Harkrider 1964). Alternatively, the scattered wavefields from diffractor points concerned with various model parameters can be derived explicitly and numerically visualized from a certain incident angle (T. Liu and T. Bohlen 2022b).

It shows in section 4.2 that the total fields $\mathbf{u}$ can be decomposed into the primary fields $\mathbf{u_0}$ and scattered fields $\delta\mathbf{u}$ linearly under Born approximation. The signal of the scattering point can be calculated based on the unperturbed wavefields $\mathbf{u_0}$. Besides, the scattered wavefields are generated from the same forward operator $\mathbf{L}$ and solved by the FDTD method afterward. Since the scattering source signals are changed with various perturbed parameters, the scattering wavefields for different parameters will be obtained separately.

5.1. Analysis of scattered wavefield produced by individual model parameter perturbations

In this part, a series of scattering tests are implemented on a $45m \times 9m$ poroelastic half space to detect the effects of the model parameters on the different wave types. The explicit expressions of the scattering point corresponding to various model parameters are shown in section 4.2. By solving Eqs. 4.47-4.74 with the FDTD method, both the incident and scattered wavefields are simulated numerically. A Ricker wavelet triggers the unperturbed shallow poroelastic subsurface with a center frequency of 40 Hz at the free surface. To make sure the waveforms are comparable and surface waves are fully generated, the scattering point (Eqs. 4.57

and 4.70) is set in the middle of the free surface as well. Poroelastic model parameters can be found in Table 5.1.

	Parameter	**Symbol**	**Unit**	**Value**
Grain	Bulk modulus	K_s	Pa	0.7×10^{10}
	Density	ρ_s	kg/m³	2650
Matrix	Bulk modulus	K_d	Pa	5.1×10^8
	Shear modulus	μ	Pa	3.45×10^8
	Porosity	ϕ	/	0.2
	Tortuosity	τ	/	2
Fluid	Bulk modulus	K_f	Pa	2.2×10^9
	Density	ρ_f	kg/m³	1000
	Viscosity	η	N·s/m²	-
Velocity	Fast P wave	V_{fp}	m/s	1562.23
	Slow P wave	V_{sp}	m/s	303.17
	Shear wave	V_s	m/s	394.21

Table 5.1.: Rock properties of the fluid-saturated porous medium for analyzing parameter sensitivities.

Fig. 5.1 shows snapshots of the undisturbed primary shallow-seismic PSV&SH wavefields $\mathbf{u_0}$. Taking the wave information from the solid phase as examples, the scattered wavefields $\delta\mathbf{u}$ corresponding to different model parameters are shown in Fig. 5.2 for the P-SV scheme and Fig. 5.3 for the SH scheme. Both for P-SV and SH cases, scattered waveform comparisons from a single trace are shown in Figs 5.4 and 5.5 separately. The number of the model parameters in the SH scheme is reduced since the main stress is not considered. The wave amplitude of the scattered wavefields in the P-SV and SH schemes is shown consistently to make a comparison.

Different wave types in the shallow P-SV&SH poroelastic wavefields have been shown in Fig. 5.1. As shown in Fig. 5.3, there is only shear wave from the SH scheme in a homogeneous half-space, and it shows the slightest perturbation from a scattering point of the fluid density ρ_f. Shear modulus μ and solid grain density ρ_s take the main responsibility for the shear wave, while porosity has a relatively small effect. When it turns to the P-SV scheme in Fig. 5.2, Rayleigh wave and compressional waves are generated in the meantime. The fast-P wave propagates in the fastest way with relatively small energy. Besides, the velocities of the P wave and S wave have a significant difference since the subsurface is poroelastic, which is consistent with the scattered result from $\delta\phi$ that porosity of the subsurface can influence body waves sensitively. Solid bulk modulus K_s shows minor effects on

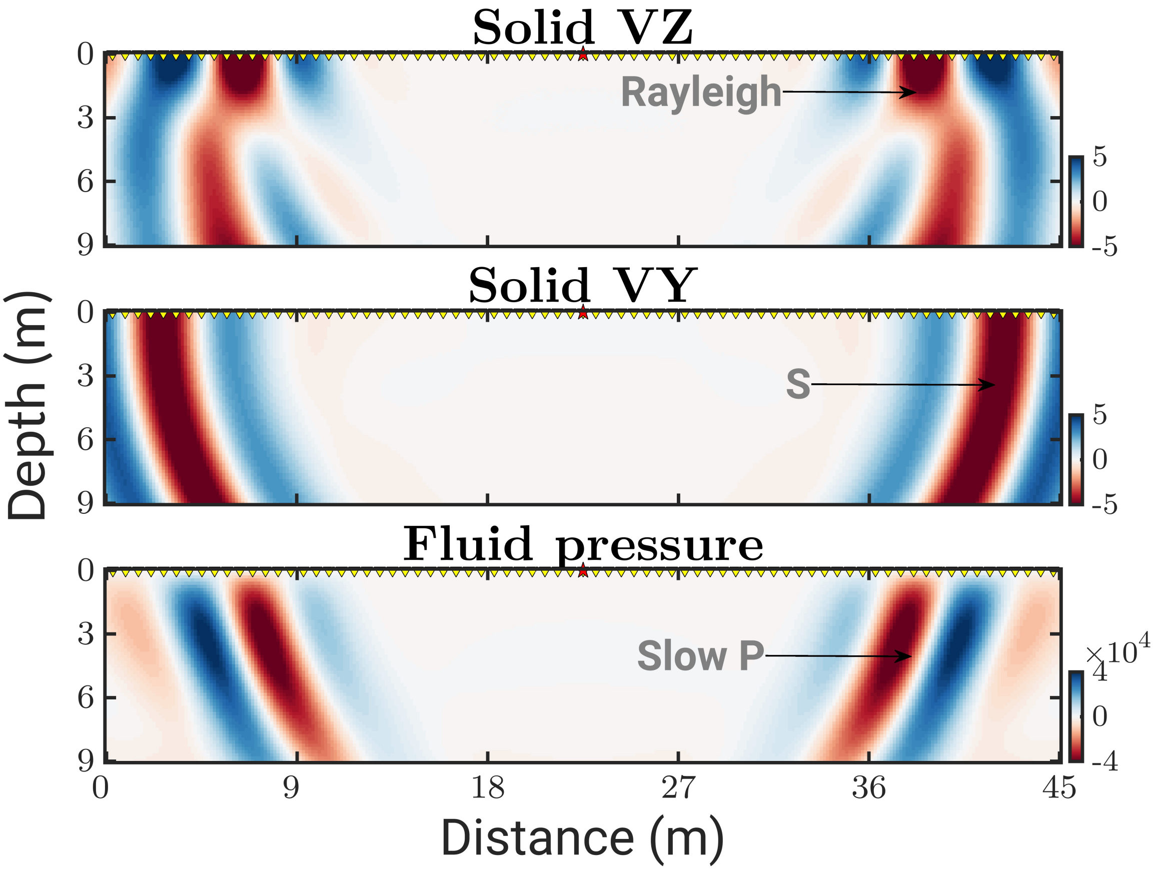

Figure 5.1.: Snapshots of the undisturbed shallow-seismic poroelastic PSV&SH wavefields at 90 ms: triggered by Ricker wavelet with a center frequency of 40 Hz.

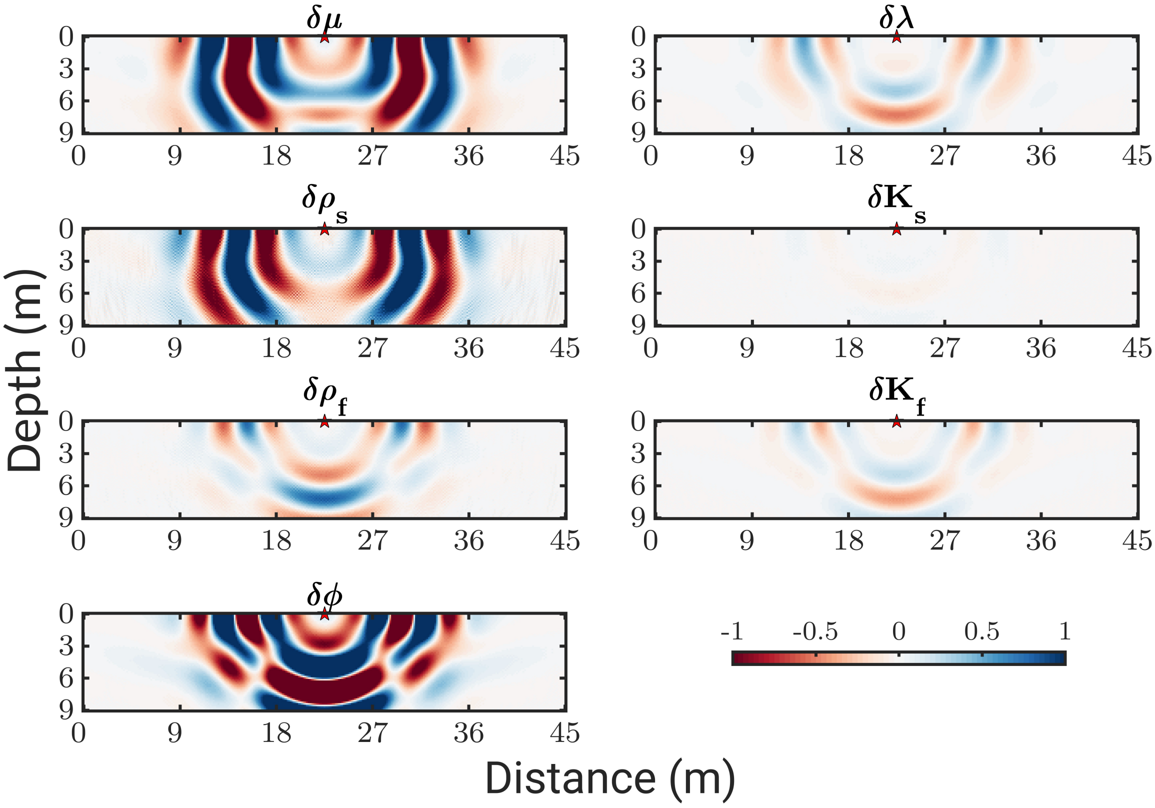

Figure 5.2.: Shallow-seismic scattered P-SV poroelastic wavefields (Solid profile in vertical direction Z) corresponding to different model parameters with 5% perturbations. The red star represents the location of the point diffractor.

the shallow poroelastic wavefields. Fluid bulk modulus K_f and fluid density ρ_f take response for shear wave slightly. Furthermore, porosity ϕ is quite sensitive to both shear and compressional waves. A similar analysis also can be told from the single-trace waveform comparison in Figs 5.4 and 5.5. The results indicate the potential trade-off relations between parameters during multi-parameter FWI. Based on the physical condition in the poroelastic medium, the parameters with fewer similarities in the radiation patterns are likely to be recovered together.

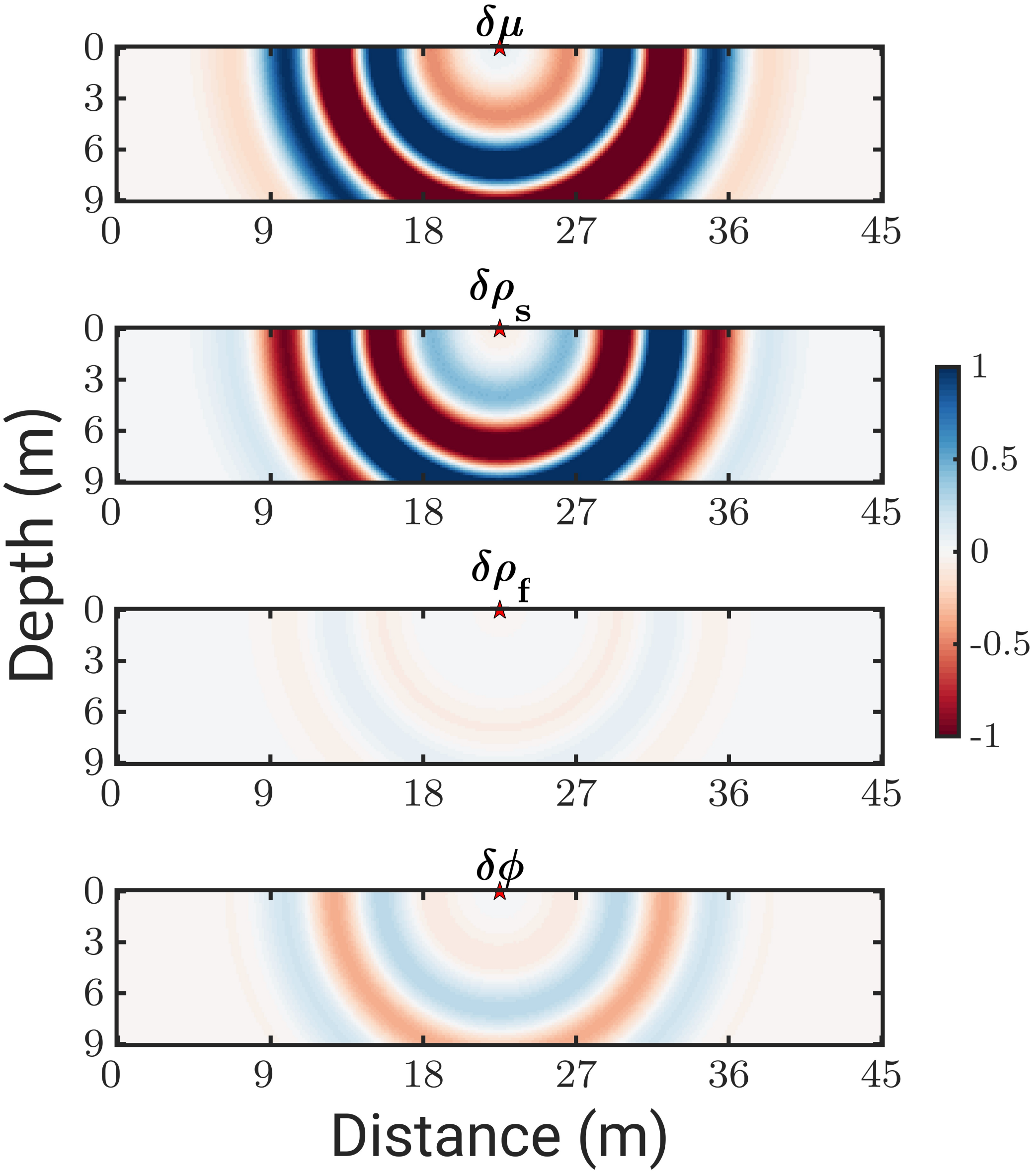

Figure 5.3.: Shallow-seismic scattered SH poroelastic wavefields (Solid profile in horizontal direction Y) corresponding to different model parameters with 5% perturbations.

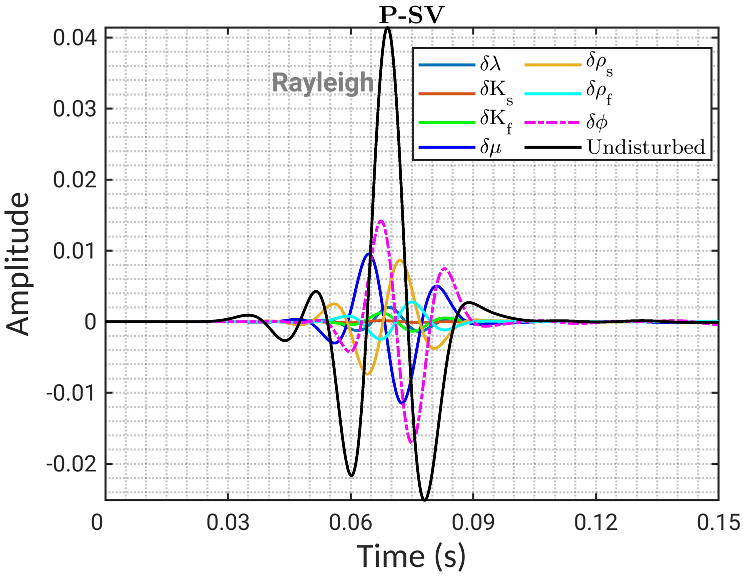

Figure 5.4.: Scattered single-trace waveform comparison from P-SV scheme: vertical-component velocity of the solid phase. The receiver is on the free surface at offset = 10.8 m in Fig. 5.2, and the black line represents the unperturbed reference waveform from the homogeneous poroelastic background at the same position.

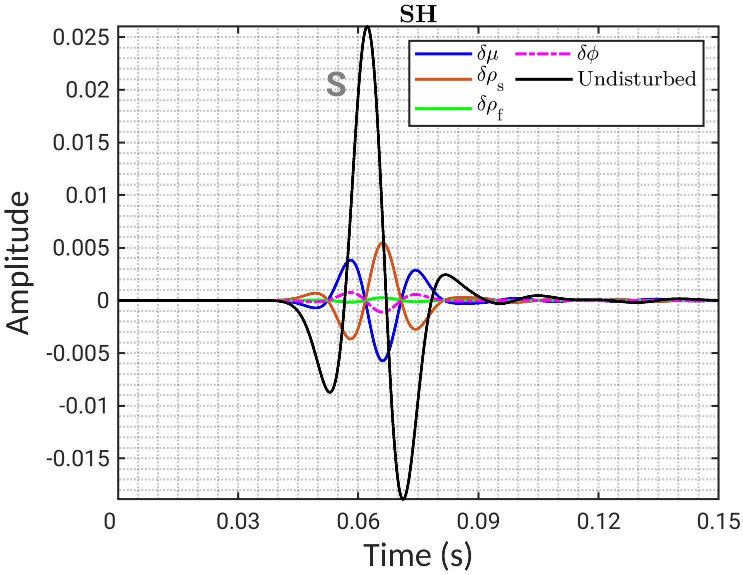

Figure 5.5.: Scattered single-trace waveform comparison from SH scheme: horizontal-component velocity of the solid phase. The receiver is on the free surface at offset = 10.8 m in Fig. 5.3, and the black line represents the unperturbed reference waveform from the homogeneous poroelastic background at the same position.

6

Sensitivity kernels

The effects of different model parameters on the waveforms are evaluated from the analysis of the scattering problem in chapter 5. As complements, the sensitivity of the various model parameters to the data space can be detected from the corresponding sensitivity kernels, which are the hearts of the related gradients as well. Besides, the explicit full expressions of the gradients have been derived in chapter 4. To clarify the effects of various wave types on the model parameters, the primary sensitivity kernels in a shallow poroelastic subsurface are numerically calculated both in P-SV and SH equations. The numerical model is a homogeneous poroelastic half-space, with a circular anomaly within the Fresnel zone. For concerns about shallow-subsurface detection, surface waves are considered. The acquisition geometry is set as the same as chapter 5 within the duration time of 15 ms, and the parameters can be found in Table 5.1.

The kernels' galleries can show the wavepaths for different scattering bodies. The updates along the raypath give contribute to the background values and source frequencies heavily affect the minor radius of the first-Fresnel zone. Unlike the traditional reflected wave exploration which concerns more reflections beyond the raypath, surface waves will travel along the free surface and the long wavelength parts on the fast P wave are less involved for shallow seismic detection. According to the wavelength Λ, here, the sequences of main wave types are $\Lambda_s > \Lambda_{Love} > \Lambda_{Rayleigh}$, and $\Lambda_s > \Lambda_{sp}$.

6.1. Fre´chet kernels K_λ, K_{K_s}, K_{K_f} involving Rayleigh waves

Fig. 6.1 shows the galleries of the sensitivity kernels for λ, K_s, and K_f, which are only considered in the P-SV case. It indicates λ concerns more on the Rayleigh waves compared to K_s and K_f, while K_s and K_f are more sensitive to the compressional waves. Especially, K_s mainly gets benefits from the long wavelength components, which gives less contribution to the shallow seismic wavefields. K_f mainly concerns the slow-P wave, which will be attenuated in a viscous porous media within the seismic band.

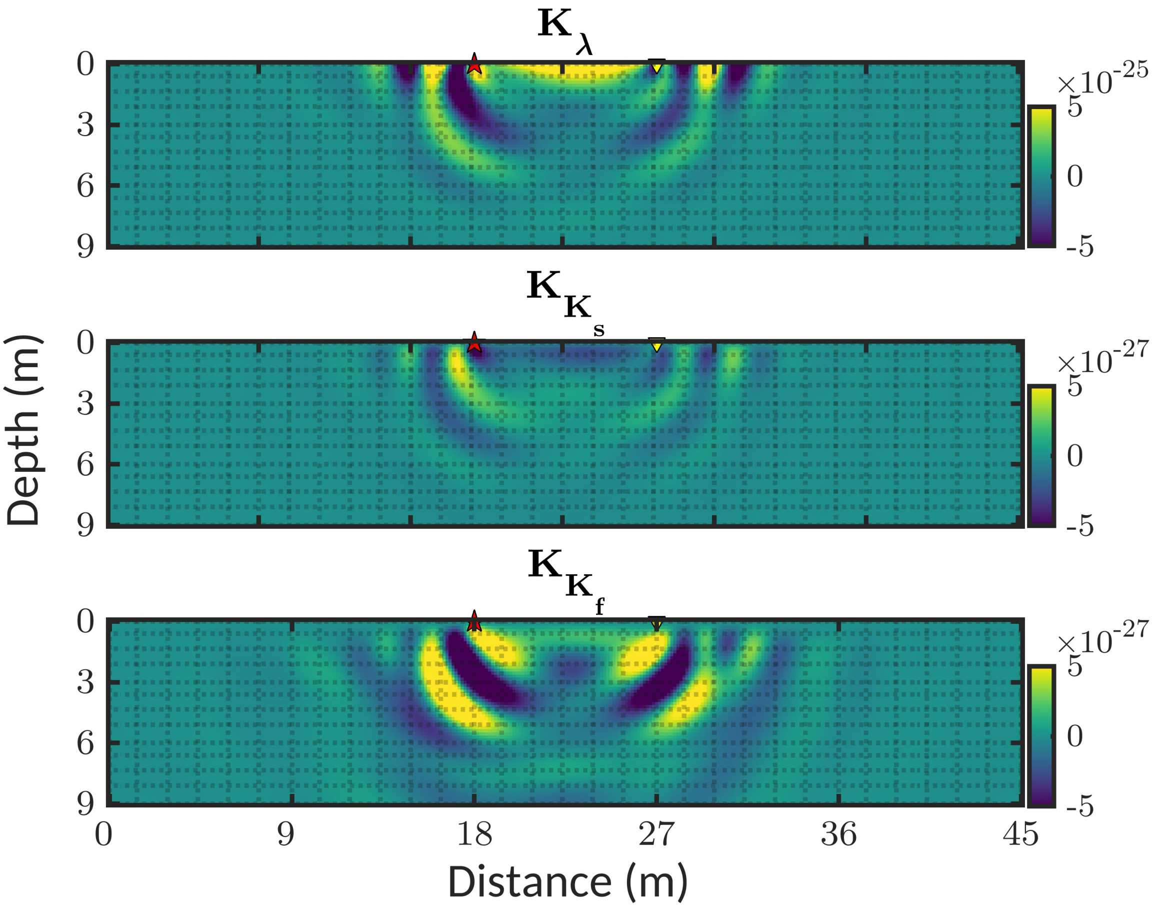

Figure 6.1.: Fréchet kernels involving Rayleigh waves in P-SV for λ, K_s, and K_f: The red star is the location of the forward source, and the inverted triangle represents the adjoint source. Both are located at the free surface.

6.2. Comparison of Fréchet kernels in P-SV and SH equations

Fig. 6.2 contains the sensitivity kernels of μ, ρ_s, ρ_f, and ϕ in P-SV and SH profiles. The galleries of the same parameter are shown consistently for comparison. Compared to ρ_f and ϕ, it is clear in SH that μ and ρ_s are more sensitive to the shear wave components and the main energy of K_μ^{SH} distribute along the free surface. ρ_f shows less effects from shear wave components, but K_{ρ_f} indicates ρ_f is sensitive to the slow-P wave modes. Similarly, K_ϕ^{SH} and K_ϕ tell that ϕ takes response for shear wave but is also sensitive to P waves, especially the slow-P wave. Since Rayleigh waves are coupled from compressional waves and shear wave in the P-SV profile, ϕ also makes substantial contributions to surface waves.

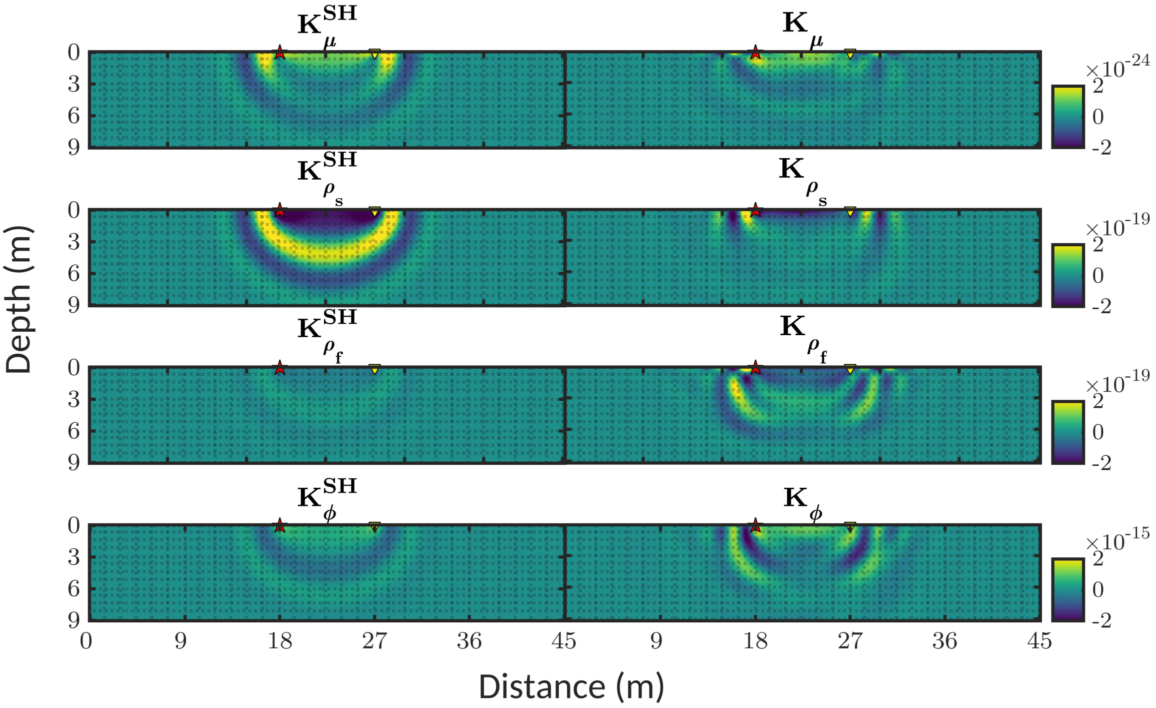

Figure 6.2.: Fréchet kernels in SH & P-SV for μ, ρ_s, ρ_f, and ϕ: surface waves are involved. Geometry is the same as in Figure 6.1.

7

Trade-off analysis

To prepare an approach for the multi-parameter inversion in fluid-saturated poroelastic media, the similarity of the sensitivities of the data to vary parameters needs to be investigated (Métivier et al. 2014). As derived in chapter 4, the explicit expressions for kernels of the gradients in P-SV and SH formats are also given by Eqs. 4.22-4.28 and 4.35-4.38 separately. According to the derivations in chapter 4, it is known that the correlations between the gradients of different parameters can not be eliminated under the assumption of Born approximation. Because the subsurface parameters are reconstructed simultaneously during the multi-parameter inversion, how to minimize the cross-talk issue and implement an applicable inversion strategy are difficult tasks. Unlike the acoustic and elastic FWI, where fewer parameters can be handled flexibly with parameterizations, we seek to divide the poroelastic parameters with low correlations into the same groups for multi-parameter inversion.

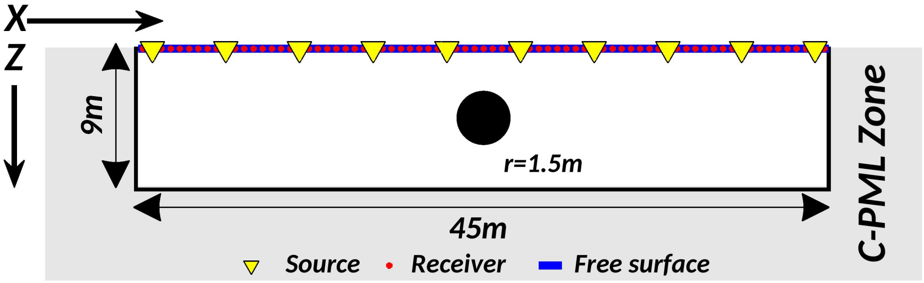

Figure 7.1.: Acquisition geometry for a shallow poroelastic inclusion model. Horizontal Y component for SH equations is considered as well.

In this chapter, a series of numerical tests on the gradients of model parameters for the anomaly model in Fig. 7.1 are performed to explore the correlations of their patterns. The acquisition and model parameters are the same as in chapter 5. The inclusion model parameters are changed individually. I vary the interference parameter of the anomaly body at the same location in the inclusion model and cross-compare the corresponding influences between the gradient patterns of other parameters. The analysis based on Figs 7.2-7.8 can provide insights into the parameterization of multi-parameter PFWI.

7.1. Correlation tests of gradient gallery in P-SV equations

Although the values of the gradients depend on the magnitude of the related material parameters, the descent direction from the gradient panels still can indicate the correlations.

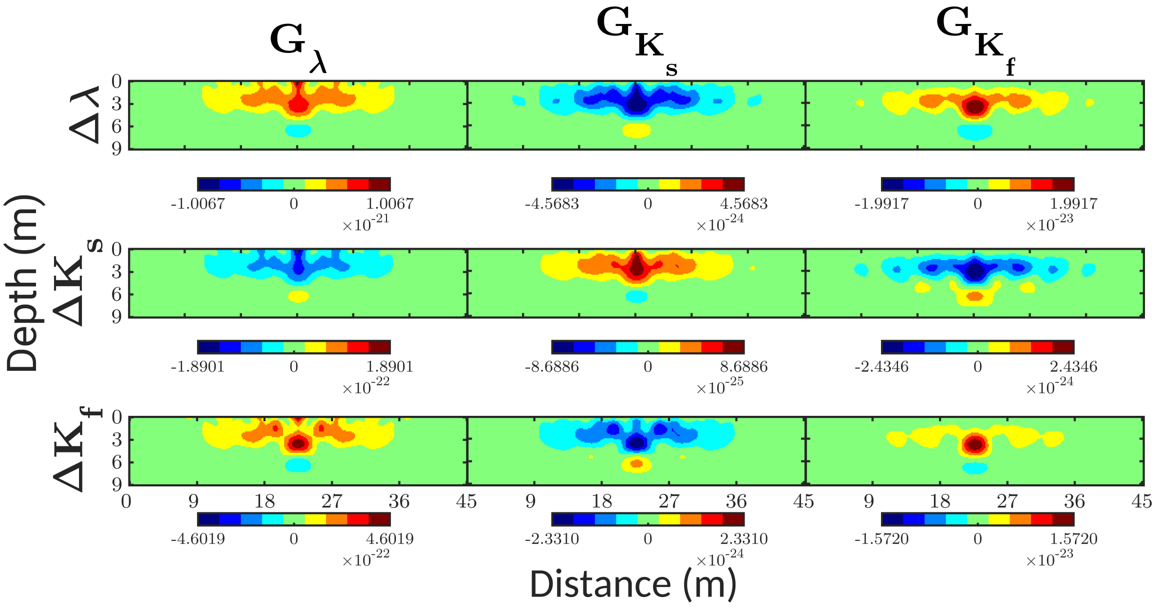

Figure 7.2.: Gradient gallery in P-SV for correlation test in section 7.1: $\{\Delta\lambda, \Delta K_s, \Delta K_f\} \rightarrow \{G_\lambda, G_{K_s}, G_{K_f}\}$ involving Rayleigh waves. The model geometry is shown in Fig. 7.1, and the parameters are listed in Table 5.1, which are the same as the followings.

7.2-7.4 present the correlations in P-SV equations. To make clear evaluations, all the panels are scaled with their absolute maximum values, which indicate the descent directions as well. To mitigate the footprint from the sources and receivers, all the gradients are tapered by an error function.

The location of the absolute extreme in gradient G is likely to be closer to the surface if the related parameter has more impact on the surface waves. The key point of achieving good results by multi-parameter inversion is to recover the parameters with less coherency. For example, Fig. 7.2 shows a map from disturbance $\{\Delta\lambda, \Delta K_s, \Delta K_f\}$ in the anomaly to the gradients $\{G_\lambda, G_{K_s}, G_{K_f}\}$ obtained from the P-SV poroelastic model. $\Delta\lambda \rightarrow G_{K_f}$ and $\Delta K_f \rightarrow G_\lambda$ indicate a strong coherency between λ and K_f, while the panels of $\Delta\lambda \rightarrow G_{K_s}$ and $\Delta K_s \rightarrow G_\lambda$ show less similarities. $\Delta K_f \rightarrow G_{K_s}$ and $\Delta K_s \rightarrow G_{K_f}$ are similar, but their descent directions are opposite. The results indicate that λ and K_s will be better to be considered in

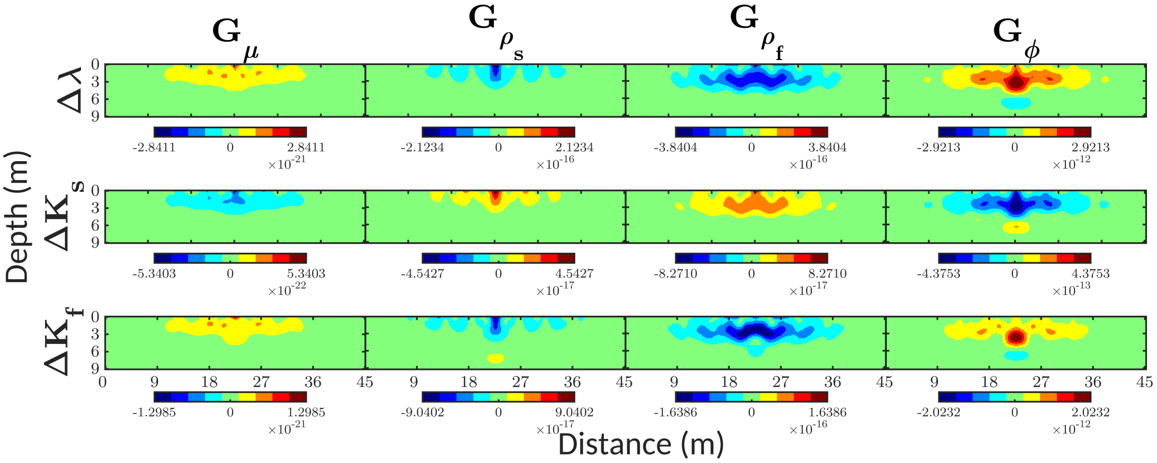

Figure 7.3.: Gradient gallery in P-SV for correlation test in section 7.1: $\{\Delta\lambda, \Delta K_s, \Delta K_f\} \longrightarrow \{G_\mu, G_{\rho_s}, G_{\rho_f}, G_\phi\}$ involving Rayleigh waves.

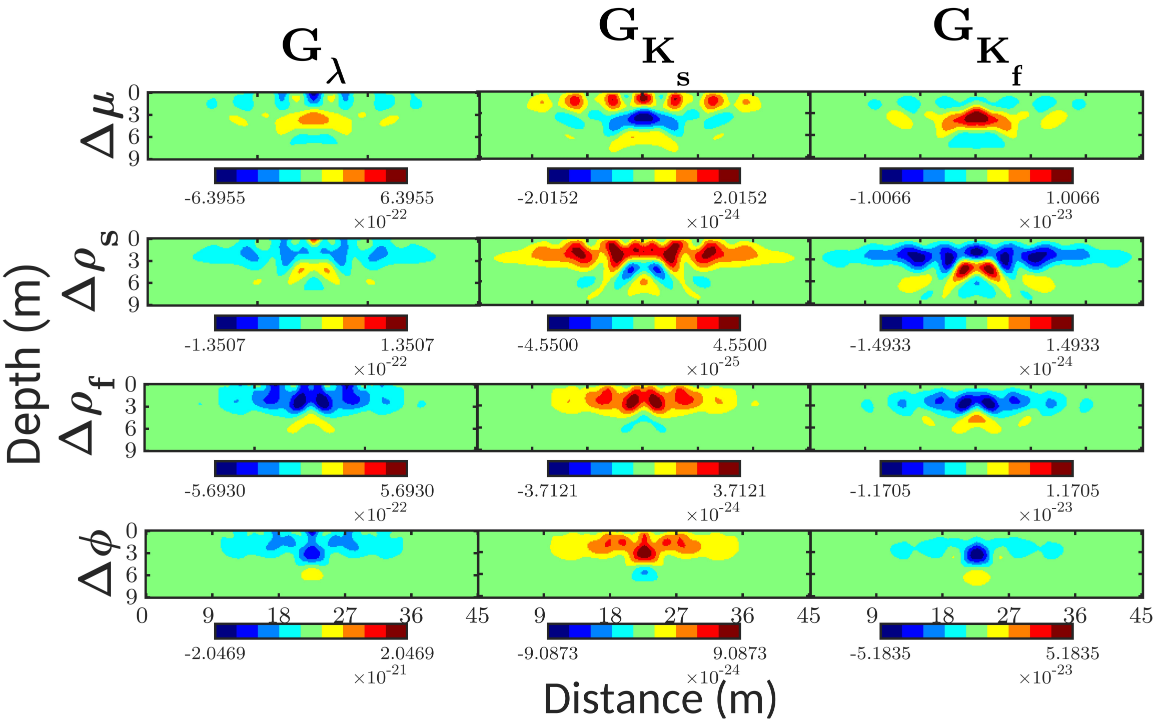

Figure 7.4.: Gradient gallery in P-SV for correlation test in section 7.1: $\{\Delta\mu, \Delta\rho_s, \Delta\rho_f, \Delta\phi\} \longrightarrow \{G_\lambda, G_{K_s}, G_{K_f}\}$ involving Rayleigh waves.

the same group during multi-parameter inversion, and $\{\Delta\lambda, \Delta K_f\}$ should make changes toward the opposite direction of $\{\Delta K_s\}$ to achieve better recovery of the same anomalies.

Figs 7.3 and 7.4 exhibit the maps $\Delta m \longrightarrow G_n$, where $m \in \mathbf{M}$ and $n \in \mathbf{N}$ $(\mathbf{M}, \mathbf{N} \subseteq \{(\lambda, K_s, K_f), (\mu, \rho_s, \rho_f, \phi)\}, \mathbf{M} \neq \mathbf{N})$. By the cross-comparison of G_n mapped from Δm, the gradients performing without concentrated descent direction at the location of the anomaly shows fewer correlations between m and n. For instance, $\Delta m \longrightarrow G_\phi$ and $\Delta\phi \longrightarrow G_n$ indicate that porosity ϕ can raise cross-talk issues easily when inverted together with $m \in (\lambda, K_s, K_f)$. Besides, $\Delta\lambda \longrightarrow G$ and $\Delta K_f \longrightarrow G$ have similar patterns, and the result is consistent with Fig. 7.2. Compared to ρ_f, (μ, ρ_s) have less coherency with (λ, K_s, K_f).

7.2. Cross-comparison of gradient panels in PSV&SH equations

Similarly, Figs 7.5-7.8 display the comparison results of the common parameters in P-SV and SH cases. They present the results of the cross comparison $\Delta m : G_n(m, n \in \{\mu, \rho_s, \rho_f, \phi\})$ in both SH and P-SV cases, while Love wave and Rayleigh waves exist separately. The gradient panels are shown consistently in P-SV and SH. In SH panels, $\Delta\mu \longrightarrow G_n^{SH}(n \in \{\rho_s, \rho_f, \phi\})$ and $\Delta m \longrightarrow G_\mu^{SH}(m \in \{\rho_s, \rho_f, \phi\})$ illustrate that μ is a harmless and essential parameter for multi-parameter PFWI. The panels of $\Delta\rho_s \longrightarrow G_n(n \in \{\mu, \rho_f, \phi\})$ and $\Delta m \longrightarrow G_{\rho_s}(m \in \{\mu, \rho_f, \phi\})$ show the correlations of gradients in P-SV are decreased compared to SH, which indicates it is more realistic to invert ρ_s, μ, and ϕ simultaneously in P-SV PFWI. Besides, G_{ρ_s} and G_{ρ_f} look similar, and the descent direction of G_ϕ and (G_{ρ_s}, G_{ρ_f}) is opposite.

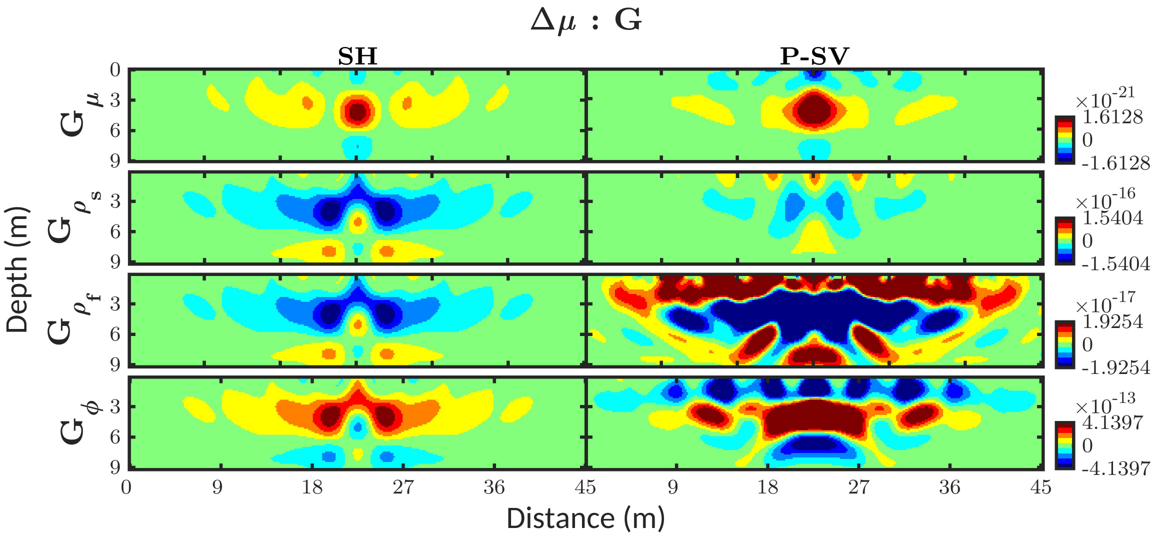

Figure 7.5.: Gradient panel in SH & P-SV for cross-comparison: $\Delta\mu \rightarrow \{G_n, G_n^{SH}\}, n \in \{\mu, \rho_s, \rho_f, \phi\}$.

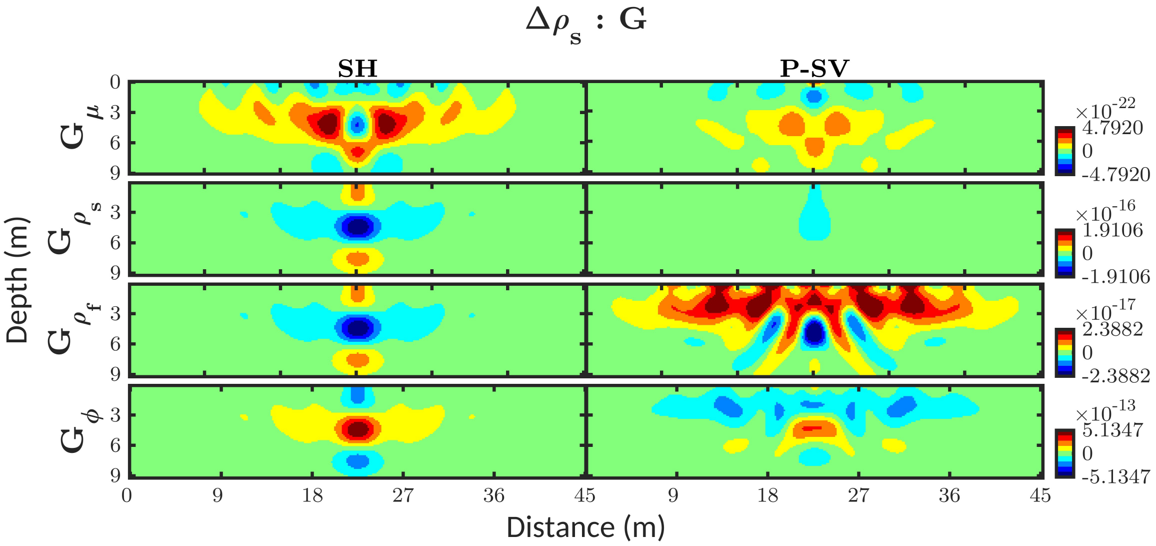

Figure 7.6.: Gradient panel in SH & P-SV for cross-comparison: $\Delta\rho_s \rightarrow \{G_n, G_n^{SH}\}, n \in \{\mu, \rho_s, \rho_f, \phi\}$.

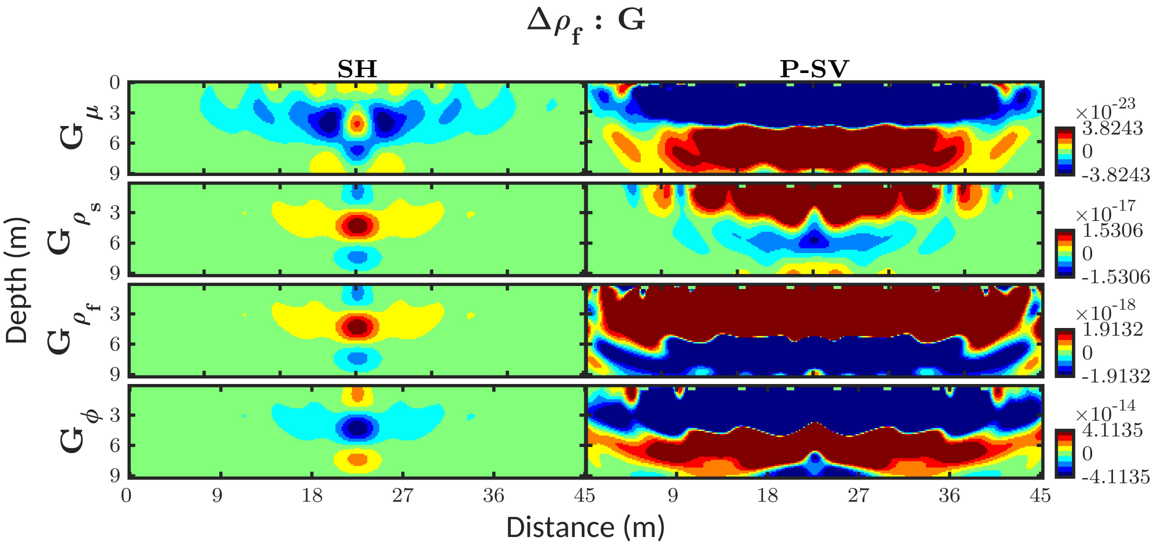

Figure 7.7.: Gradient panel in SH & P-SV for cross-comparison: $\Delta\rho_f \rightarrow \{G_n, G_n^{SH}\}, n \in \{\mu, \rho_s, \rho_f, \phi\}$.

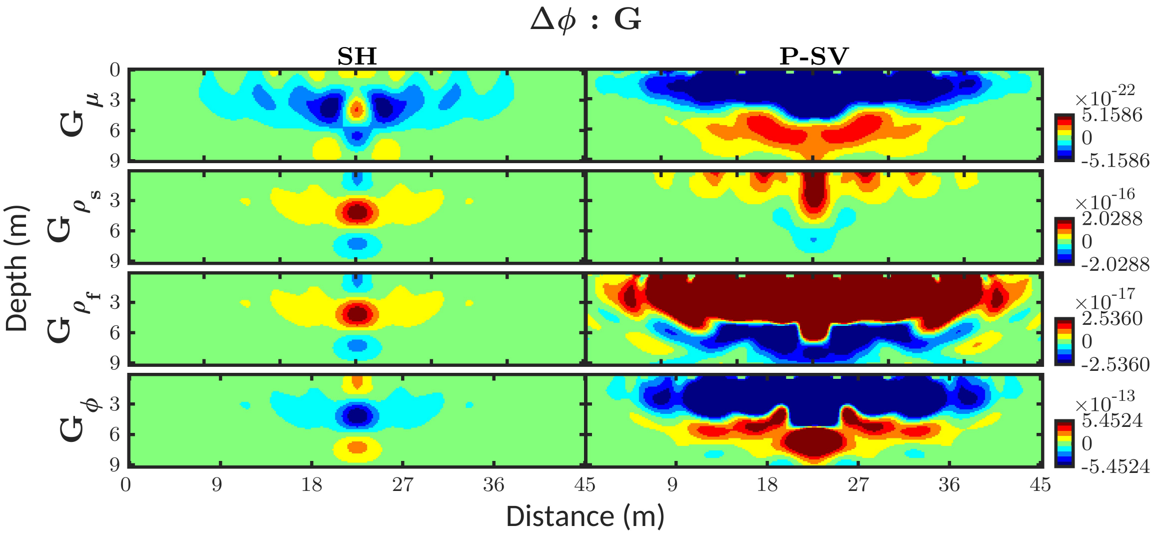

Figure 7.8.: Gradient panel in SH & P-SV for cross-comparison: $\Delta\phi \rightarrow \{G_n, G_n^{SH}\}, n \in \{\mu, \rho_s, \rho_f, \phi\}$.

Part IV.

Numerical reconstructions

8

Mono-parameter poroelastic FWI

Before the application of PFWI to field data, primary numerical reconstruction tests are necessary to validate the inversion results obtained from $IforPoro$, which also help to evaluate the reconstruction abilities of different poroelastic parameters. Based on a known geological model, the "real" seismic data will be generated numerically with the help of a proper acquisition geometry. For mono-parameter inversion, only one unknown parameter is inverted while other model properties are kept constant (T. Liu and T. Bohlen 2022a). In this chapter, there are two poroelastic model examples. One is an inclusion model with a circle anomaly, and the other contains a layered medium. I will investigate the accuracy of Rayleigh&Love wave PFWI workflow and detect the reconstructed performance of different model parameters. To keep fewer interference factors, the optimizations in this thesis are implemented by a preconditioned steepest-descent method. According to the physical unit of parameters, the step length is scaled and estimated by a parabolic curve fitting method (Kurzmann 2012; Nocedal and Wright 2006).

8.1. Inclusion model

Here, the target model (Fig. 8.1) is a $9m \times 45m$ poroelastic shallow subsurface with a circle anomaly in the center. The model background is filled with poroelastic heterogeneities, and the radius of the circle anomaly is 1.5 meters. Table. 8.1 contains the real parameters of the anomaly.

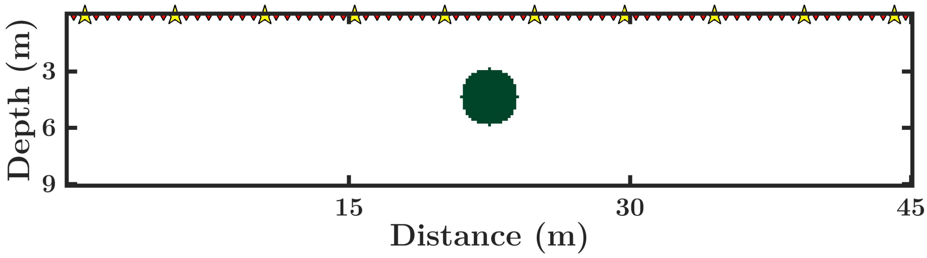

Figure 8.1.: Inclusion model for mono-parameter inversion.

	Parameter	Symbol	Unit	Value
Grain	Bulk modulus	K_s	Pa	0.45×10^{10}
	Density	ρ_s	kg/m³	2950
Matrix	Bulk modulus	K_d	Pa	2.32×10^8
	Shear modulus	μ	Pa	1.8×10^8
	Porosity	ϕ	/	0.24
	Tortuosity	τ	/	2
Fluid	Bulk modulus	K_f	Pa	1.3×10^9
	Density	ρ_f	kg/m³	800
	Viscosity	η	N·s/m²	-

Table 8.1.: Poroelastic parameters of the anomaly.

8.1.1. Inversion setup

To fully generate and detect shallow-seismic wavefields, 10 shots and 75 receivers are set at the free surface. The source interval is 4.8 m, and the trace interval is 0.6 m. Ricker wavelet with a central frequency of 40 Hz is set as the source signal. The total recording time $T = 0.12s$, and time step Δt is 0.05 ms. In P-SV poroelastic equations, the source is vertical point force so that both P-wave and S-wave components can be detected (Fig. 3.2). In SH poroelastic wavefields, the compressional waves vanish, and the source is a shear type. In the numerical modeling with the FD method, the model will be discretized into grids with a space of $\Delta x = \Delta z = 0.15m$. In the recording of seismic data, there is strong energy near the source. To reduce the artifacts from sources, 4 traces near each source are killed during the space integration. To mitigate the footprints from the source location, the gradients are tapered by a circular taper function around the source (Köhn 2011). As introduced in chapter C, the multi-stage strategy applied here is 10-20-30-45-70-120 Hz.

8.1.2. Rayleigh wave PFWI results: λ, K_s, K_f

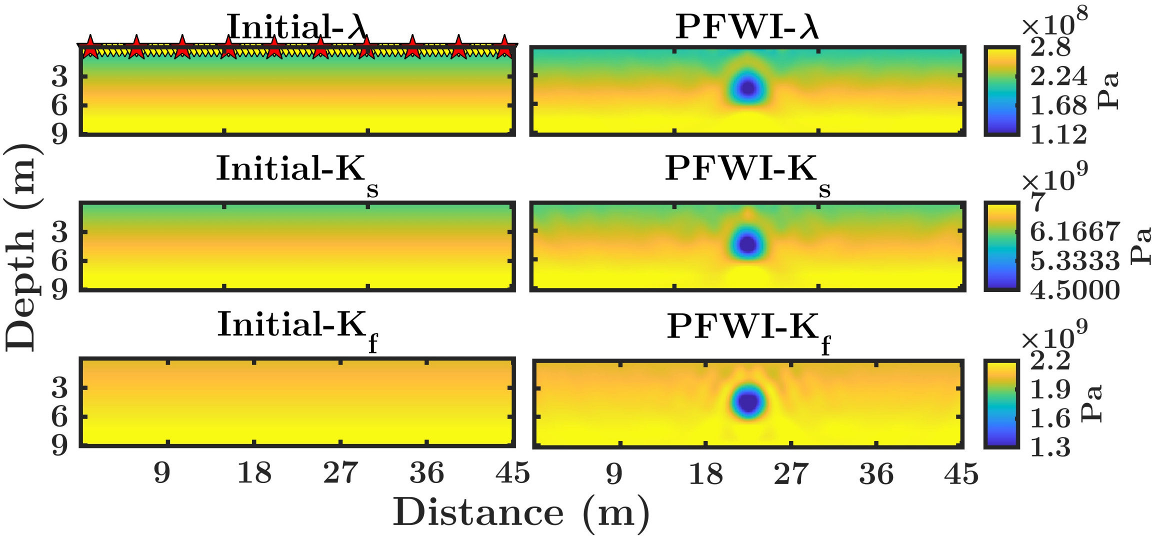

Figure 8.2.: Reconstructed λ, K_s, K_f by Rayleigh wave PFWI. The red stars represent the source location, and invert triangles represent receivers, which are same as the follows.

8.1.3. Reconstruction results comparison of Rayleigh and Love wave PFWI

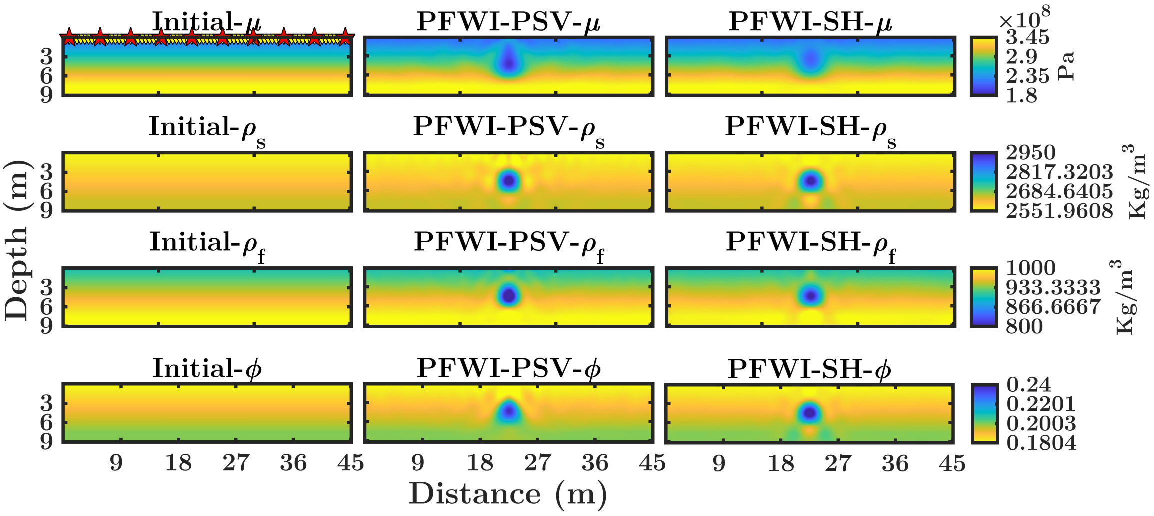

Figure 8.3.: Reconstructed $\mu, \rho_s, \rho_f, \phi$ by Rayleigh&Love wave PFWI.

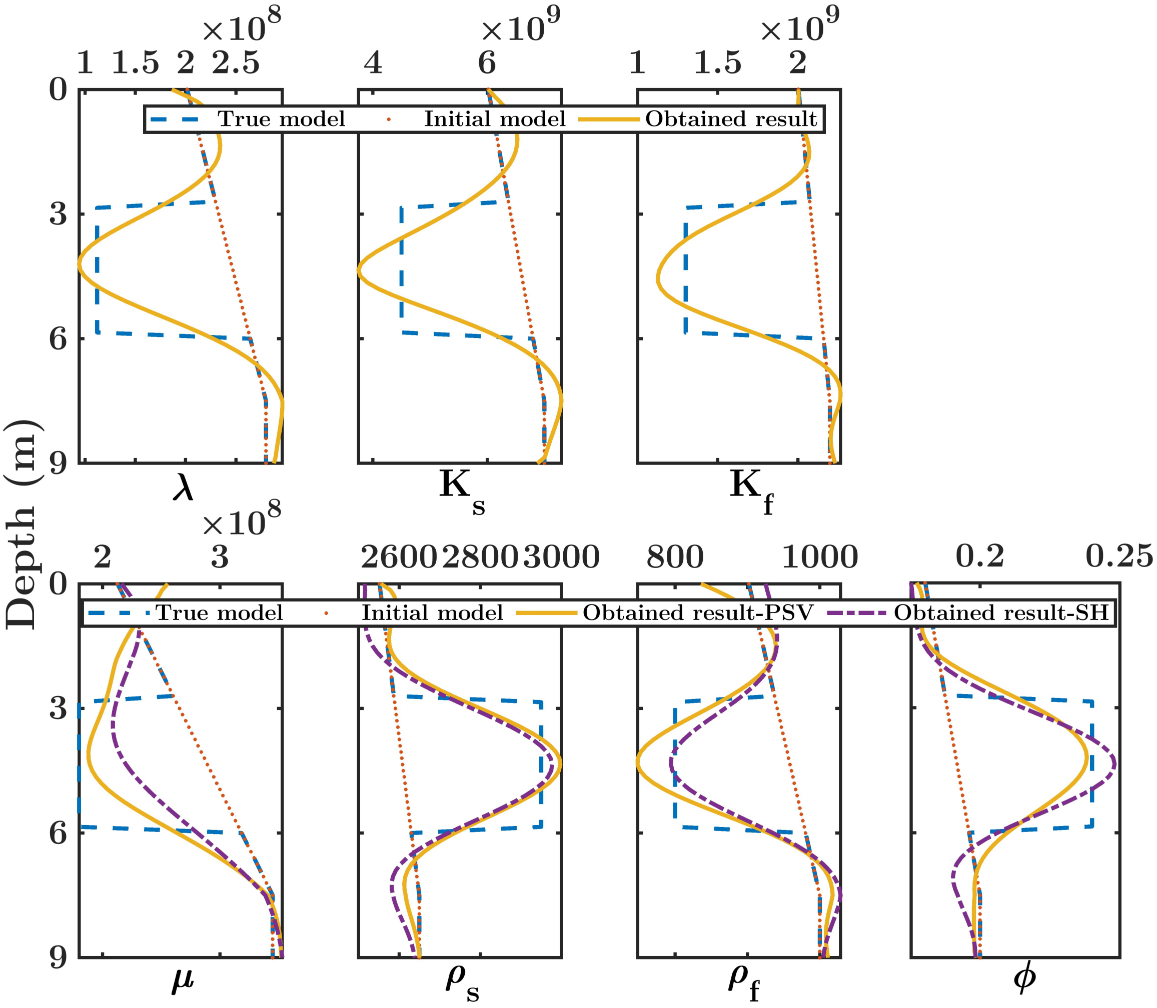

Figure 8.4.: Comparison of log profiles in the middle of the model.

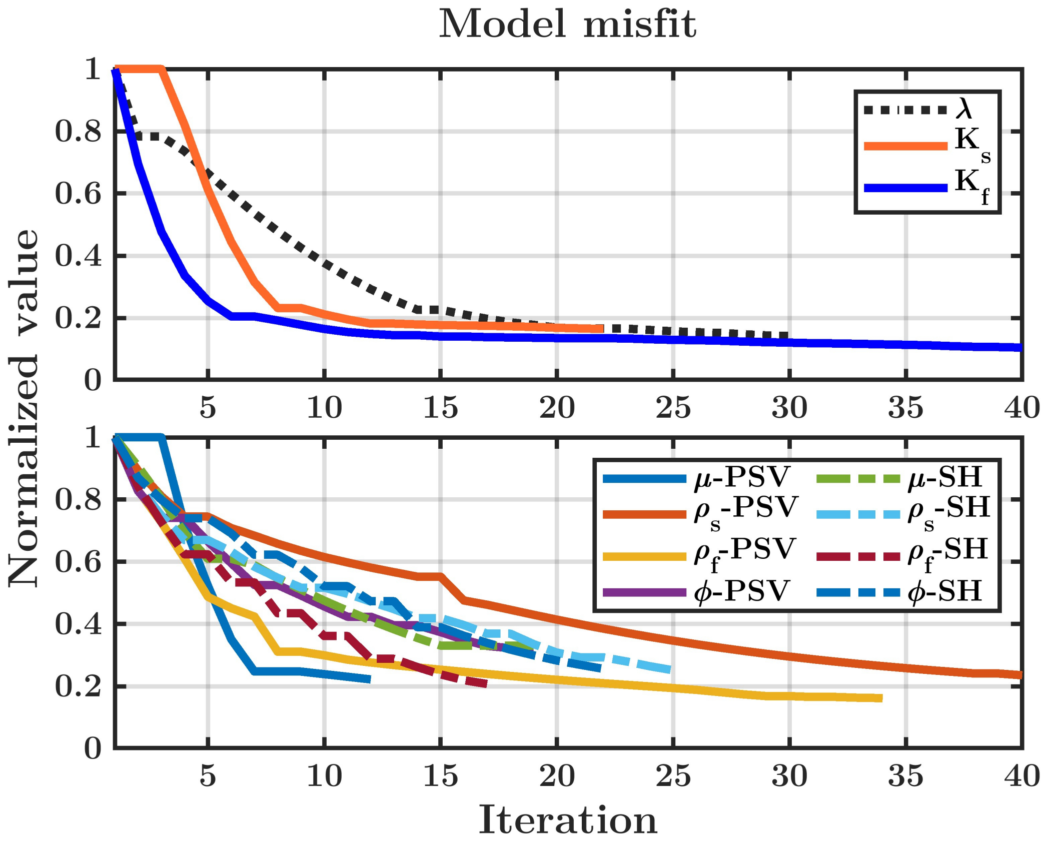

Figure 8.5.: Model misfit comparison.

8.1.4. Summary

Through iterations in multi-stages, the inversion results in Figs. 8.2 and 8.3 show that PFWI can supply an accurate estimation of the shape and location of the anomaly body, which is relay on the accuracy of wavefields simulation and gradients calculation. The inversion results are shown intuitively from log profile comparisons in Fig. 8.4. Most recovered values are close to the corresponding real models. The reconstructed $\mu, \rho_s, \rho_f, \phi$ by PSV/Rayleigh wave PFWI and SH/Love wave PFWI are also compared. To achieve convergence, Rayleigh wave PFWI usually needs more iterations compared with Love wave PFWI. For parameters such as K_s and K_f, there exist over-fitting issues. Based on the sensitivity analysis in part III, it should be because these parameters have low sensitivities to the short wavelength components in the shallow-seismic wavefields. Since the real models are known in the synthetic tests, the normalized model misfit comparisons can be exported and shown in Fig. 8.5, which indicates the inversions have achieved convergence after several iterations. For PSV/Rayleigh wave PFWI, the final model misfits show the results for different model parameters can achieve a similar degree of accuracy.

8.2. Layered model

Parameter	Symbol	Unit	Layer 1	Layer 2	Layer 3
Bulk modulus	K_s	Pa	2.5×10^9	2.8×10^9	3.3×10^9
Density	ρ_s	kg/m³	2250	2650	3100
Bulk modulus	K_d	Pa	4.5×10^8	4.8×10^8	5.6×10^8
Shear modulus	μ	Pa	2.75×10^8	3.45×10^8	3.75×10^8
Porosity	ϕ	/	0.1	0.2	0.25
Tortuosity	τ	/	2	2	2
Bulk modulus	K_f	Pa	1.5×10^9	1.8×10^9	2.2×10^9
Density	ρ_f	kg/m³	800	1000	1200
Viscosity	η	N·s/m²	-	-	-

Table 8.2.: Poroelastic parameters of the true 3-layer model.

In this section, I will implement Rayleigh&Love wave PFWI to reconstruct a $9m \times 45m$ 3-layered poroelastic subsurface and compare the inversion results. Besides surface waves, more reflected waves are involved in shallow-seismic wavefields. The real parameters of the 3 poroelastic layers are listed in Table. 8.2. The depth of each layer is 3 meters.

8.2.1. Inversion setup

The acquisition geometry is the same as in section 8.1. In FD modeling, the grid space $\Delta x = \Delta z = 0.1m$, and the time step is 0.04 ms. With a duration time of 0.12 s, the source signal is a Ricker wavelet with a central frequency of 45 Hz. The source loading, trace-killing, and source tapering methods are as the same as in section 8.1. The frequency band range is wider than in section 8.1, so the multi-stage strategy applied here is 10-20-40-60-80-100-130 Hz. The initial model of single parameters is smoothed from the corresponding true model.

8.2.2. Rayleigh wave PFWI results: λ, K_s, K_f

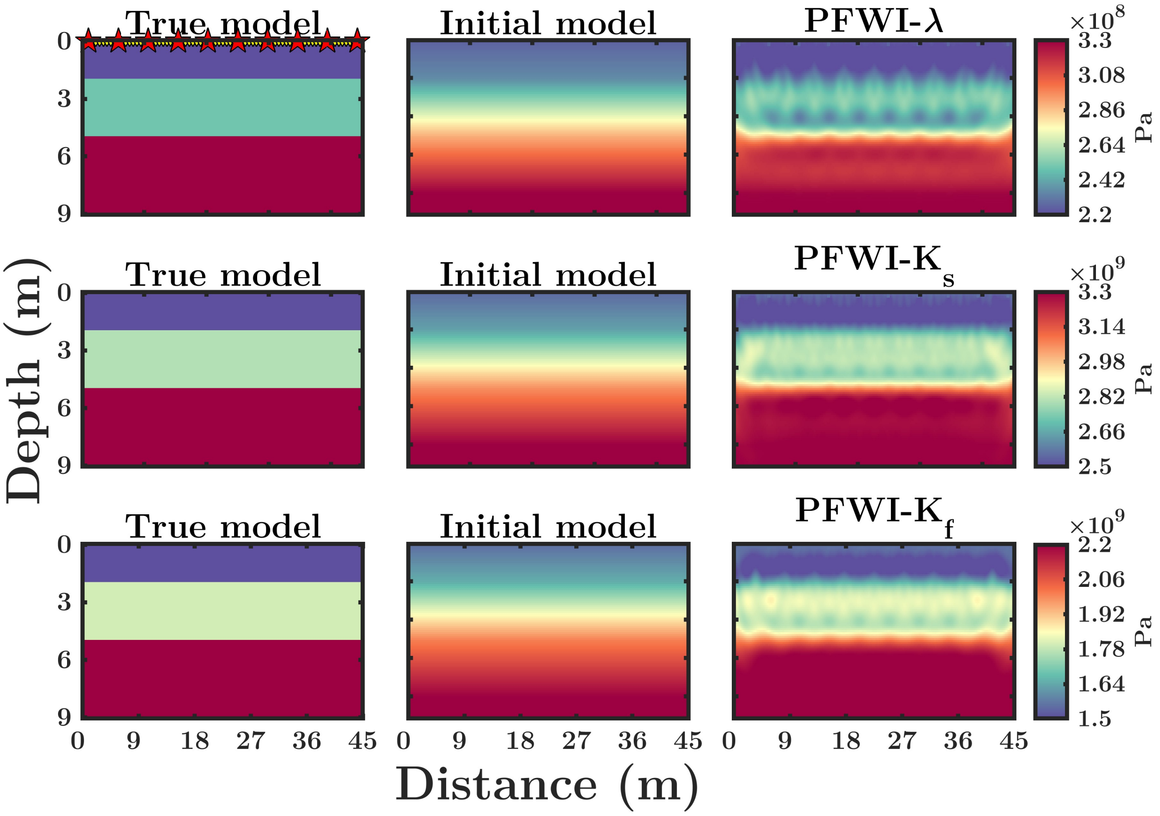

Figure 8.6.: Reconstructed λ, K_s, K_f by Rayleigh wave PFWI in a 3-layer model.

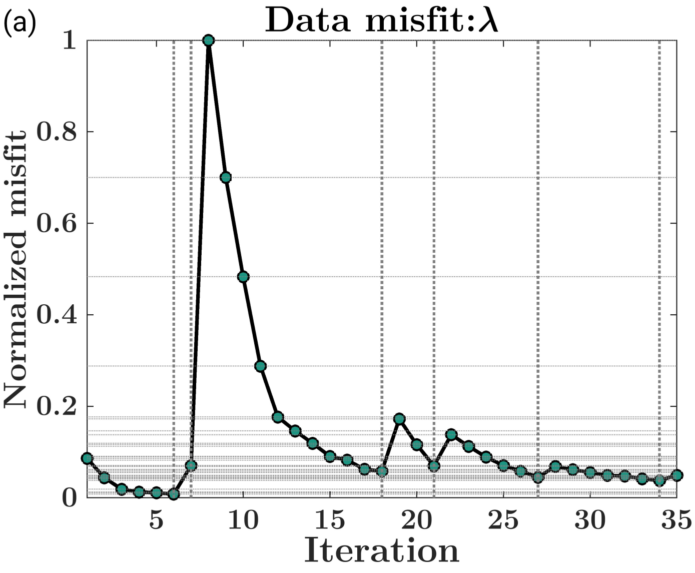

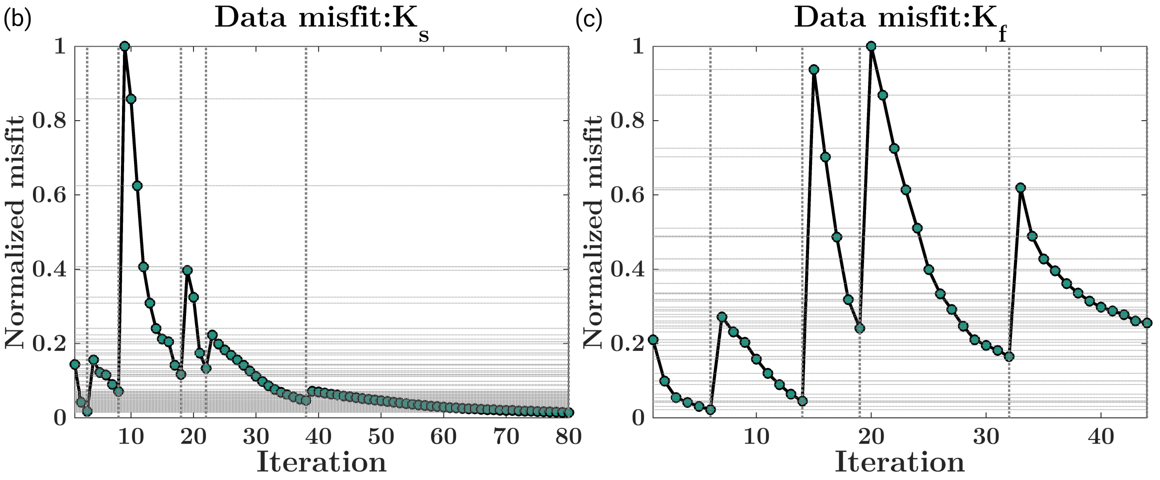

Figure 8.7.: Data misfit changed with stages for (a) λ; (b) K_s; (c) K_f.

8.2.3. Reconstruction results comparison of Rayleigh and Love wave PFWI

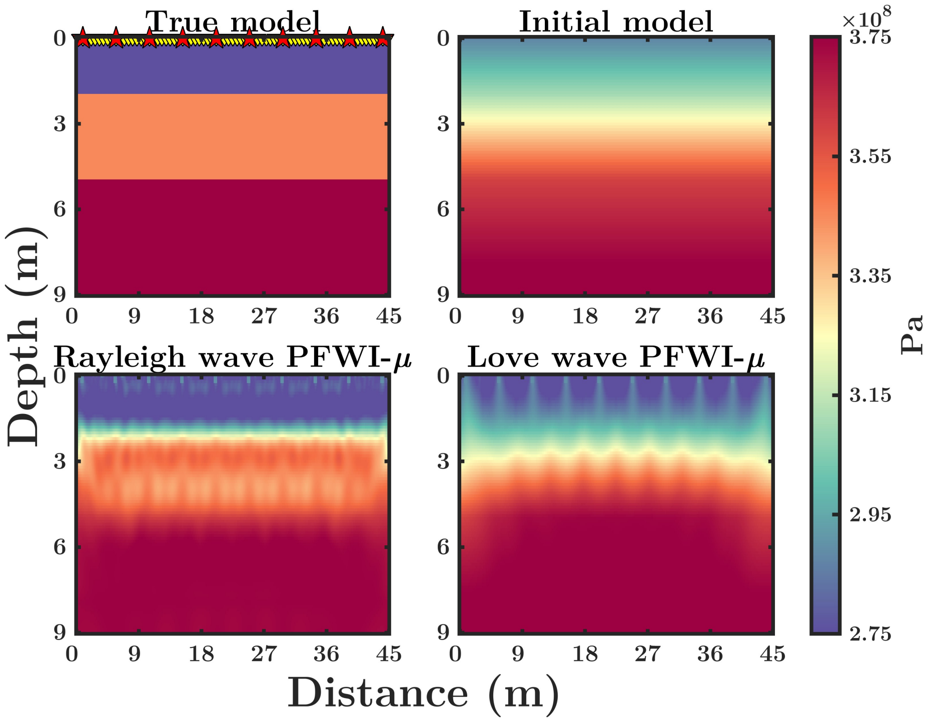

Figure 8.8.: Comparisons of reconstructed μ by Rayleigh wave and Love wave PFWI.

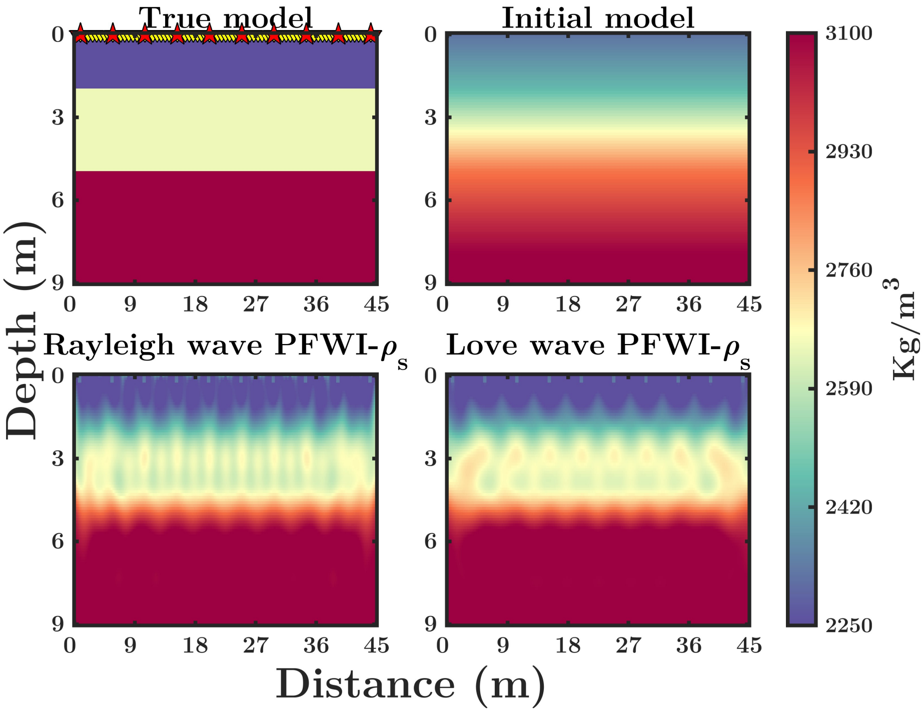

Figure 8.9.: Comparisons of reconstructed ρ_s by Rayleigh wave and Love wave PFWI.

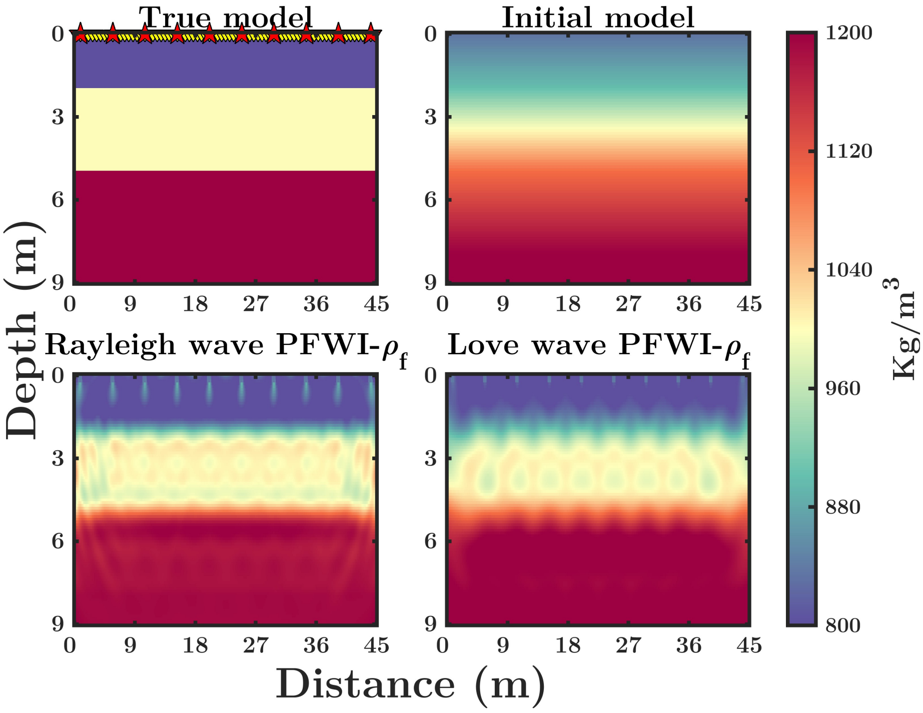

Figure 8.10.: Comparisons of reconstructed ρ_f by Rayleigh wave and Love wave PFWI.

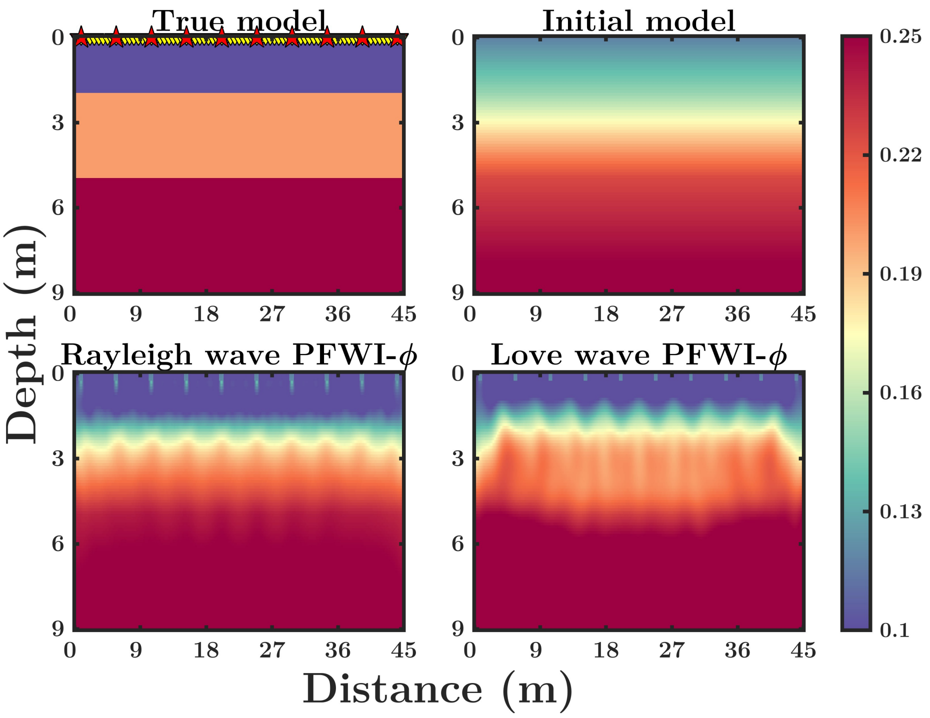

Figure 8.11.: Comparisons of reconstructed ϕ by Rayleigh wave and Love wave PFWI.

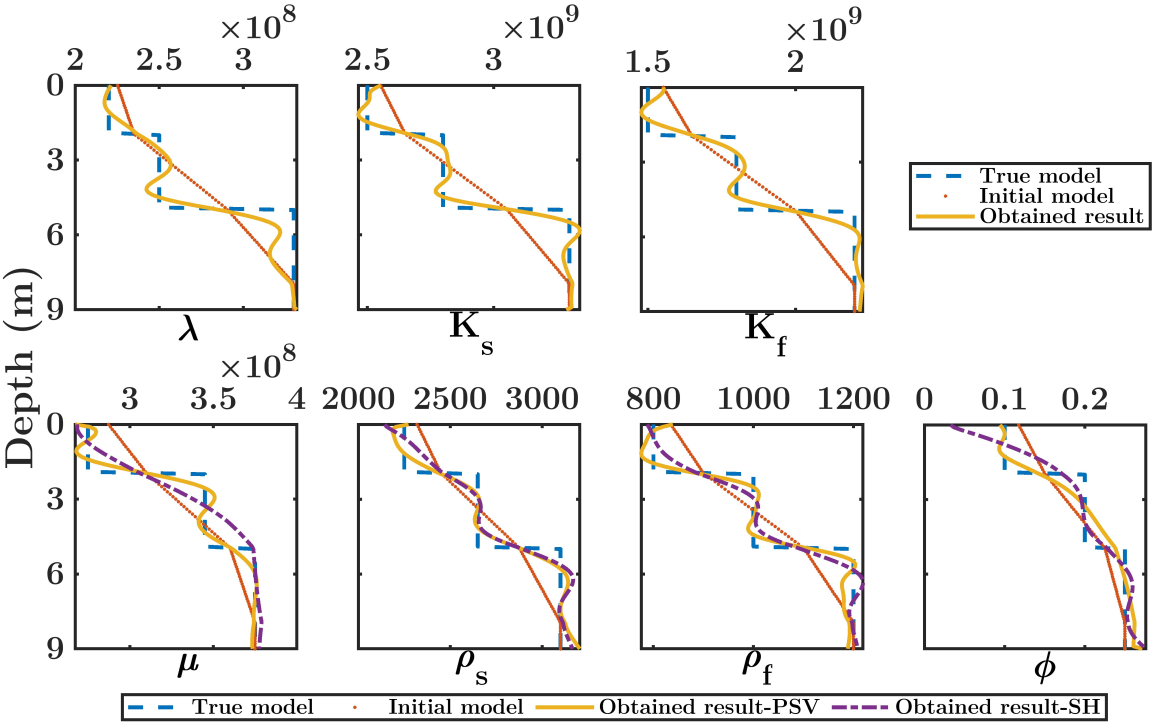

Figure 8.12.: Comparison of log profiles in the middle of the model.

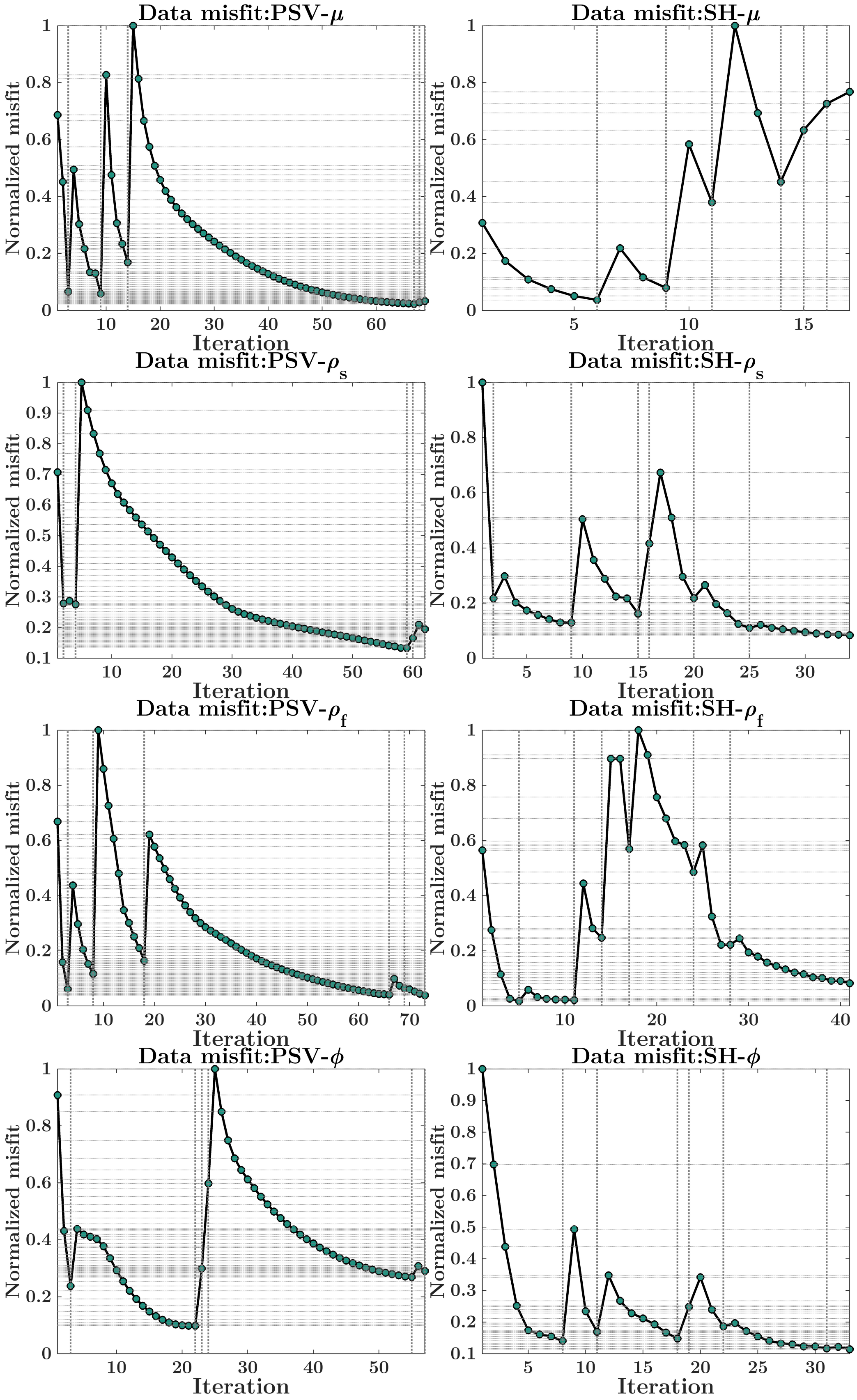

Figure 8.13.: Data misfit changed with stages for $\mu, \rho_s, \rho_f, \phi$ during PSV/Rayleigh and SH/Love wave PFWI.

8.2.4. Summary

This section contains a series of mono-parameter reconstruction tests for a 3-layer poroelastic model (Figs. 8.8-8.11). Similar to section 8.1, λ, K_s, K_f are recovered by Rayleigh wave PFWI, and $\mu, \rho_s, \rho_f, \phi$ can be recovered both by Rayleigh and Love wave PFWI. As a trapped SH mode, Love waves are much associated with the near-surface with varying vertical properties, which also travels faster than Rayleigh waves. From the log profile comparisons in Fig. 8.12, Love wave PFWI shows a better reconstruction ability in the deeper structure, especially for porosity recovery. When a multi-stage strategy is applied, the data misfit (Figs. 8.2.2 and 8.13) will show in stages format with the increasing frequency band information. In this thesis, the model and data misfit are all calculated by L2 norm errors. It is also possible that the parameters can not be updated effectively in a certain frequency band as they can not get benefits from current wave information. In this circumstance, the iterations will automatically jump to the next frequency stage. The data misfit curve is perceived as a useful tool for intuitively detecting the convergence of inversion.

9

Multi-parameter PFWI

As the real subsurface contains several physical properties, mono-parameter FWI can only detect one parameter during each implementation. In this case, the influence between different physical parameters is ignored. Instead, Multi-parameter FWI is regarded as a promising tool to image multiple subsurface geophysical parameters (e.g., P-wave velocity, S-wave velocity, anisotropic parameters, etc.) and geological parameters (e.g., Lamé constants λ, μ, density ρ, etc.) at the same time (Métivier et al. 2014). Nevertheless, it is a challenging task to update each parameter simultaneously as there are coupled effects between parameters (Operto et al. 2013). Especially, the cross-talk issues will become more serious when comes to complex mediums. Such as in the poroelastic case, the geological information from the fluid contents is also considered.

Since the sensitivities of poroelastic parameters have been discussed in part III, in this section, I will investigate the performance of multi-parameter PFWI on the recovery of different parameter groups, and clarify the cross-talk issues further. Following the idea of Köhn (2011), I build a cross-target model (CTM, Fig. 9.1) to do reconstruction tests implemented by Rayleigh and Love wave PFWI.

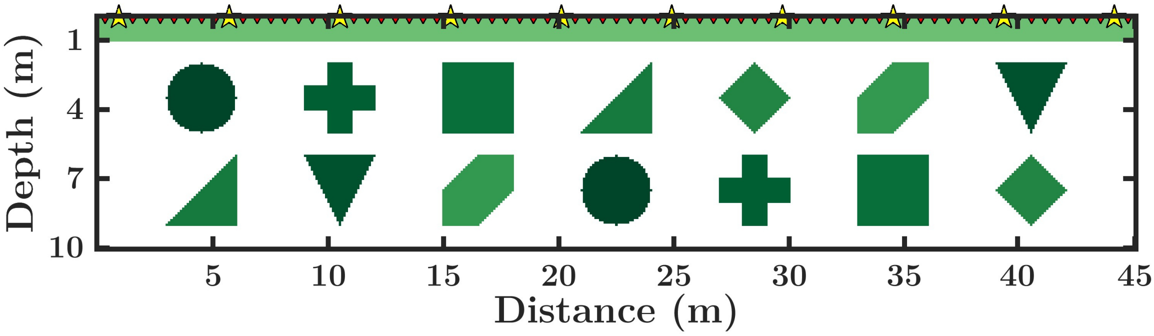

Figure 9.1.: Cross-target model for multi-parameter reconstruction tests.

The model is $10m \times 45m$ in space, which includes a two-layer poroelastic background and 7 groups of anomalies at two depths. Each group represents one type of property. The depth of the thin layer on the top is 1 meter, and the regular size of the anomaly is 3 meters in width. Table 9.1 provides the detailed model parameters.

	Parameter	Unit	Layer 1	Layer 2	Anomaly
Grain	K_s	Pa	2.5×10^9	3.3×10^9	2.8×10^9
	ρ_s	kg/m^3	2250	3100	2900
Matrix	K_d	Pa	4.03×10^8	5.8×10^8	3.1×10^8
	μ	Pa	2.75×10^8	3.75×10^8	1.8×10^8
	ϕ	/	0.25	0.1	0.2
	τ	/	2	2	2
Fluid	K_f	Pa	1.5×10^9	2.2×10^9	1.3×10^9
	ρ_f	kg/m^3	800	1200	1000
	η	N·s/m^2	-	-	-
Velocity	V_{fp}	m/s	1187.05	1133.03	-
	V_{sp}	m/s	344.65	215.47	-
	V_s	m/s	392.23	362.74	-

Table 9.1.: CTM parameters used for multi-parameter reconstruction tests in chapter 9.

The acquisition geometry and FD modeling setup are the same as in section 8.2. According to the frequency band of seismic signals, as shown in chapter C, the applied multi-stage inversion strategy is 10-20-30-45-60-80-100-130 Hz. In Rayleigh wave PFWI, the source type for forward modeling is the vertical point, and the adjoint sources are loaded to solid x, and z components. In Love wave PFWI, the forward source is a shear source, and the adjoint source is applied in the same way. The misfit function is in a classic L2 norm shown in Eq. 4.1 without normalization and regularization, which is the same as in the mono-parameter PFWI. Fig. 9.2 shows the snapshots of solid and fluid components in the forward shallow-seismic wavefields. The 2-meter thick artificial C-PML boundaries are not imaged. In the fluid-related components, shear wave information is excluded. For Love wave PFWI, there are only four types of parameters considered, and P-wave information are expelled from the wavefields.

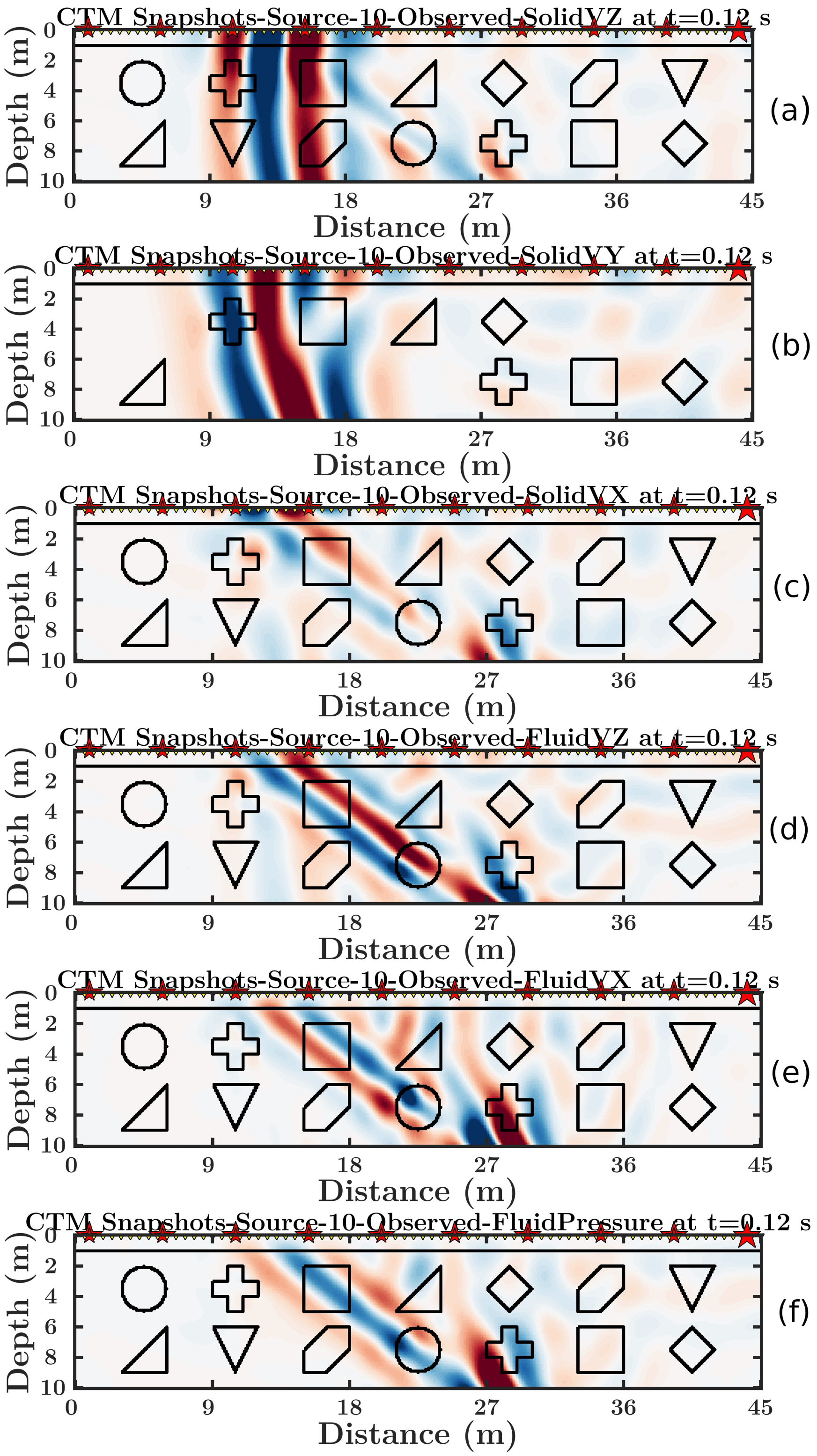

Figure 9.2.: CTM snapshots at time=0.12 s of the forward shallow-seismic wavefields from the source location X=44.1 m: (a) Solid velocity in Z direction; (b) Solid velocity in Y direction; (c) Solid velocity in X direction; (d) Fluid velocity in Z direction; (e) Fluid velocity in X direction; (f) Fluid pressure.

9.1. Rayleigh wave PFWI

In this section, the reconstruction tests are performed with five different parameter sets to explore the cross-talk issues.

9.1.1. Parameter set: $\lambda, K_s, K_f, \mu, \rho_s, \rho_f, \phi$

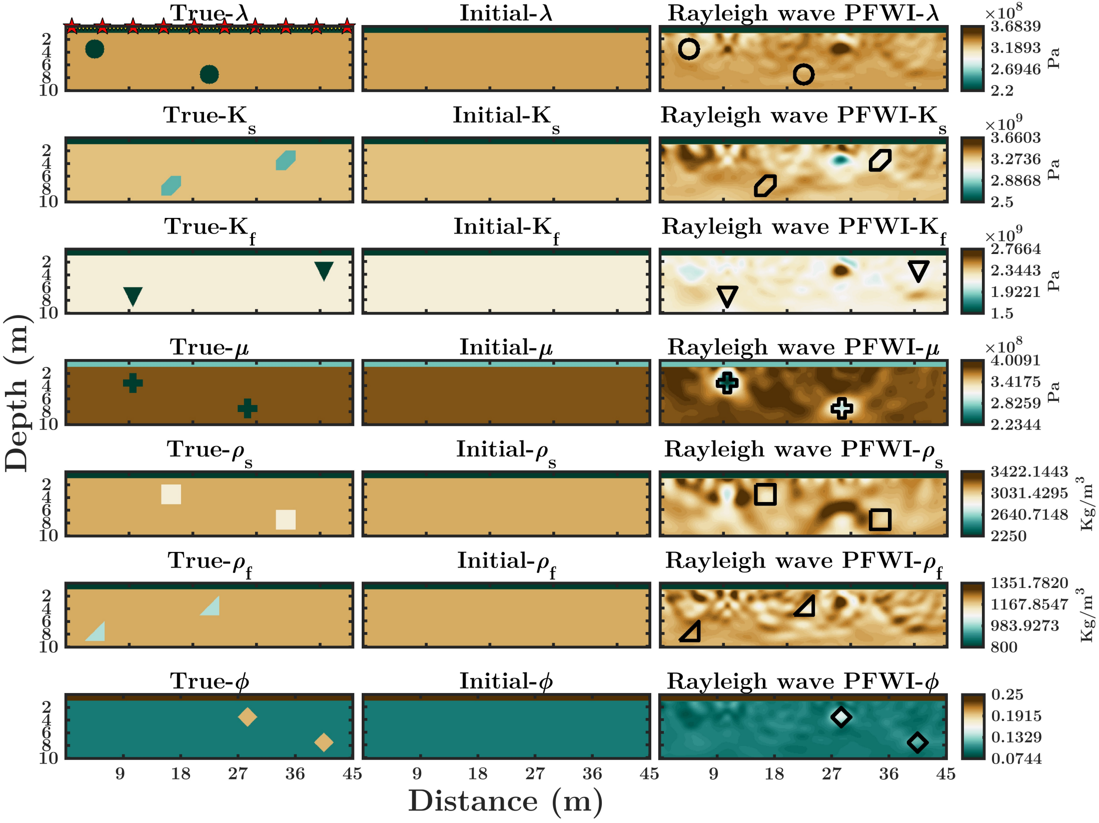

Figure 9.3.: Multi-parameter Rayleigh wave PFWI results from the parameter set (λ, K_s, K_f, μ, ρ_s, ρ_f, ϕ).

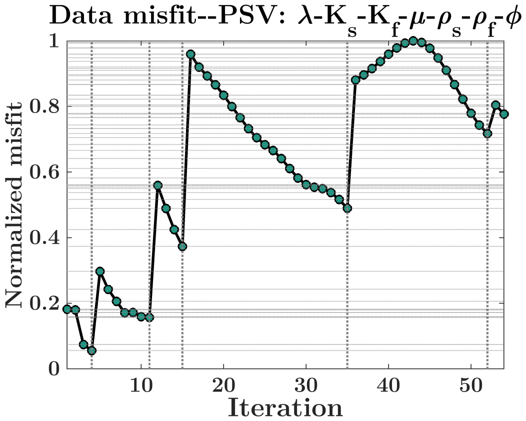

Figure 9.4.: Data misfit changed with iterations.

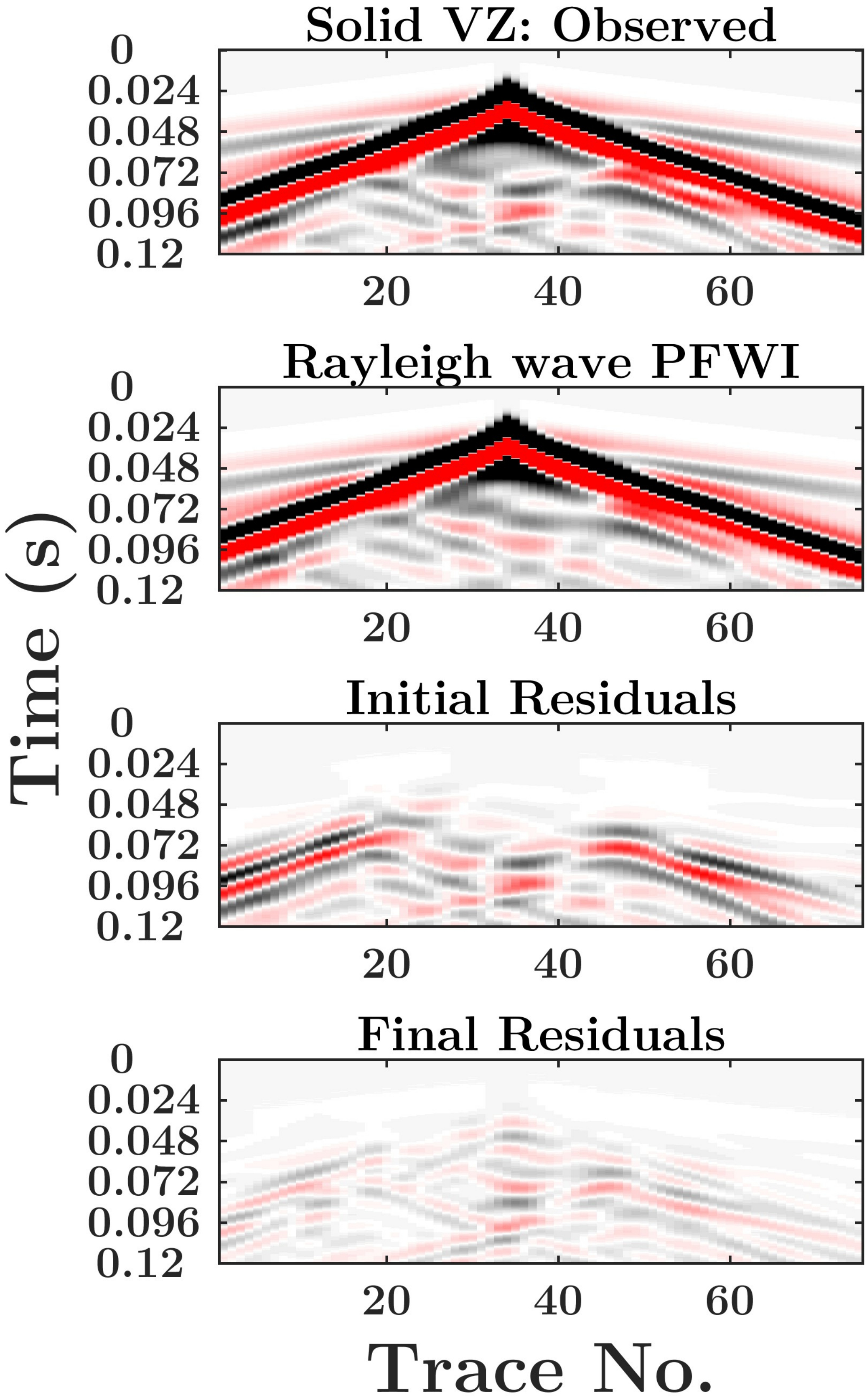

Figure 9.5.: Seismic profiles of solid Z component from the shot at x=20.1 m.

9.1.2. Parameter set: λ, K_s, K_f

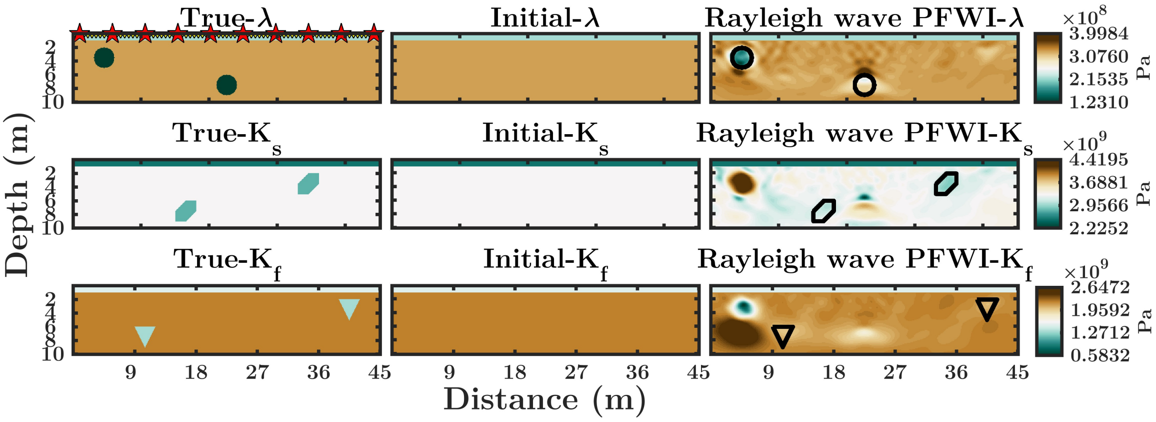

Figure 9.6.: Multi-parameter Rayleigh wave PFWI results from the parameter set (λ, K_s, K_f).

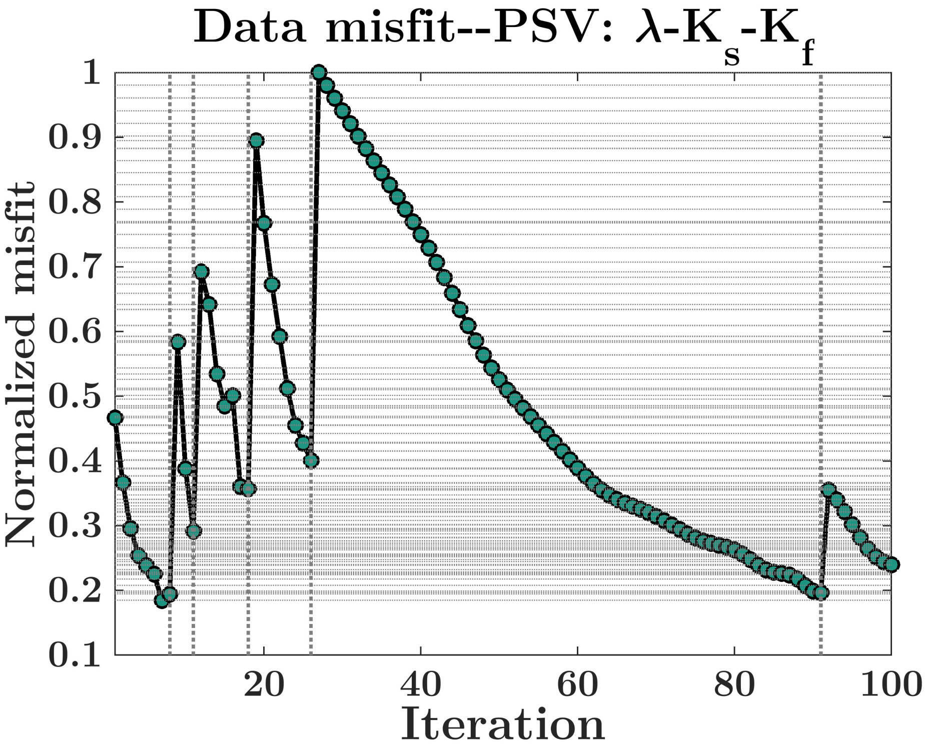

Figure 9.7.: Data misfit changed with iterations.

9.1.3. Parameter set: λ, K_s, K_f, ϕ

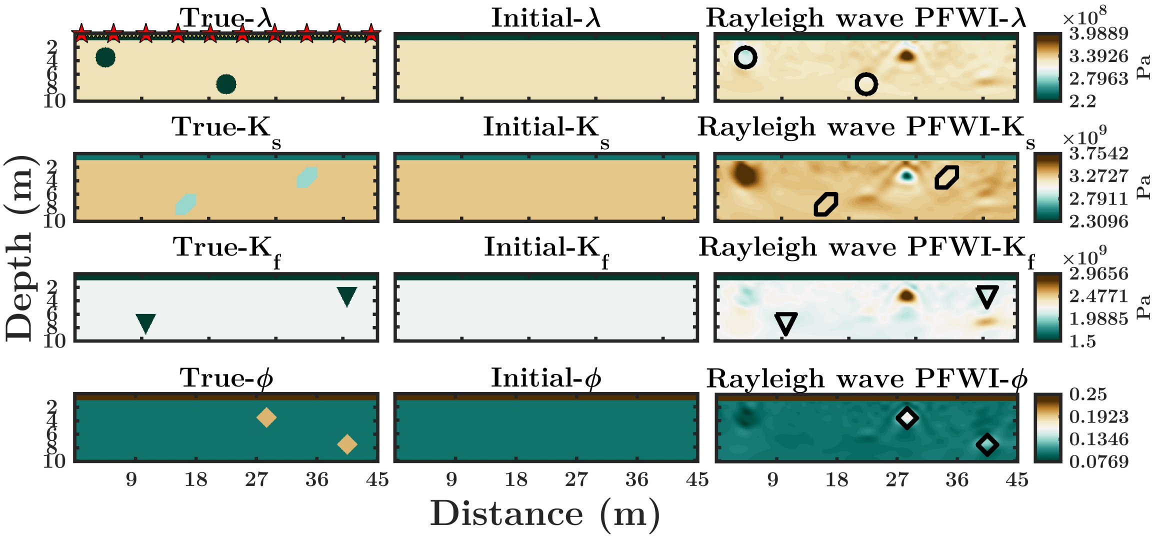

Figure 9.8.: Multi-parameter Rayleigh wave PFWI results from the parameter set (λ, K_s, K_f, ϕ).

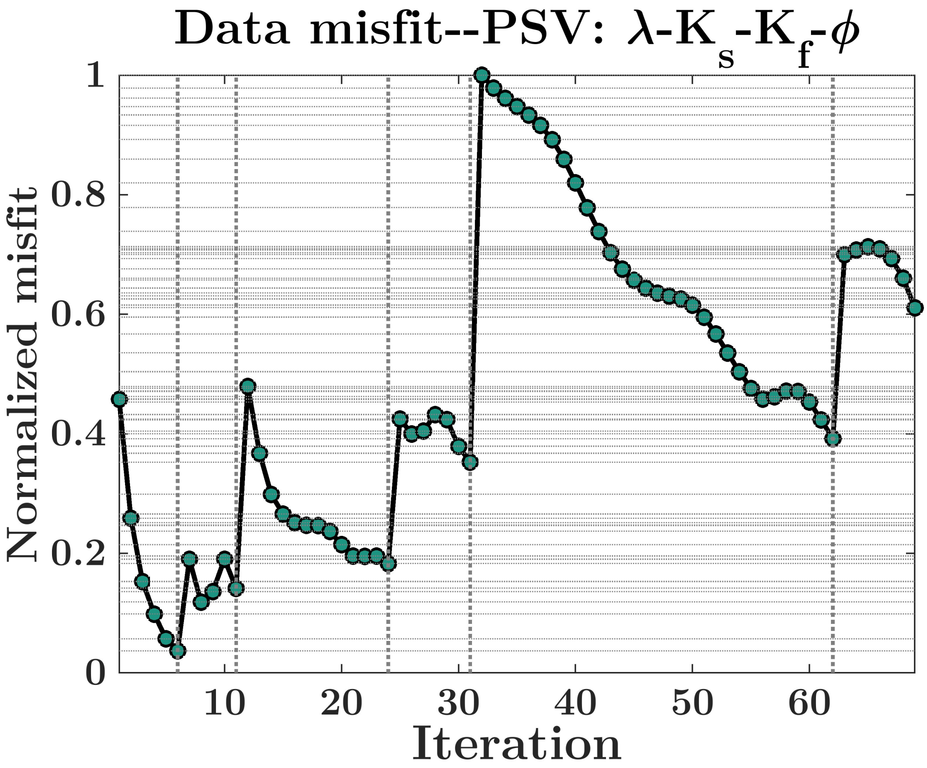

Figure 9.9.: Data misfit changed with iterations.

9.1.4. Parameter set: $\mu, \rho_s, \rho_f, \phi$

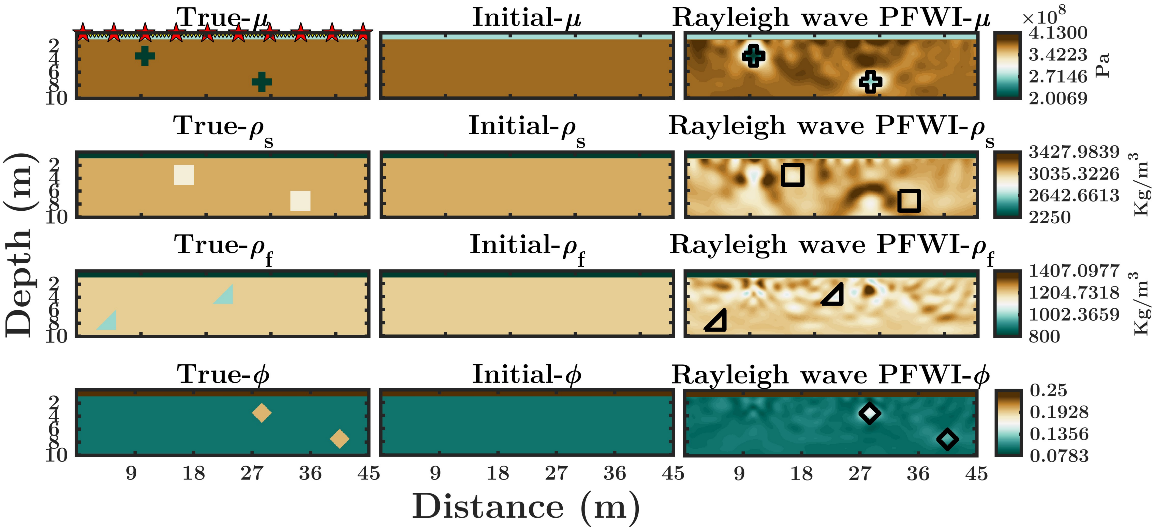

Figure 9.10.: Multi-parameter Rayleigh wave PFWI results from the parameter set (μ, ρ_s, ρ_f, ϕ).

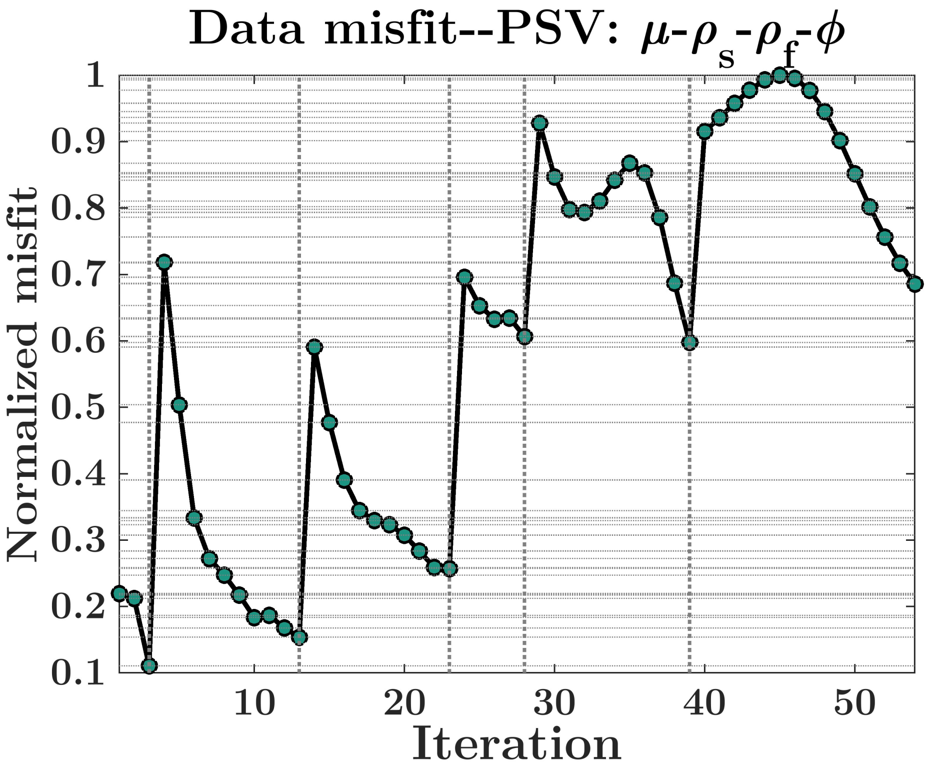

Figure 9.11.: Data misfit changed with iterations.

9.1.5. Parameter set: λ, μ, ϕ

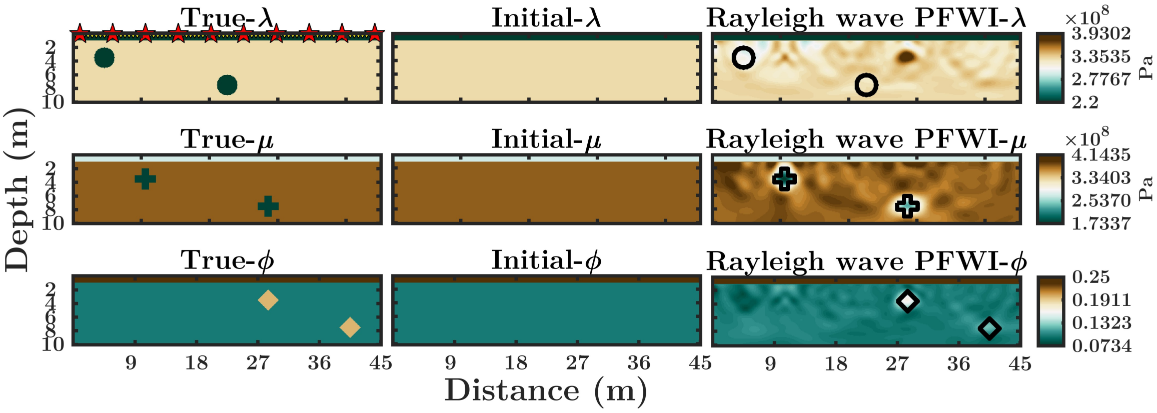

Figure 9.12.: Multi-parameter Rayleigh wave PFWI results from the parameter set (λ, μ, ϕ).

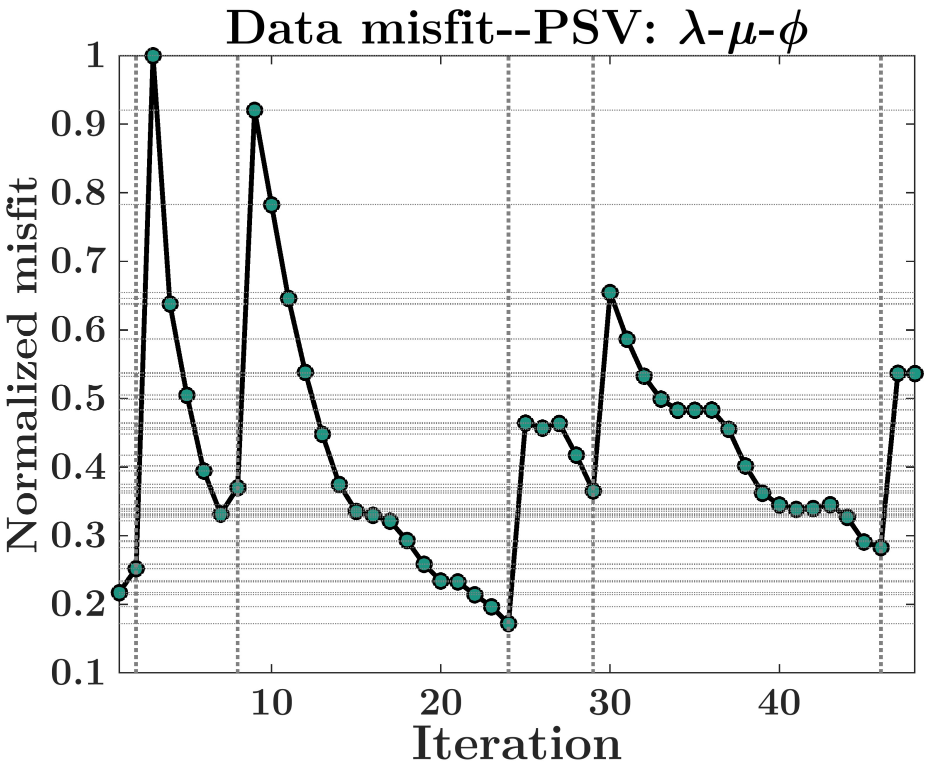

Figure 9.13.: Data misfit changed with iterations.

9.1.6. Summary

According to the methodology introduction in part II, the model space in P-SV poroelastic equations, $\mathbf{m}^{PSV}$ consist of 7 independent parameters (λ, K_s, K_f μ, ρ_s, ρ_f, ϕ) under non-dissipation condition, which means the fluid viscosity is neglected. After real updates in 6 frequency bands (Fig. 9.4), Fig. 9.3 provides the multi-parameter Rayleigh wave PFWI results from the parameter set (λ, K_s, K_f, μ, ρ_s, ρ_f, ϕ), which indicates the model parameters can hardly be reconstructed all together successfully as the strong coupled inter-parameter effects, even though, μ and ϕ are well detected from this parameter set. There are cross-talk issues from $\lambda \rightarrow K_f$, $\mu \rightarrow \rho_s$, $\phi \rightarrow \{\lambda, K_s, K_f, \rho_f\}$. Fig. 9.5 gives the seismic data comparisons. The Rayleigh wave components with stronger energies in the initial residuals are fully used, but there is still some reflection information that remains in the final residuals. In the results from parameter set (λ, K_s, K_f), λ and K_s are well recovered, especially for the near-surface anomalies. Except for the cross-talk effects between λ and K_f, there are also strong footprints from λ in the profile of K_s. When porosity ϕ is involved in the parameter set (λ, K_s, K_f, ϕ), only ϕ can be recovered as its strong effects on others (Fig. 9.8). The reconstructions from parameter set (μ, ρ_s, ρ_f, ϕ) show a similar results with parameter set (λ, K_s, K_f, μ, ρ_s, ρ_f, ϕ). At last, I conduct the inversion tests on the parameter set (λ, μ, ϕ), which are expected to have fewer coupled issues. Except for λ, μ and ϕ can be recovered, as the cross-talk effects from $\phi \rightarrow \lambda$.

9.2. Love wave PFWI

In this section, the four model parameters (μ, ρ_s, ρ_f, ϕ) in SH poroelastic equations are divided into three parameter sets to perform Love wave PFWI.

9.2.1. Parameter set: $\mu, \rho_s, \rho_f, \phi$

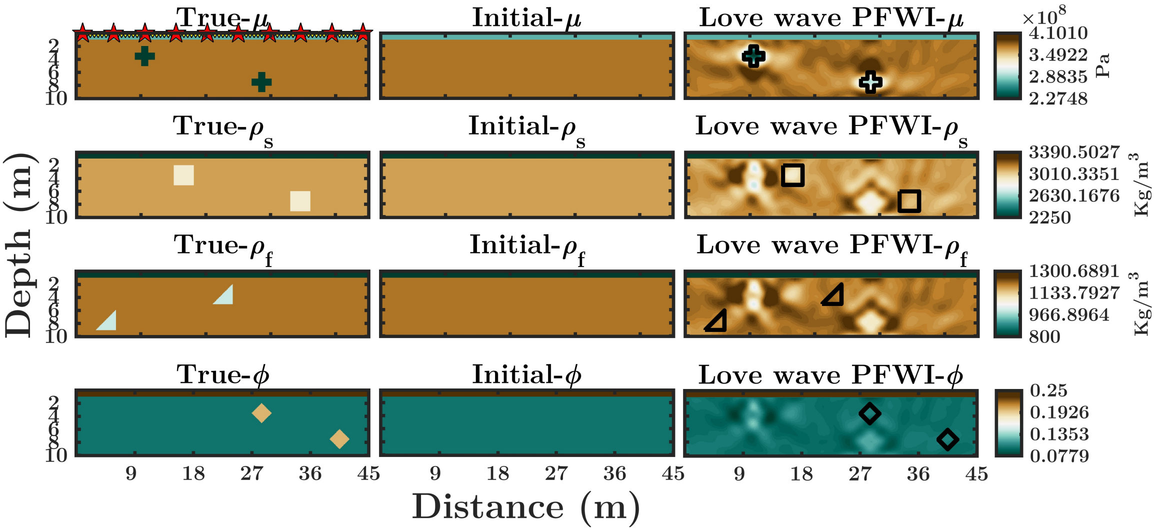

Figure 9.14.: Multi-parameter Love wave PFWI results from the parameter set (μ, ρ_s, ρ_f, ϕ).

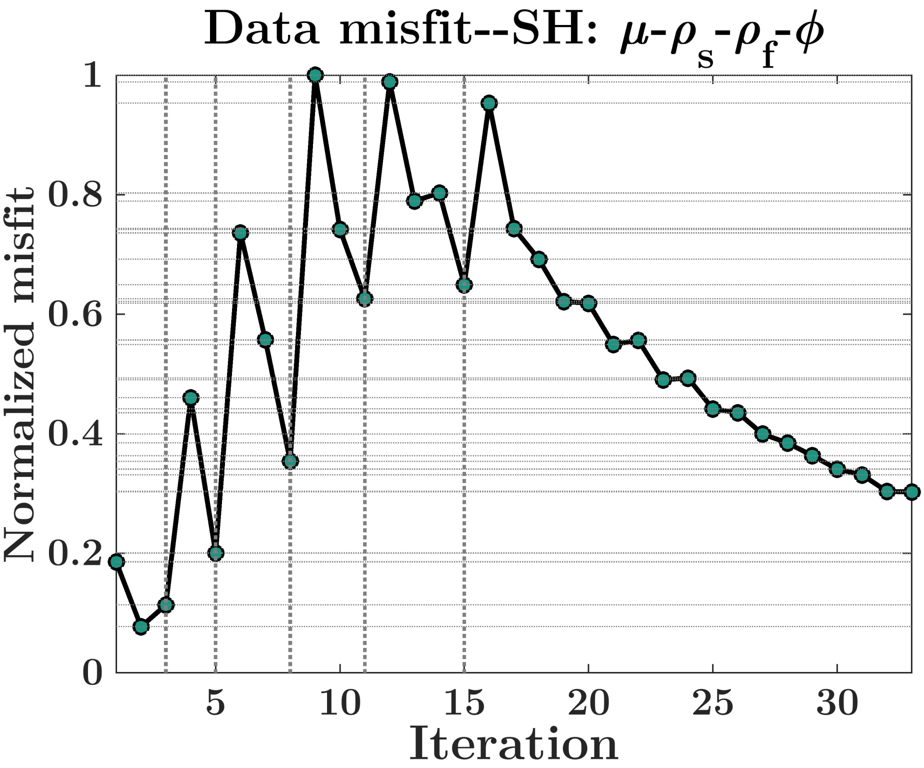

Figure 9.15.: Data misfit changed with iterations.

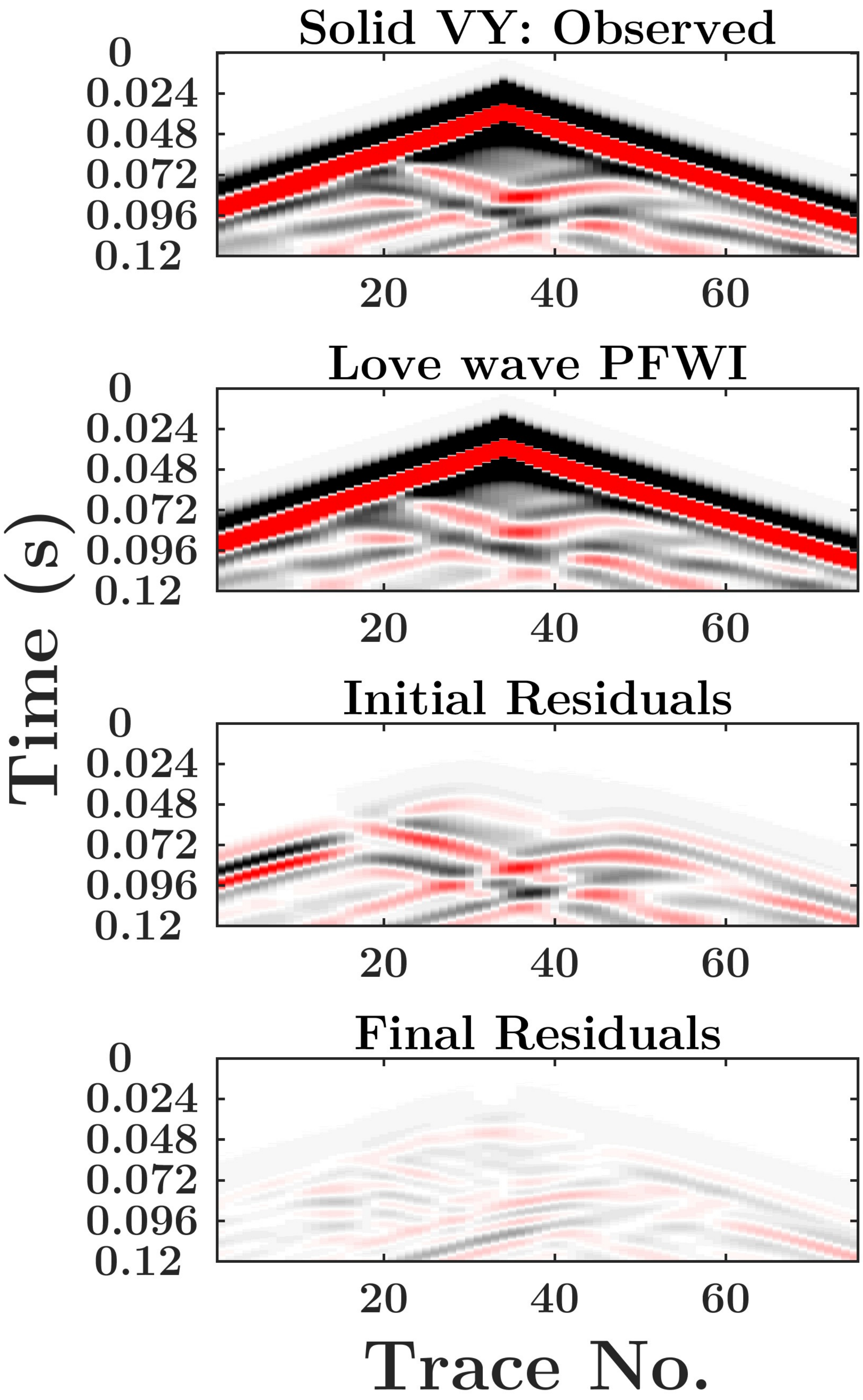

Figure 9.16.: Seismic profiles of solid Y component from the shot at x=20.1 m.

9.2.2. Parameter set: ρ_s, ρ_f, ϕ

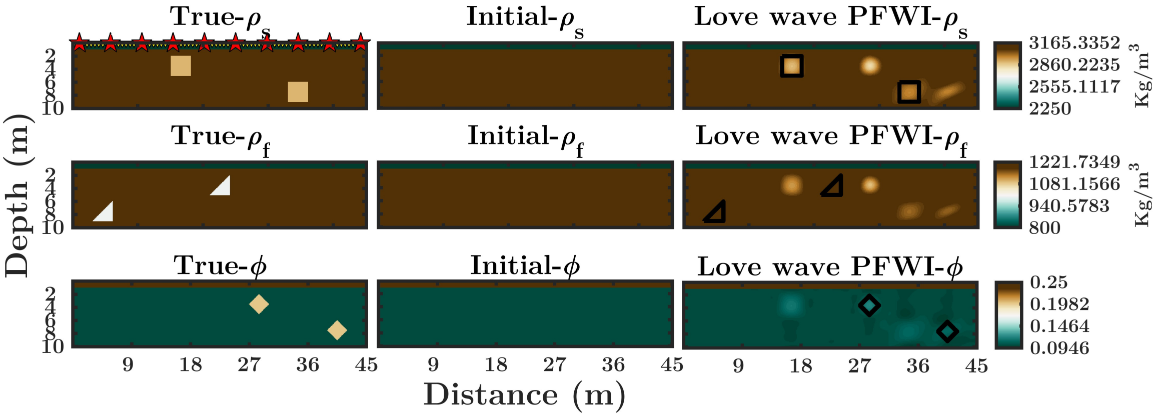

Figure 9.17.: Multi-parameter Love wave PFWI results from the parameter set (ρ_s, ρ_f, ϕ).

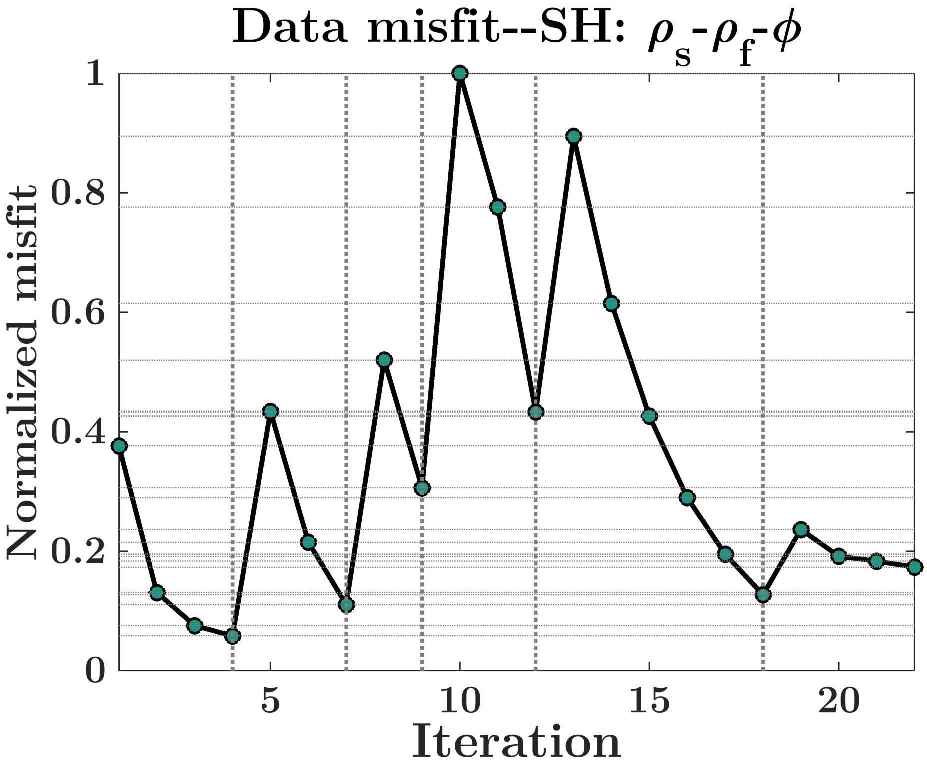

Figure 9.18.: Data misfit changed with iterations.

9.2.3. Parameter set: μ, ϕ

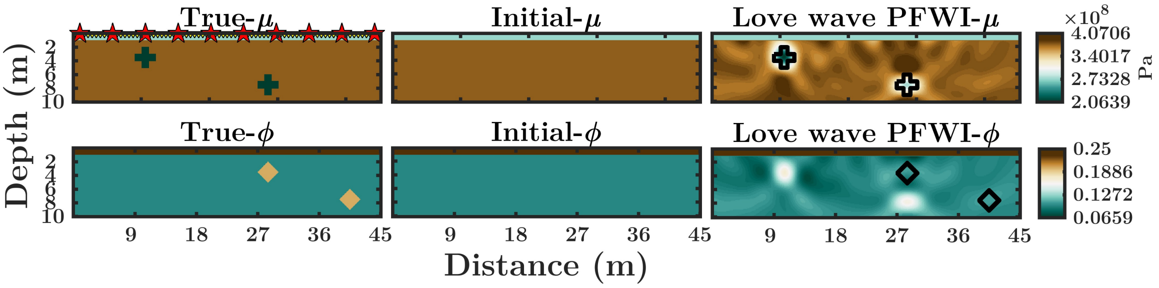

Figure 9.19.: Multi-parameter Love wave PFWI results from the parameter set (μ ϕ).

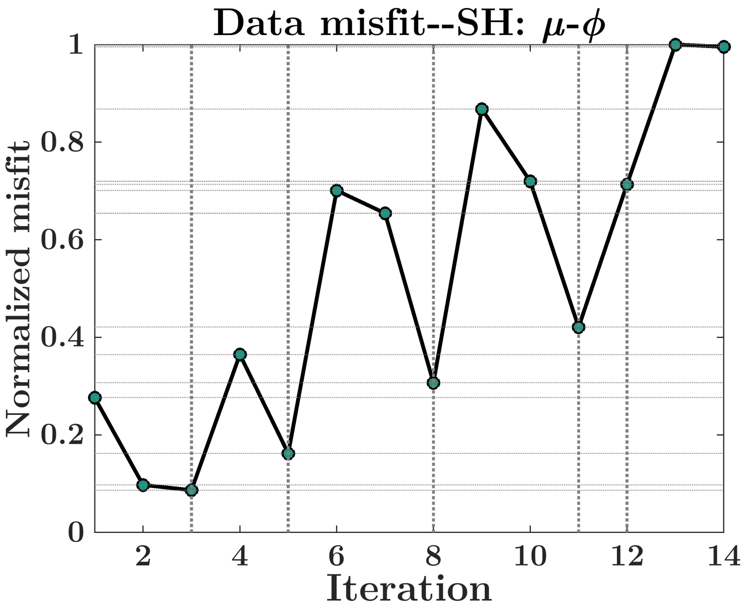

Figure 9.20.: Data misfit changed with iterations.

9.2.4. Summary

In Love wave PFWI, the compressional wave information is excluded. Fig. 9.14 gives the results from parameter set (μ, ρ_s, ρ_f, ϕ), which shows that μ and ρ_s can be recovered. Similar to the results in Rayleigh wave PFWI, there exists a cross-talk issue from $\mu \longrightarrow \rho_s$. Seismic profiles in Fig. 9.16 indicate that most of the waveform residuals are applied in the inversion, especially Love wave components. In the tests of parameter set (ρ_s, ρ_f, ϕ), ρ_s is well recovered. There are cross-talk issues from $\rho_s \longrightarrow \{\rho_f, \phi\}$ and $\phi \longrightarrow \{\rho_s, \rho_f\}$. When only reconstructing μ and ϕ together, only μ can be recovered because of the cross-talk issue from $\mu \longrightarrow \phi$ from the results in Fig. 9.19.

10

Comparison with EFWI

The real physical system in the subsurface is always complicated far beyond estimation. When more parameters are considered in the constitutive equations, PFWI shows stronger nonlinear characteristics than traditional elastic FWI (EFWI). However, the reconstruction tests introduced before have proved that it is possible to invert the poroelastic attributes by PFWI directly. In this section, I will give a toy example to compare the inversion results of SH/Love wave EFWI and PFWI, as the seismic wavefields are simple enough that only shear waves and Love waves exist.

10.1. Model setup

In the real data application of FWI methods, the direct information from the fieldwork is the waveform, which is measured by geophones at a certain location and the signal usually represents the geometric propagation velocity of seismic waves. Different math models can be used to describe the physical environment of the subsurface and find the 'best' model which can reproduce waveforms to approximate the actual collected waveform data as much as possible. So in this toy example, I will take the same initial μ and V_s models as inputs for Love wave PFWI and EFWI toward to recovery of the same real μ and V_s models. The velocity is calculated by equations in section E. Since the real observed data is always complicated, the pseudo-real data is generated under the poroelastic constraint. The acquisition geometry and poroelastic model parameters are as same as in section 8.2.

10.2. Results comparison

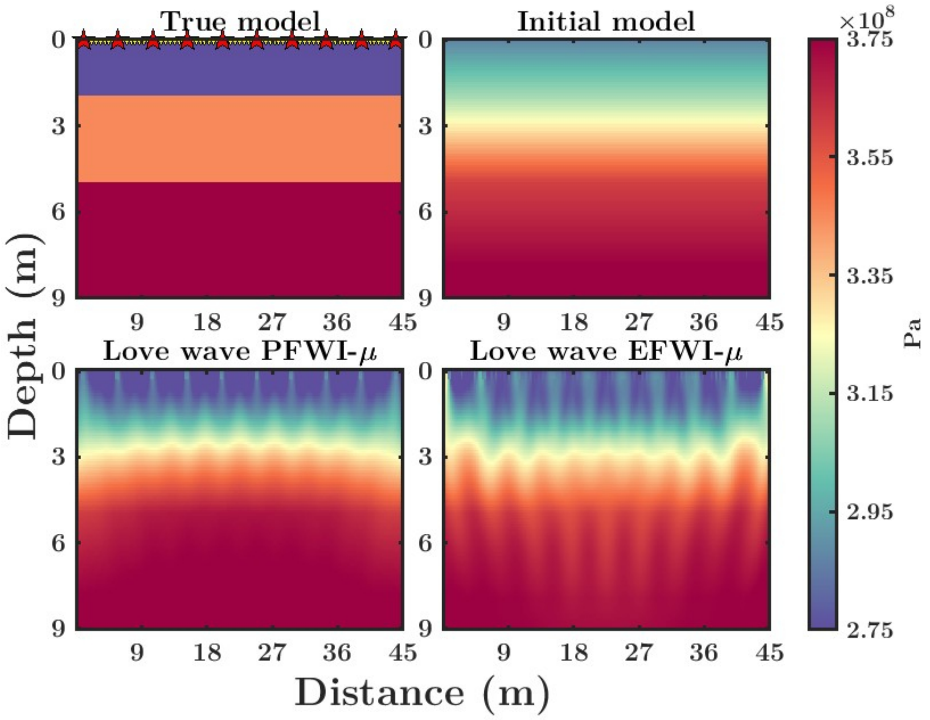

Figure 10.1.: Comparison of reconstructed μ by Love wave PFWI and EFWI.

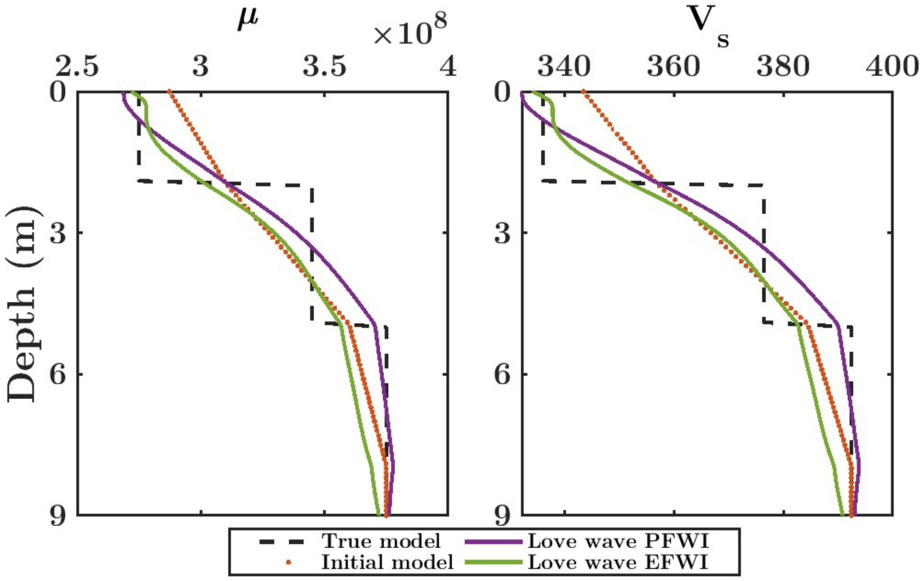

Figure 10.2.: Comparisons of log profiles in the middle of the model for reconstructed μ and V_s.

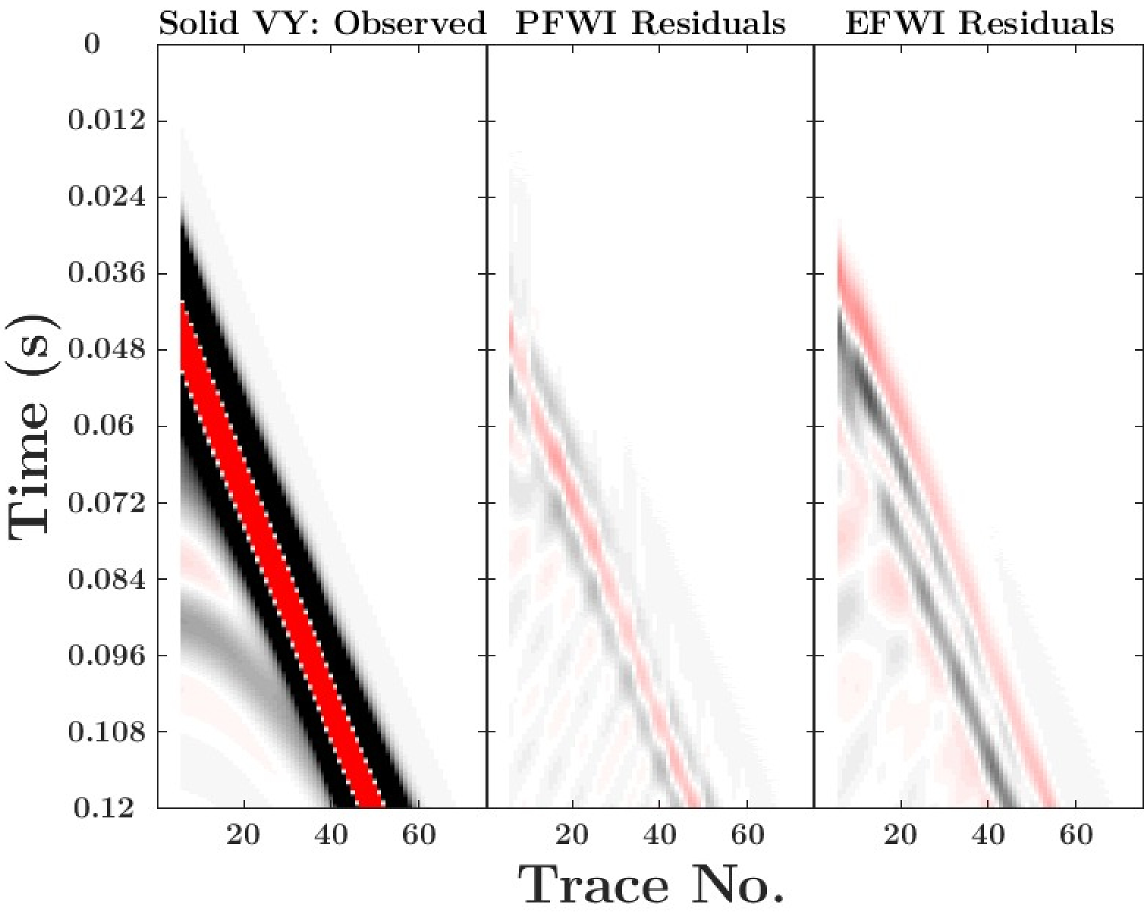

Figure 10.3.: Seismic data comparison of Love wave PFWI and EFWI.

The inverted μ are compared in Fig. 10.1, and Fig. 10.2 shows the log profiles of μ and V_s from the middle of the model. Take the first shot as an example, Fig. 10.3 shows the horizontal velocity components in the Y direction, which contain the observed data, and the data residuals from Love wave PFWI and EFWI separately. The reconstructed results of this synthetic toy example imply that even Love wave PFWI contains stronger nonlinearity, it can maximize the use of information in observed waveforms and performs better than Love wave EFWI when dealing with the complex medium. A more powerful proof will come from comparing the results of real data applications, which can be extended in the future.

Part V.

Summary

11

Conclusions

The main objective of this thesis is to establish a framework for time-domain poroelastic FWI (PFWI) for shallow-subsurface detection and explore the direct reconstruction realizability of fluid-related geological information by PFWI. Previously, the studies on FWI methods are usually developed on the basis of acoustic assumption and the stress structure considering only solid components. Here, the developed time-domain PFWI algorithm can supply a way towards the multi-parameter seismic imaging of complex subsurface containing fluid contents.

- **In the forward part**

Both the shallow-seismic P-SV and SH poroelastic wavefields are simulated numerically. Based upon Born approximation, the single-scattering P-S&SH wave equations for the fluid-saturated poroelastic media are derived. The contributions of the single poroelastic parameters (P-SV: λ, μ, ρ_s, ρ_f, K_s, K_f, ϕ; SH: μ, ρ_s, ρ_f, ϕ) on the shallow-seismic wavefields are discussed by comparing the corresponding scattered wavefields, respectively. With the help of the adjoint-state method, the explicit formulations of the sensitivity kernels for different model parameters are derived by perturbation theory and Lagrange augmented functional. The kernel galleries in P-SV&SH are used to illustrate further the sensitivities of the poroelastic parameters to different wave components. As a preliminary preparation for multi-parameter FWI, the inter-parameter issues based on the descent direction in the P-SV&SH panels of gradients are also investigated.

Similar to elastic FWI, the results indicate that shear modulus μ and grain density ρ_s are mainly responsible for generating shear waves. The fluid density ρ_f, which is extracted from the overall density ρ, pays primary attention to the slow-P wave mode. λ, which also exists in elastodynamic equations, and grain bulk modulus K_s has similar effects. In addition, fluid bulk modulus K_f and porosity ϕ mainly concern with the slow-P wave mode. ϕ affects all the wave types but prefers compressional waves. According to the real subsurface condition, it is necessary to classify the parameters with fewer correlations as a group to minimize the cross-talk issues during multi-parameter PFWI. For instance, λ and K_f are not suitable to invert together in PFWI of Rayleigh-wave data. ρ_s and ρ_f can hardly be detected together in PFWI of Love-wave data, but their correlation is minimized in P-SV equations. Since the effective velocities of the poroelastic subsurface are strongly coupled with different parameters (chapter E), it is impractical to transmit the velocity updates directly during PFWI.

- **In the inversion part**

With the help of the developed PFWI package $IforPoro$, to validate PFWI methods and figure out cross-talk issues, several numerical reconstructions with various strategies are implemented by Rayleigh and Love wave PFWI.

In the mono-parameter inversion, an anomaly model and a layered model is set up for PFWI reconstruction tests. The results illustrate that both Rayleigh and Love wave PFWI can achieve convergence and good accuracy in the estimation of poroelastic parameters. For the inversion of parameters, such as K_s, K_f, which are less sensitive to the short wavelength components in the shallow-seismic wavefields, the inversion will easily encounter over-fitting problems. The reconstruction results of the layered model show that Love wave PFWI can recover deeper subsurface properties, such as ϕ, better than Rayleigh wave PFWI.

In the multi-parameter inversion, a cross-target model is generated to examine the feasibility and reconstructability of Rayleigh&Love wave PFWI. The model parameters are divided into five parameter sets for Rayleigh wave PFWI implementations and three parameter sets for Love wave PFWI reconstructions. The Rayleigh wave PFWI results tell that μ and ϕ can be detected by from the parameter set (λ, K_s, K_f μ, ρ_s, ρ_f, ϕ). λ and K_s are well recovered from the parameter set excluded ϕ, such as (λ, K_s, K_f). There are cross-talk issues between $\lambda \longrightarrow K_f$, $\mu \longrightarrow \rho_s$, $\phi \longrightarrow \{\lambda, K_s, K_f, \rho_f\}$, which should be avoided when determining inversion parameter set. The Love wave PFWI results indicate that even though there exist cross-talk effects between μ and ρ_s, they still can be detected from the parameter set (μ, ρ_s, ρ_f, ϕ). Besides, ρ_s can be well recovered from the parameter set (ρ_s, ρ_f, ϕ). There are cross-talk issues between $\rho_s \longrightarrow \{\rho_f, \phi\}$, $\phi \longrightarrow \{\rho_s, \rho_f\}$, $\mu \longrightarrow \phi$. In the parameter set (μ, ϕ), only μ can be successfully recovered. Generally, the solid-related information (e.g., λ, K_s, μ, ρ_s) can be well recovered by multi-parameter PFWI. Apart from ϕ, parameters such as K_f and ρ_f are less estimated when combined with solid-related parameters, which is probably because the fluid adjoint source is not applied. In this thesis, the developed TD Rayleigh&Love wave PFWI methods have shown the ability to image multiple geological properties directly.

12

Outlook

In this work, a classic poroelastic full-waveform inversion (PFWI) structure has been set up and numerically validated through the developing package $IforPoro$. Both Rayleigh&Love wave PFWI can be implemented successfully. Even though, this thesis tries to break the ice in multi-parameter PFWI and direct reconstruction of fluid information. There are still several open topics that need to be further investigated.

- **Joint inversion of Rayleigh&Love wave PFWI**

  Since the sensitivity of poroelastic parameters to different wave types has been studied. To detect some determined areas more accurately, the joint inversion of Rayleigh&Love wave PFWI might be worth trying to reduce the cross-talk issues between parameters and increase the reconstruction accuracy.

- **Applying FWI techniques**

  FWI is a rising topic in the last decades. For now, there are numerous techniques concerning every step (e.g., Modification of misfit functional; Application of different optimization methods; With the help of Machine learning technique;) have been developed to improve the inversion results.

- **Field data application & 3D PFWI setup**

  In this thesis, there are only synthetic reconstruction examples. To further detect the reconstruction ability of PFWI on the shallow subsurface, some field data application tests are necessary for the future. In the meantime, it will be helpful to visualize and explore the unknown subsurface in more detail accurately, if the 2D inversion structure can be extended to a 3D case.

- **Modification of the methodology on the porous subsurface**

In this work, the forward system is based on the fluid-saturated poroelastic equations coming from Biot's theories (Biot 1956a,b, 1962; Biot and Willis 1957). As we know, theoretics always has their own limitations. Regarding the poroelastic theories, there are also studies on the patchy consolidation and dual-porosity environments (Elsworth and Bai 1992; Gerke and Genuchten 1993; White 1975). Nevertheless, there is still a big gap between the forward and inverse problems in the application of these theories, which might be an interesting topic worth trying.

Bibliography

Aki, K. and P.G. Richards (1980). *Quantitative Seismology: Theory and Methods.* Geology Series v. 1-2. W. H. Freeman. ISBN: 9780716710585. URL: `https://books.google.de/books?id=iYEwQQAACAAJ`.

Ben-Menahem, Ari and David G Harkrider (1964). "Radiation patterns of seismic surface waves from buried dipolar point sources in a flat stratified earth". In: *Journal of Geophysical Research* 69.12, pp. 2605–2620.

Berenger, Jean-Pierre (1994). "A perfectly matched layer for the absorption of electromagnetic waves". In: *Journal of Computational Physics* 114.2, pp. 185–200. ISSN: 0021-9991. DOI: `https://doi.org/10.1006/jcph.1994.1159`. URL: `https://www.sciencedirect.com/science/article/pii/S0021999184711594`.

Berg, P. et al. (1994). "Analytic reference solutions". In: *Modeling the Earth for oil exploration, Final report of the CEC's GEOSCIENCE I Program 1990-1993.* Ed. by K. Helbig. Pergamon Press, Oxford, United Kingdom, pp. 421–427.

Berryman, James G. (1999). "Origin of Gassmann's equations". In: *GEOPHYSICS* 64.5, pp. 1627–1629. DOI: `10.1190/1.1444667`. eprint: `https://doi.org/10.1190/1.1444667`. URL: `https://doi.org/10.1190/1.1444667`.

Biot, M. A. (1956a). "Theory of Propagation of Elastic Waves in a Fluid-Saturated Porous Solid. I. Low-Frequency Range". In: *The Journal of the Acoustical Society of America* 28.2, pp. 168–178. DOI: `10.1121/1.1908239`. eprint: `https://doi.org/10.1121/1.1908239`. URL: `https://doi.org/10.1121/1.1908239`.

– (1956b). "Theory of Propagation of Elastic Waves in a Fluid-Saturated Porous Solid. II. Higher Frequency Range". In: *The Journal of the Acoustical Society of America* 28.2, pp. 179–191. DOI: `10.1121/1.1908241`. eprint: `https://doi.org/10.1121/1.1908241`. URL: `https://doi.org/10.1121/1.1908241`.

– (1962). "Mechanics of Deformation and Acoustic Propagation in Porous Media". In: *Journal of Applied Physics* 33.4, pp. 1482–1498. DOI: `10.1063/1.1728759`. eprint: `https://doi.org/10.1063/1.1728759`. URL: `https://doi.org/10.1063/1.1728759`.

Biot, M. A. and D. G. Willis (1957). "THE ELASTIC COEFFICIENTS OF THE THEORY OF CONSOLIDATION". In: *Journal of Applied Mechanics* 24, pp. 594–601.

Bohlen, Thomas (2002). "Parallel 3-D viscoelastic finite difference seismic modelling". In: *Computers & Geosciences* 28.8, pp. 887–899. ISSN: 0098-3004. DOI: `https://doi.org/10.1016/S0098-3004(02)00006-7`. URL: `https://www.sciencedirect.com/science/article/pii/S0098300402000067`.

Bohlen, Thomas and Erik H. Saenger (2006). "Accuracy of heterogeneous staggered-grid finite-difference modeling of Rayleigh waves". In: *GEOPHYSICS* 71.4, T109–

T115. DOI: `10.1190/1.2213051`. eprint: `https://doi.org/10.1190/1.2213051`. URL: `https://doi.org/10.1190/1.2213051`.

Boonyasiriwat, Chaiwoot et al. (2009). "An efficient multiscale method for time-domain waveform tomography". In: *GEOPHYSICS* 74.6, WCC59–WCC68. DOI: `10.1190/1.3151869`. eprint: `https://doi.org/10.1190/1.3151869`. URL: `https://doi.org/10.1190/1.3151869`.

Bunks, Carey et al. (1995). "Multiscale seismic waveform inversion". In: *GEOPHYSICS* 60.5, pp. 1457–1473. DOI: `10.1190/1.1443880`. eprint: `https://doi.org/10.1190/1.1443880`. URL: `https://doi.org/10.1190/1.1443880`.

Butler, D.K. (2005). *Near-surface Geophysics*. Investigations in geophysics Near-surface geophysics. Society of Exploration Geophysicists. ISBN: 9781560801719. URL: `https://books.google.de/books?id=0q-ywgEACAAJ`.

Caprili, M. (1983). "Solution of a free boundary problem by finite elements: Numerical considerations and results". In: *International Journal for Numerical Methods in Engineering* 19.3, pp. 355–371. DOI: `https://doi.org/10.1002/nme.1620190305`. eprint: `https://onlinelibrary.wiley.com/doi/pdf/10.1002/nme.1620190305`. URL: `https://onlinelibrary.wiley.com/doi/abs/10.1002/nme.1620190305`.

"Chapter 7 - Biot Theory for Porous Media" (2015). In: *Wave Fields in Real Media (Third Edition)*. Ed. by José M. Carcione. Third Edition. Oxford: Elsevier, pp. 299–420. ISBN: 978-0-08-099999-9. DOI: `https://doi.org/10.1016/B978-0-08-099999-9.00007-8`. URL: `https://www.sciencedirect.com/science/article/pii/B9780080999999000078`.

Carcione, José M., Gérard C. Herman, and A. P. E. ten Kroode (2002). "Seismic modeling". In: *GEOPHYSICS* 67.4, pp. 1304–1325. DOI: `10.1190/1.1500393`. eprint: `https://doi.org/10.1190/1.1500393`. URL: `https://doi.org/10.1190/1.1500393`.

Carcione, José M., Christina Morency, and Juan E. Santos (2010). "Computational poroelasticity — A review". In: *GEOPHYSICS* 75.5, 75A229–75A243. DOI: `10.1190/1.3474602`. eprint: `https://doi.org/10.1190/1.3474602`. URL: `https://doi.org/10.1190/1.3474602`.

Cerjan, Charles et al. (1985). "A nonreflecting boundary condition for discrete acoustic and elastic wave equations". In: *GEOPHYSICS* 50.4, pp. 705–708. DOI: `10.1190/1.1441945`. eprint: `https://doi.org/10.1190/1.1441945`. URL: `https://doi.org/10.1190/1.1441945`.

Chavent, G. (1974). "Identification of functional parameters in partial differential equations". Undetermined. In: *Joint Automatic Control Conference* 12, pp. 155–156. DOI: `10.1109/JACC.1974.4170030`.

Collino, Francis and Chrysoula Tsogka (2001). "Application of the perfectly matched absorbing layer model to the linear elastodynamic problem in anisotropic heterogeneous media". In: *GEOPHYSICS* 66.1, pp. 294–307. DOI: `10.1190/1.1444908`.

eprint: https://doi.org/10.1190/1.1444908. URL: https://doi.org/10.1190/1.1444908.

Corapcioglu, M. Yavuz (1991). “Wave Propagation in Porous Media—A Review”. In: *Transport Processes in Porous Media.* Ed. by Jacob Bear and M. Yavuz Corapcioglu. Dordrecht: Springer Netherlands, pp. 373–469. ISBN: 978-94-011-3628-0. DOI: 10.1007/978-94-011-3628-0_8. URL: https://doi.org/10.1007/978-94-011-3628-0_8.

Dai, N., A. Vafidis, and E. R. Kanasewich (1995). “Wave propagation in heterogeneous, porous media: A velocity-stress, finite-difference method”. In: *Geophysics* 60.2, pp. 327–340. DOI: 10.1190/1.1443769. eprint: https://doi.org/10.1190/1.1443769. URL: https://doi.org/10.1190/1.1443769.

De Barros, L. (2012). *Using a Poroelastic Theory to Reconstruct Subsurface Properties: Numerical Investigation.* IntechOpen. URL: https://books.google.de/books?id=TjygzQEACAAJ.

Deresiewicz, H. (Oct. 1960). “The effect of boundaries on wave propagation in a liquid-filled porous solid: I. Reflection of plane waves at a free plane boundary (non-dissipative case)”. In: *Bulletin of the Seismological Society of America* 50.4, pp. 599–607. ISSN: 0037-1106. eprint: https://pubs.geoscienceworld.org/bssa/article-pdf/50/4/599/2692739/BSSA0500040599.pdf.

Dupuy, Bastien et al. (2016). “Estimation of rock physics properties from seismic attributes — Part 2: Applications”. In: *Geophysics* 81.4, pp. M55–M69. DOI: 10.1190/geo2015-0492.1. eprint: https://doi.org/10.1190/geo2015-0492.1. URL: https://doi.org/10.1190/geo2015-0492.1.

Elsworth, Derek and Mao Bai (1992). “Flow Deformation Response of Dual-Porosity Media”. In: *Journal of Geotechnical Engineering* 118.1, pp. 107–124. DOI: 10.1061/(ASCE)0733-9410(1992)118:1(107). eprint: https://ascelibrary.org/doi/pdf/10.1061/\%28ASCE\%290733-9410\%281992\%29118\%3A1\%28107\%29. URL: https://ascelibrary.org/doi/abs/10.1061/%5C%28ASCE%5C%290733-9410%5C%281992%5C%29118%5C%3A1%5C%28107%5C%29.

Gassmann, F. (1951). *Über die Elastizität poröser Medien.* Mitteilungen aus dem Institut für Geophysik an der Eidgenössischen Technischen Hochschule Zürich. Inst. für Geophysik an der ETH. URL: https://books.google.de/books?id=DseMZwEACAAJ.

Gauthier, Odile, Jean Virieux, and Albert Tarantola (1986). “Two-dimensional nonlinear inversion of seismic waveforms: Numerical results”. In: *GEOPHYSICS* 51.7, pp. 1387–1403. DOI: 10.1190/1.1442188. eprint: https://doi.org/10.1190/1.1442188. URL: https://doi.org/10.1190/1.1442188.

Geophysical Institute (2015). *SOFI2D-seismic modeling with finite differences 2D - elastic and viscoelastic version.* https://git.scc.kit.edu/GPIAG-Software/SOFI2D_sh/tree/Release. Karlsruhe Institute of Technology (KIT).

Gerke, H. H. and M. T. van Genuchten (1993). "A dual-porosity model for simulating the preferential movement of water and solutes in structured porous media". In: *Water Resources Research* 29.2, pp. 305–319. DOI: `https://doi.org/10.1029/92WR02339`. eprint: `https://agupubs.onlinelibrary.wiley.com/doi/pdf/10.1029/92WR02339`. URL: `https://agupubs.onlinelibrary.wiley.com/doi/abs/10.1029/92WR02339`.

Ghanbarian, Behzad et al. (2013). "Tortuosity in Porous Media: A Critical Review". In: *Soil Science Society of America Journal* 77.5, pp. 1461–1477. DOI: `https://doi.org/10.2136/sssaj2012.0435`. eprint: `https://acsess.onlinelibrary.wiley.com/doi/pdf/10.2136/sssaj2012.0435`. URL: `https://acsess.onlinelibrary.wiley.com/doi/abs/10.2136/sssaj2012.0435`.

Groos, Lisa (2013). "2D full waveform inversion of shallow seismic Rayleigh waves". PhD thesis. Karlsruher Institut für Technologie (KIT). DOI: `10.5445/IR/1000037320`.

Hu, Qi et al. (2021). "Direct updating of rock-physics properties using elastic full-waveform inversion". In: *Geophysics* 86.3, MR117–MR132. DOI: `10.1190/geo2020-0199.1`. eprint: `https://doi.org/10.1190/geo2020-0199.1`. URL: `https://doi.org/10.1190/geo2020-0199.1`.

Igel, Heiner (Nov. 2016). *Computational Seismology: A Practical Introduction.* Oxford University Press. ISBN: 9780198717409. DOI: `10.1093/acprof:oso/9780198717409.001.0001`. URL: `https://doi.org/10.1093/acprof:oso/9780198717409.001.0001`.

Johnson, David Linton, Joel Koplik, and Roger Dashen (1987). "Theory of dynamic permeability and tortuosity in fluid-saturated porous media". In: *Journal of Fluid Mechanics* 176, pp. 379–402. DOI: `10.1017/S0022112087000727`.

Köhn, Daniel (2011). "Time Domain 2D Elastic Full Waveform Tomography". en. PhD thesis. URL: `https://macau.uni-kiel.de/receive/diss_mods_00006786`.

Komatitsch, Dimitri and Roland Martin (2007). "An unsplit convolutional perfectly matched layer improved at grazing incidence for the seismic wave equation". In: *GEOPHYSICS* 72.5, SM155–SM167. DOI: `10.1190/1.2757586`. eprint: `https://doi.org/10.1190/1.2757586`. URL: `https://doi.org/10.1190/1.2757586`.

Kristek, Jozef, Peter Moczo, and Ralph J. Archuleta (2002). In: *Studia Geophysica et Geodaetica* 46.2, pp. 355–381. DOI: `10.1023/a:1019866422821`. URL: `https://doi.org/10.1023/a:1019866422821`.

Kurzmann, André (2012). "Applications of 2D and 3D full waveform tomography in acoustic and viscoacoustic complex media". PhD thesis. Karlsruher Institut für Technologie (KIT). DOI: `10.5445/IR/1000034421`.

Levander, Alan R. (1988). "Fourth-order finite-difference P-SV seismograms". In: *GEOPHYSICS* 53.11, pp. 1425–1436. DOI: `10.1190/1.1442422`. eprint: `https://doi.org/10.1190/1.1442422`. URL: `https://doi.org/10.1190/1.1442422`.

Liu, T. and T. Bohlen (2022a). "Mono-Parameter Poroelastic Fwi for the Reconstruction of the Shallow-Seismic Data". In: 2022.1, pp. 1–5. ISSN: 2214-4609. DOI:

https://doi.org/10.3997/2214-4609.202210532. URL: https://www.earthdoc.org/content/papers/10.3997/2214-4609.202210532.

– (Oct. 2022b). “Time-domain poroelastic full-waveform inversion of shallow seismic data: methodology and sensitivity analysis”. In: *Geophysical Journal International* 232.3, pp. 1803–1820. ISSN: 0956-540X. DOI: 10.1093/gji/ggac414. eprint: https://academic.oup.com/gji/article-pdf/232/3/1803/47028780/ggac414.pdf. URL: https://doi.org/10.1093/gji/ggac414.

Martin, Roland, Dimitri Komatitsch, and Abdelâziz Ezziani (2008). “An unsplit convolutional perfectly matched layer improved at grazing incidence for seismic wave propagation in poroelastic media”. In: *GEOPHYSICS* 73.4, T51–T61. DOI: 10.1190/1.2939484. eprint: https://doi.org/10.1190/1.2939484. URL: https://doi.org/10.1190/1.2939484.

Masson, Y. J., S. R. Pride, and K. T. Nihei (2006). “Finite difference modeling of Biot’s poroelastic equations at seismic frequencies”. In: *Journal of Geophysical Research: Solid Earth* 111.B10. DOI: https://doi.org/10.1029/2006JB004366. eprint: https://agupubs.onlinelibrary.wiley.com/doi/pdf/10.1029/2006JB004366. URL: https://agupubs.onlinelibrary.wiley.com/doi/abs/10.1029/2006JB004366.

Métivier, Ludovic et al. (Apr. 2014). “Multi-Parameter FWI - An Illustration of the Hessian Operator Role for Mitigating Trade-off between Parameter Classes”. In: *6th Saint Petersburg International Conference and Exhibition*. Saint Petersburg, Russia. DOI: 10.3997/2214-4609.20140196. URL: https://hal.archives-ouvertes.fr/hal-01887702.

Mittet, Rune (2002). “Free-surface boundary conditions for elastic staggered-grid modeling schemes”. In: *GEOPHYSICS* 67.5, pp. 1616–1623. DOI: 10.1190/1.1512752. eprint: https://doi.org/10.1190/1.1512752. URL: https://doi.org/10.1190/1.1512752.

Morency, Christina, Yang Luo, and Jeroen Tromp (Nov. 2009). “Finite-frequency kernels for wave propagation in porous media based upon adjoint methods”. In: *Geophysical Journal International* 179.2, pp. 1148–1168. ISSN: 0956-540X. DOI: 10.1111/j.1365-246X.2009.04332.x. eprint: https://academic.oup.com/gji/article-pdf/179/2/1148/5981840/179-2-1148.pdf. URL: https://doi.org/10.1111/j.1365-246X.2009.04332.x.

Morency, Christina and Jeroen Tromp (Oct. 2008). “Spectral-element simulations of wave propagation in porous media”. In: *Geophysical Journal International* 175.1, pp. 301–345. ISSN: 0956-540X. DOI: 10.1111/j.1365-246X.2008.03907.x. eprint: https://academic.oup.com/gji/article-pdf/175/1/301/5978976/175-1-301.pdf. URL: https://doi.org/10.1111/j.1365-246X.2008.03907.x.

Nocedal, Jorge and Stephen J. Wright (2006). *Numerical Optimization*. second. New York, NY, USA: Springer.

Operto, S. et al. (2013). “A guided tour of multiparameter full-waveform inversion with multicomponent data: From theory to practice”. In: *The Leading Edge* 32.9, pp. 1040–1054. DOI: `10.1190/tle32091040.1`. eprint: `https://doi.org/10.1190/tle32091040.1`. URL: `https://doi.org/10.1190/tle32091040.1`.

Pica, A., J. P. Diet, and A. Tarantola (1990). “Nonlinear inversion of seismic reflection data in a laterally invariant medium”. In: *GEOPHYSICS* 55.3, pp. 284–292. DOI: `10.1190/1.1442836`. eprint: `https://doi.org/10.1190/1.1442836`. URL: `https://doi.org/10.1190/1.1442836`.

Plessix, R.-E. (Nov. 2006). “A review of the adjoint-state method for computing the gradient of a functional with geophysical applications”. In: *Geophysical Journal International* 167.2, pp. 495–503. ISSN: 0956-540X. DOI: `10.1111/j.1365-246X.2006.02978.x`. eprint: `https://academic.oup.com/gji/article-pdf/167/2/495/1492368/167-2-495.pdf`. URL: `https://doi.org/10.1111/j.1365-246X.2006.02978.x`.

Pratt, R. Gerhard (1999). “Seismic waveform inversion in the frequency domain, Part 1: Theory and verification in a physical scale model”. In: *GEOPHYSICS* 64.3, pp. 888–901. DOI: `10.1190/1.1444597`. eprint: `https://doi.org/10.1190/1.1444597`. URL: `https://doi.org/10.1190/1.1444597`.

Pride, S. R., J. G. Berryman, and J. M. Harris (2004). “Seismic attenuation due to wave-induced flow”. In: *Journal of Geophysical Research: Solid Earth* 109.B1. DOI: `https://doi.org/10.1029/2003JB002639`. eprint: `https://agupubs.onlinelibrary.wiley.com/doi/pdf/10.1029/2003JB002639`. URL: `https://agupubs.onlinelibrary.wiley.com/doi/abs/10.1029/2003JB002639`.

Pride, Steven R., Anthony F. Gangi, and F. Dale Morgan (1992). “Deriving the equations of motion for porous isotropic media”. In: *The Journal of the Acoustical Society of America* 92.6, pp. 3278–3290. DOI: `10.1121/1.404178`. eprint: `https://doi.org/10.1121/1.404178`. URL: `https://doi.org/10.1121/1.404178`.

Queißer, Manuel and Satish C. Singh (2013). “Full waveform inversion in the time lapse mode applied to CO2 storage at Sleipner”. In: *Geophysical Prospecting* 61.3, pp. 537–555. DOI: `https://doi.org/10.1111/j.1365-2478.2012.01072.x`. eprint: `https://onlinelibrary.wiley.com/doi/pdf/10.1111/j.1365-2478.2012.01072.x`. URL: `https://onlinelibrary.wiley.com/doi/abs/10.1111/j.1365-2478.2012.01072.x`.

Russell, Brian H. (Jan. 1988). “1. Part 1 - Introduction”. In: *Introduction to Seismic Inversion Methods*. Society of Exploration Geophysicists, pp. 1–1–1–5. DOI: `10.1190/1.9781560802303.ch1`. URL: `https://doi.org/10.1190/1.9781560802303.ch1`.

Santos, Juan E. and Dongwoo Sheen (2007). “Finite Element Methods for the Simulation of Waves in Composite Saturated Poroviscoelastic Media”. In: *SIAM Journal on Numerical Analysis* 45.1, pp. 389–420. DOI: `10.1137/050629069`. eprint: `https://doi.org/10.1137/050629069`. URL: `https://doi.org/10.1137/050629069`.

Sheriff, R. E. and L. P. Geldart (1995). *Exploration Seismology.* 2nd ed. Cambridge University Press. DOI: `10.1017/CBO9781139168359`.

Sheriff, Robert E. (2002). *Encyclopedic Dictionary of Applied Geophysics.* 4th ed. Vol. 13. Geophysical References. Society of Exploration Geophysicists. ISBN: 0931830478. URL: `http://www.segdl.org/dictionary/`.

Tajuddin, M. (1984). "Rayleigh waves in a poroelastic half-space". In: *The Journal of the Acoustical Society of America* 75.3, pp. 682–684. DOI: `10.1121/1.390578`. eprint: `https://doi.org/10.1121/1.390578`. URL: `https://doi.org/10.1121/1.390578`.

Tarantola, A. (1984). "LINEARIZED INVERSION OF SEISMIC REFLECTION DATA*". In: *Geophysical Prospecting* 32.6, pp. 998–1015. DOI: `https://doi.org/10.1111/j.1365-2478.1984.tb00751.x`. eprint: `https://onlinelibrary.wiley.com/doi/pdf/10.1111/j.1365-2478.1984.tb00751.x`. URL: `https://onlinelibrary.wiley.com/doi/abs/10.1111/j.1365-2478.1984.tb00751.x`.

Tarantola, Albert (2005). *Inverse Problem Theory and Methods for Model Parameter Estimation.* Society for Industrial and Applied Mathematics. DOI: `10.1137/1.9780898717921`. eprint: `https://epubs.siam.org/doi/pdf/10.1137/1.9780898717921`. URL: `https://epubs.siam.org/doi/abs/10.1137/1.9780898717921`.

Tromp, Jeroen, Dimitri Komatitsch, and Qinya Liu (2008). "Spectral-element and adjoint methods in seismology". In: *Communications in Computational Physics* 3, pp. 1–32.

Virieux, J. (1984). "SH-wave propagation in heterogeneous media: velocity-stress finite-difference method". In: *Exploration Geophysics* 15.4, pp. 265–265. DOI: `10.1071/EG984265a`. eprint: `https://doi.org/10.1071/EG984265a`. URL: `https://doi.org/10.1071/EG984265a`.

Virieux, J., A. Asnaashari, et al. (2017). "6. An introduction to full waveform inversion". In: *Encyclopedia of Exploration Geophysics*, R1-1-R1–40. DOI: `10.1190/1.9781560803027.entry6`. eprint: `https://library.seg.org/doi/pdf/10.1190/1.9781560803027.entry6`. URL: `https://library.seg.org/doi/abs/10.1190/1.9781560803027.entry6`.

Virieux, J. and S. Operto (2009). "An overview of full-waveform inversion in exploration geophysics". In: *Geophysics* 74.6, WCC1–WCC26. DOI: `10.1190/1.3238367`. eprint: `https://doi.org/10.1190/1.3238367`. URL: `https://doi.org/10.1190/1.3238367`.

Virieux, Jean (1986). "P-SV wave propagation in heterogeneous media: Velocity-stress finite-difference method". In: *GEOPHYSICS* 51.4, pp. 889–901. DOI: `10.1190/1.1442147`. eprint: `https://doi.org/10.1190/1.1442147`. URL: `https://doi.org/10.1190/1.1442147`.

White, J. E. (Apr. 1975). "Computed seismic speeds and attenuation in rocks with partial gas saturation". In: *GEOPHYSICS* 40.2, pp. 224–232. ISSN: 0016-8033. DOI:

10.1190/1.1440520. eprint: https://pubs.geoscienceworld.org/geophysics/article-pdf/40/2/224/3156753/224.pdf. URL: https://doi.org/10.1190/1.1440520.

Wu, R. and K. Aki (1989). *Scattering and Attenuation of Seismic Waves, Part II*. Pageoph Topical Volumes. Birkhäuser Basel. ISBN: 9783034863636. URL: https://books.google.de/books?id=gBvyBwAAQBAJ.

Xu, Yixian, Jianghai Xia, and Richard D. Miller (2007). "Numerical investigation of implementation of air-earth boundary by acoustic-elastic boundary approach". In: *GEOPHYSICS* 72.5, SM147–SM153. DOI: 10.1190/1.2753831. eprint: https://doi.org/10.1190/1.2753831. URL: https://doi.org/10.1190/1.2753831.

Yang, Pengliang et al. (July 2016). "A review on the systematic formulation of 3-D multiparameter full waveform inversion in viscoelastic medium". In: *Geophysical Journal International* 207.1, pp. 129–149. ISSN: 0956-540X. DOI: 10.1093/gji/ggw262. eprint: https://academic.oup.com/gji/article-pdf/207/1/129/23641502/ggw262.pdf. URL: https://doi.org/10.1093/gji/ggw262.

Yang, Qingjie and Alison Malcolm (Dec. 2020). "Frequency domain full-waveform inversion in a fluid-saturated poroelastic medium". In: *Geophysical Journal International* 225.1, pp. 68–84. ISSN: 0956-540X. DOI: 10.1093/gji/ggaa579. URL: https://doi.org/10.1093/gji/ggaa579.

Yang, Qingjie, Alison Malcolm, et al. (Dec. 2018). "Analysis of radiation patterns for optimized full waveform inversion in fluid-saturated porous media". In: *Geophysical Journal International* 216.3, pp. 1919–1937. ISSN: 0956-540X. DOI: 10.1093/gji/ggy525. URL: https://doi.org/10.1093/gji/ggy525.

Zahradník, Jiří and Enrico Priolo (Mar. 1995). "Heterogeneous formulations of elastodynamic equations and finite-difference schemes". In: *Geophysical Journal International* 120.3, pp. 663–676. ISSN: 0956-540X. DOI: 10.1111/j.1365-246X.1995.tb01844.x. eprint: https://academic.oup.com/gji/article-pdf/120/3/663/2335513/120-3-663.pdf. URL: https://doi.org/10.1111/j.1365-246X.1995.tb01844.x.

Zeng, Y. Q., J. Q. He, and Q. H. Liu (2001). "The application of the perfectly matched layer in numerical modeling of wave propagation in poroelastic media". In: *GEOPHYSICS* 66.4, pp. 1258–1266. DOI: 10.1190/1.1487073. eprint: https://doi.org/10.1190/1.1487073. URL: https://doi.org/10.1190/1.1487073.

Zhang, Yu, Ping Ping, and Shuang-Xi Zhang (Mar. 2017). "Finite-difference modeling of surface waves in poroelastic media and stress mirror conditions". In: *Applied Geophysics* 14.1, pp. 105–114. DOI: 10.1007/s11770-017-0601-5.

Zhu, X. and G. A. McMechan (1991). "Numerical simulation of seismic responses of poroelastic reservoirs using Biot theory". In: *Geophysics* 56.3, pp. 328–339. DOI: 10.1190/1.1443047. eprint: https://doi.org/10.1190/1.1443047. URL: https://doi.org/10.1190/1.1443047.

A

Effects on Fréchet kernels

A.1. Effects of frequency

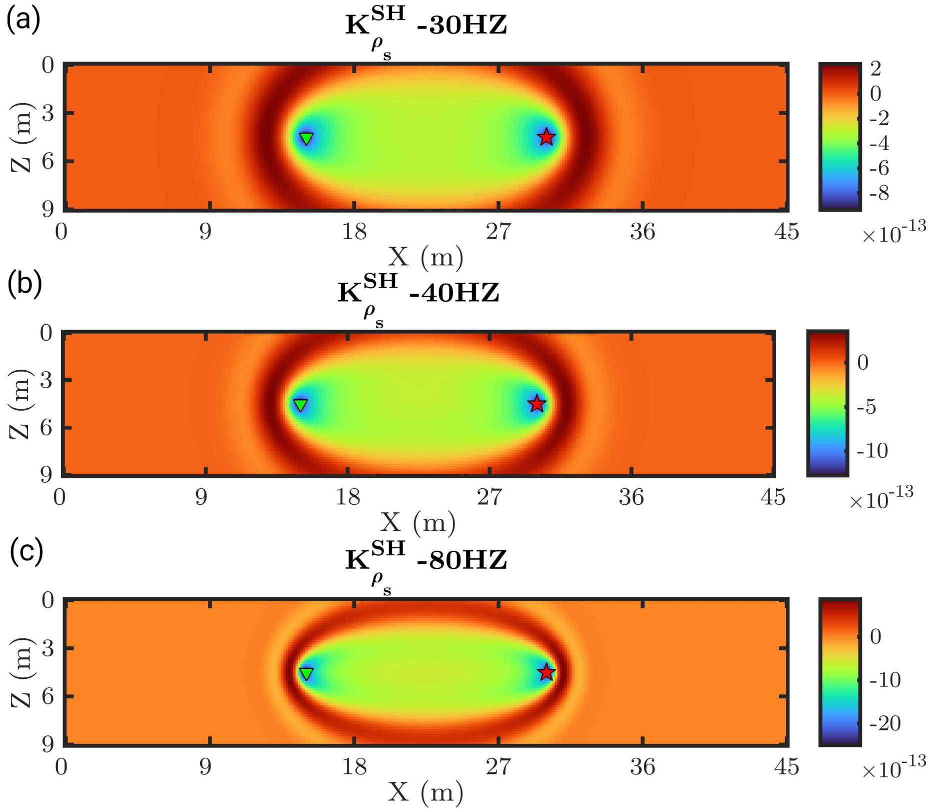

Figure A.1.: Fréchet kernels of solid grain density ρ_s in SH equations at different source frequencies: (a) 30 Hz; (b) 40 Hz; (c) 80 Hz.

Taking the Fréchet kernel of solid grain density as an example, the kernels are calculated from SH equations under different source frequencies. The red star represents the forward source, while the inverted triangle is the adjoint source. It shows clearly the width of the first Fresnel zone is getting narrower with increasing frequencies.

A.2. Kernels with/without surface waves

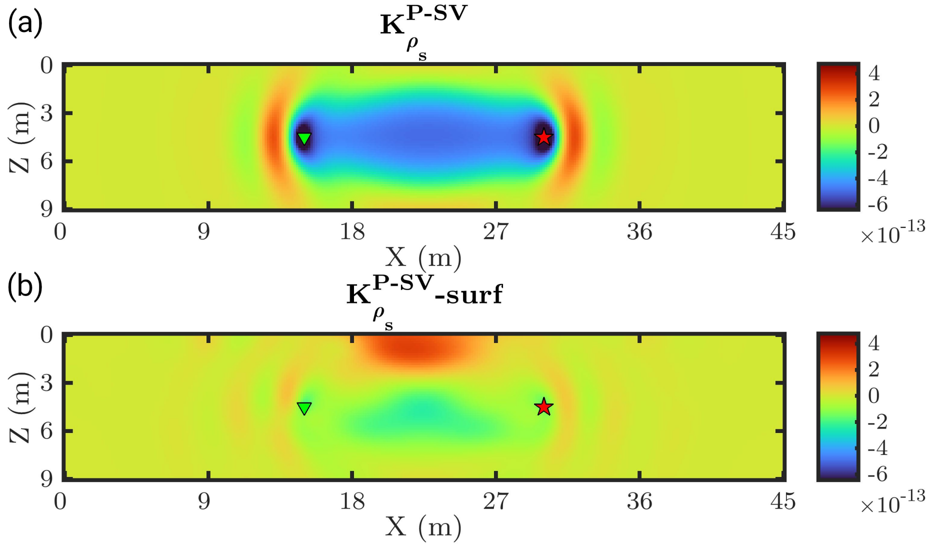

Figure A.2.: Fréchet kernels of solid grain density ρ_s in P-SV equations: (a) Without surface waves; (b) Containing Rayleigh waves.

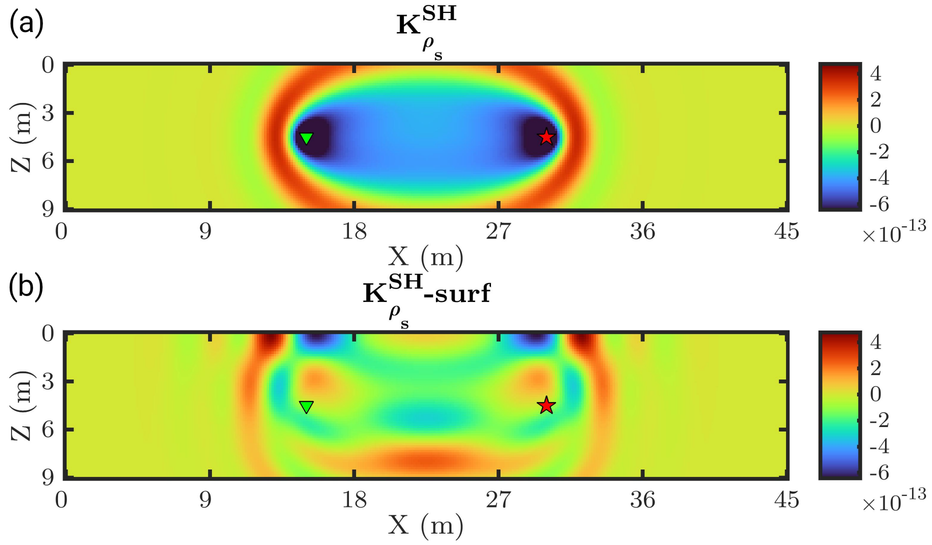

Figure A.3.: Fréchet kernels of solid grain density ρ_s in SH equations: (a) Without surface waves; (b) Containing Love wave.

B

Gradients tapering

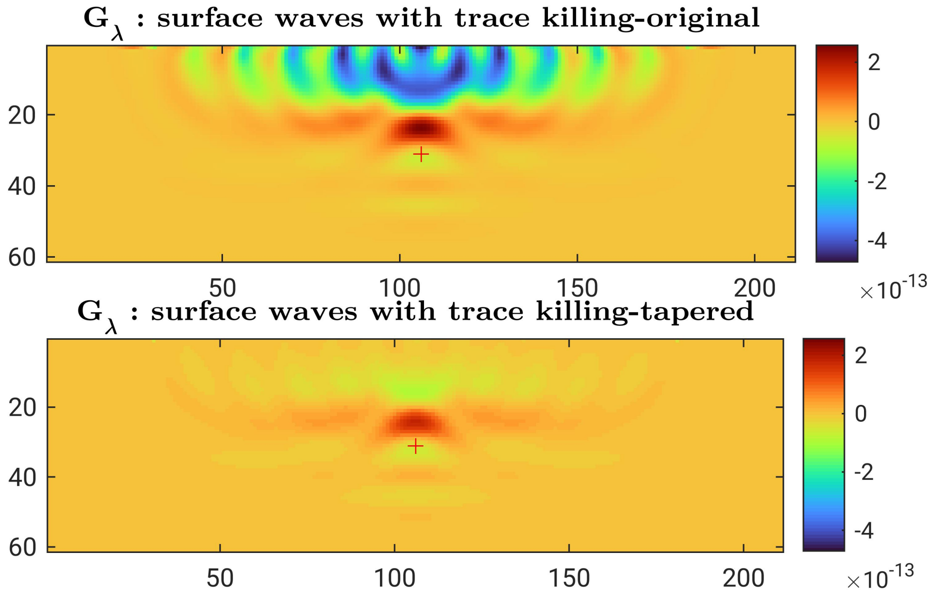

Figure B.1.: Comparisons of the gradients of λ in poroelastic P-SV equations before and after tapering.

For unnormalized objective function, there are strong wave energies around the forward sources during the gradients' integration in space, especially when surface waves are involved. These footprints will mislead the decent direction during iterations. To minimize these effects, a taper function can be applied source by source or after the gradient summation. Fig. B shows the gradient comparison before and after applying a circular taper function around the source after the shot summation, which shows the footprints around the source location are diminished.

C

Multi-stage strategy

As a local optimization problem, FWI will easily get stuck into a convergence towards local minima because of non-linearity. In this case, a multi-stage (also known as multi-scale) strategy is usually applied in FWI to mitigate the non-linearity issue (J. Virieux and Operto 2009). In poroelastic FWI, the non-linear problem will become severe with a more complex stress structure and increasing model parameters. As for the time-domain FWI, the multi-stage strategy is implemented by filtering seismic data by choosing optimal frequency bands. After filtering seismic waveforms with a low-pass filter, the wave number will decrease, and the cycle-skipping problem is alleviated so that FWI can achieve convergence stage by stage more easily (Boonyasiriwat et al. 2009; Bunks et al. 1995).

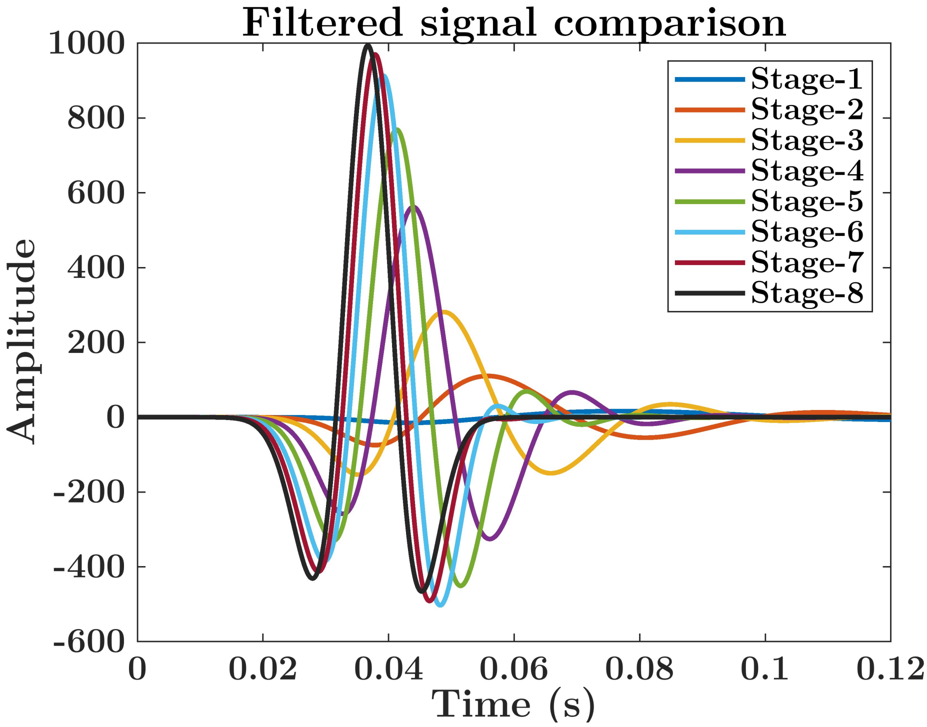

Figure C.1.: Filtered Ricker wavelet comparison: The central frequency of original signal is 45 Hz, and the corner frequencies from stage 1 to 8 are 10 Hz, 20 Hz, 30 Hz, 45 Hz, 60 Hz, 80 Hz, 100 Hz, 130 Hz.

In this thesis, the multi-stage strategy is applied to the numerical reconstruction tests in part IV. The seismic data are filtered by the 4th-order Butterworth low-pass filter with different corner frequencies. Fig. C.1 shows the waveform comparison of filtered signals with an 8-stage strategy 10-20-30-45-60-80-100-130 Hz. The corresponding frequency responses are given in Fig. C.2.

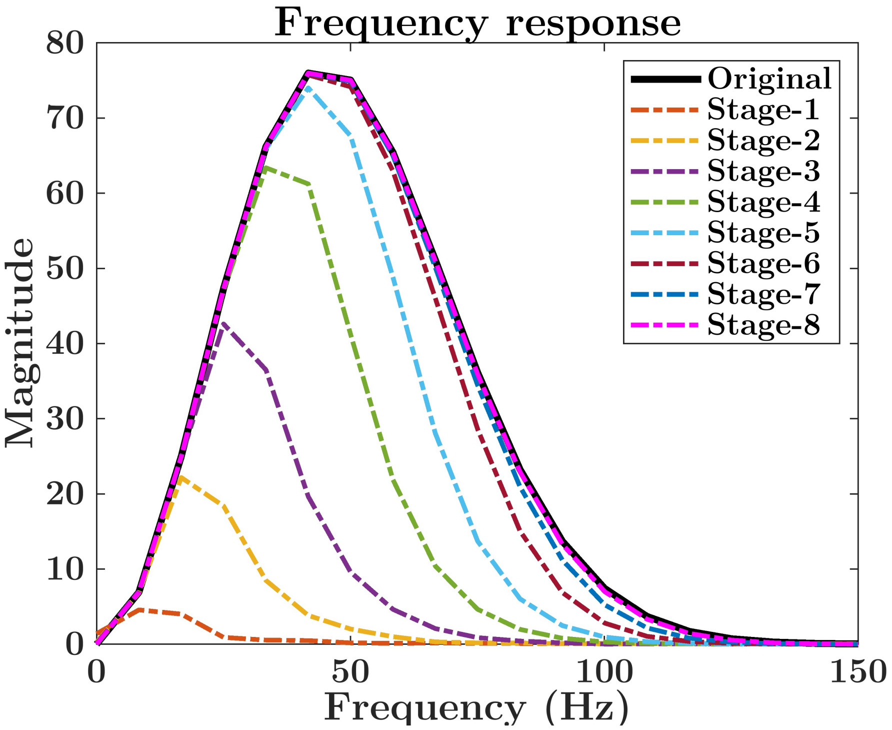

Figure C.2.: Frequency responses corresponding to the filtered signals in Fig. C.1.

D

Reconstruction test with/without surface waves

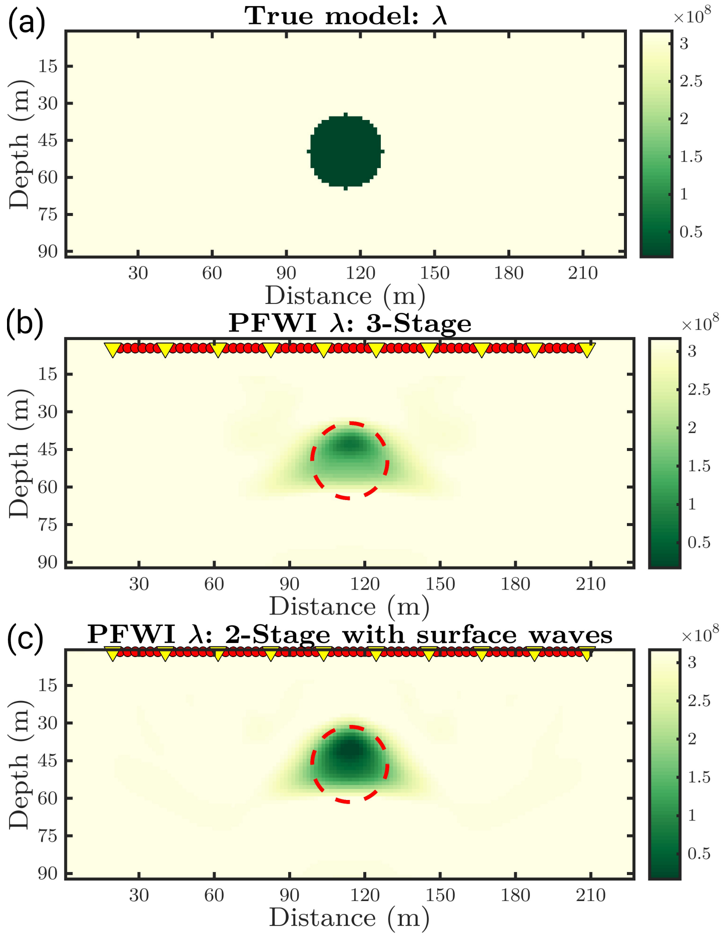

Figure D.1.: Poroelastic full-waveform inversion (PFWI) results of an anomaly body $\delta\lambda$: (a) True model; (b) Obtained λ without surface waves; (c) Obtained λ containing Rayleigh waves. The yellow invert triangles are sources, while the red circles represent receivers.

This chapter contains a simple anomaly reconstruction test, which compares the obtained results when surface waves are involved or not. The anomaly body is in the center of the poroelastic model. There are 10 shots on the top, while the Ricker wavelet with the center frequency of 10 Hz is set as the source signal.

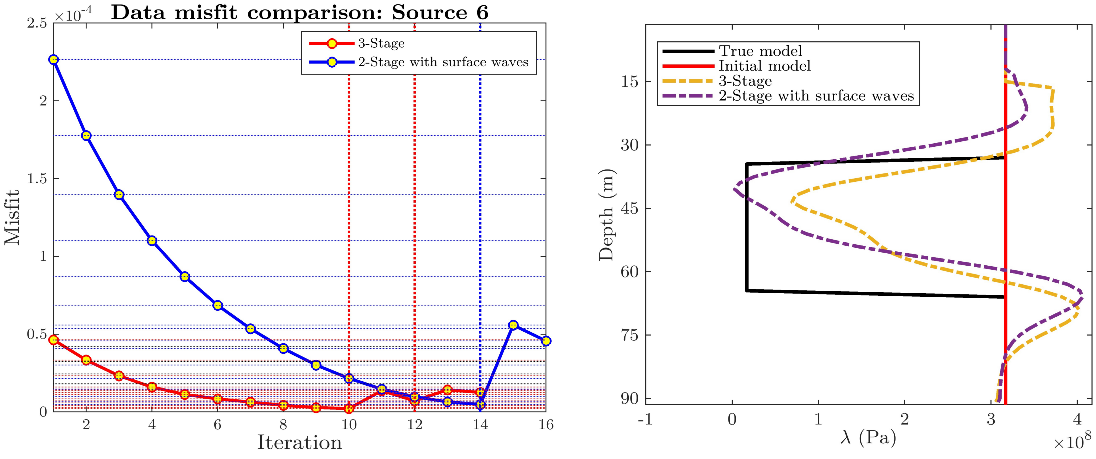

(a) Data misfit

(b) Log profiles

Figure D.2.: Single anomaly reconstruct results comparison with/without surface waves.

Taking the elastic modulus λ as an example, Fig. D.1 shows the PFWI results compared with the true model, and the initial model is a homogeneous poroelastic subsurface. Fig. D.1(b) gives the PFWI result with only body waves, and the applied frequency stages are 5 Hz-10 Hz-15 Hz. Similarly, When the frequency stage is only from 5 Hz to 15 Hz, Fig. D.1(c) is the corresponding Rayleigh wave PFWI result, which shows a better accuracy. A more intuitive comparison is in Fig. D.2(b), which is a log profile from the middle of the model. To be noticed in Fig. D.2(a), the data misfit will increase when surface waves are involved.

E

Effective velocities

The parameters and formulations for the calculation of the velocities in the poroelastic media are summarized below (Biot and Willis 1957; Dai, Vafidis, and Kanasewich 1995). The definition of the parameters has already been explained in chapter 3.

$$\begin{cases} P = [(1-\phi)(\alpha-\phi) + \frac{\phi K_d}{K_f}]M + \frac{4}{3}\mu \\ Q = \phi M(\alpha - \phi) \\ R = \phi^2 M \end{cases}, \tag{E.1}$$

$$\begin{cases} A' = T\phi\rho\rho_f - (-\phi\rho_f)^2 \\ B' = \rho R + T\phi\rho_f P + 2\phi\rho_f Q \\ C' = PR - Q^2 \end{cases}. \tag{E.2}$$

Then the velocity of the fast compressional wave

$$V_{fp} = \sqrt{\frac{B'^2 + \sqrt{B'^2 - 4A'C'}}{2A'}}, \tag{E.3}$$

the velocity of the slow compressional wave

$$V_{sp} = \sqrt{\frac{B'^2 - \sqrt{B'^2 - 4A'C'}}{2A'}}. \tag{E.4}$$

The fluid viscosity is absent in the non-dissipative case ($\eta = 0$) and then the shear wave velocity is (Deresiewicz 1960; Morency and Tromp 2008)

$$V_s = \sqrt{\frac{\mu}{\rho - \frac{\phi\rho_f}{T}}}. \tag{E.5}$$

List of Figures

3.1. Porous subsurface illustration 10

3.2. Implementation of different source types 13

3.3. Cartesian coordinate system and surface waves 14

3.4. Staggered grid and spatial position of variables in P-SV poroelastic equations 15

3.5. Staggered grid and spatial position of variables in SH poroelastic equations 17

3.6. Waveform comparisons of the synthetic data (in Fig. 3.7) and analytical solution of elastic wave equations. (a) Solid vertical velocity; (b) Solid horizontal velocity. 22

3.7. Snapshots of the shallow-seismic wavefields in homogeneous elastic subsurface when the point per minimum wavelength number is 56. The red cross is the source location and the inverted triangles are 38 receivers. 23

3.8. L2 norm error varied with offset and ppw number for comparisons of elastic results. 24

3.9. Poroelastic wavefields including surface waves at time = 0.24 s. The source locates at the free surface in the middle, and the horizontal distance is 1000 m. 26

3.10. Waveform comparison of the synthetic data obtained from $SPECFEM2D$ and $IforPoro$: solid vertical velocity VZ displayed in 11 traces. . . . 27

3.11. L2 norm error between the numerical results of SE and FD methods. 27

3.12. Snapshots of the poroelastic wavefields from $IforPoro$: (a) Horizontal velocity in solid phase; (b) Vertical velocity in fluid phase; (c) Horizontal velocity in fluid phase. 28

3.13. Synthetic data obtained from $IforPoro$: Solid velocity in Y direction. The sampling rate is 0.2 ms, and the duration time is 0.4 s. 29

3.14. L2 norm error between the numerical results of $IforPoro$ (Fortran 90), $SOFI2D - Sh$ (C language) and Matlab scripts. HAFDA is a method introduced in section 3.3.2.2 for free surface implementation, and SIM means stress image method. 30

5.1. Snapshots of the undisturbed shallow-seismic poroelastic PSV&SH wavefields at 90 ms: triggered by Ricker wavelet with a center frequency of 40 Hz. 49

5.2. Shallow-seismic scattered P-SV poroelastic wavefields (Solid profile in vertical direction Z) corresponding to different model parameters with 5% perturbations. The red star represents the location of the point diffractor. 50

5.3. Shallow-seismic scattered SH poroelastic wavefields (Solid profile in horizontal direction Y) corresponding to different model parameters with 5% perturbations. 51

5.4. Scattered single-trace waveform comparison from P-SV scheme: vertical-component velocity of the solid phase. The receiver is on the free surface at offset = 10.8 m in Fig. 5.2, and the black line represents the unperturbed reference waveform from the homogeneous poroelastic background at the same position. 52

5.5. Scattered single-trace waveform comparison from SH scheme: horizontal-component velocity of the solid phase. The receiver is on the free surface at offset = 10.8 m in Fig. 5.3, and the black line represents the unperturbed reference waveform from the homogeneous poroelastic background at the same position. 52

6.1. Fréchet kernels involving Rayleigh waves in P-SV for λ, K_s, and K_f: The red star is the location of the forward source, and the inverted triangle represents the adjoint source. Both are located at the free surface. 54

6.2. Fréchet kernels in SH & P-SV for μ, ρ_s, ρ_f, and ϕ: surface waves are involved. Geometry is the same as in Figure 6.1. 55

7.1. Acquisition geometry for a shallow poroelastic inclusion model. Horizontal Y component for SH equations is considered as well. . . 57

7.2. Gradient gallery in P-SV for correlation test in section 7.1: $\{\Delta\lambda, \Delta K_s, \Delta K_f\} \longrightarrow \{G_\lambda, G_{K_s}, G_{K_f}\}$ involving Rayleigh waves. The model geometry is shown in Fig. 7.1, and the parameters are listed in Table 5.1, which are the same as the followings. 58

7.3. Gradient gallery in P-SV for correlation test in section 7.1: $\{\Delta\lambda, \Delta K_s, \Delta K_f\} \longrightarrow \{G_\mu, G_{\rho_s}, G_{\rho_f}, G_\phi\}$ involving Rayleigh waves. 59

7.4. Gradient gallery in P-SV for correlation test in section 7.1: $\{\Delta\mu, \Delta\rho_s, \Delta\rho_f, \Delta\phi\} \longrightarrow \{G_\lambda, G_{K_s}, G_{K_f}\}$ involving Rayleigh waves. 59

7.5. Gradient panel in SH & P-SV for cross-comparison: $\Delta\mu \longrightarrow \{G_n, G_n^{SH}\}, n \in \{\mu, \rho_s, \rho_f, \phi\}$. 61

7.6. Gradient panel in SH & P-SV for cross-comparison: $\Delta\rho_s \longrightarrow \{G_n, G_n^{SH}\}, n \in \{\mu, \rho_s, \rho_f, \phi\}$. 61

7.7. Gradient panel in SH & P-SV for cross-comparison: $\Delta\rho_f \longrightarrow \{G_n, G_n^{SH}\}, n \in \{\mu, \rho_s, \rho_f, \phi\}$. 62

7.8. Gradient panel in SH & P-SV for cross-comparison: $\Delta\phi \rightarrow \{G_n, G_n^{SH}\}, n \in \{\mu, \rho_s, \rho_f, \phi\}$. 62

8.1. Inclusion model for mono-parameter inversion. 65
8.2. Reconstructed λ, K_s, K_f by Rayleigh wave PFWI. The red stars represent the source location, and invert triangles represent receivers, which are same as the follows. 67
8.3. Reconstructed $\mu, \rho_s, \rho_f, \phi$ by Rayleigh&Love wave PFWI. 67
8.4. Comparison of log profiles in the middle of the model. 68
8.5. Model misfit comparison. 69
8.6. Reconstructed λ, K_s, K_f by Rayleigh wave PFWI in a 3-layer model. 71
8.7. Data misfit changed with stages for (a) λ; (b) K_s; (c) K_f. 72
8.8. Comparisons of reconstructed μ by Rayleigh wave and Love wave PFWI. 72
8.9. Comparisons of reconstructed ρ_s by Rayleigh wave and Love wave PFWI. 73
8.10. Comparisons of reconstructed ρ_f by Rayleigh wave and Love wave PFWI. 73
8.11. Comparisons of reconstructed ϕ by Rayleigh wave and Love wave PFWI. 74
8.12. Comparison of log profiles in the middle of the model. 74
8.13. Data misfit changed with stages for $\mu, \rho_s, \rho_f, \phi$ during PSV/Rayleigh and SH/Love wave PFWI. 75

9.1. Cross-target model for multi-parameter reconstruction tests. 77
9.2. CTM snapshots at time=0.12 s of the forward shallow-seismic wavefields from the source location X=44.1 m: (a) Solid velocity in Z direction; (b) Solid velocity in Y direction; (c) Solid velocity in X direction; (d) Fluid velocity in Z direction; (e) Fluid velocity in X direction; (f) Fluid pressure. 79
9.3. Multi-parameter Rayleigh wave PFWI results from the parameter set (λ, K_s, K_f, μ, ρ_s, ρ_f, ϕ). 80
9.4. Data misfit changed with iterations. 80
9.5. Seismic profiles of solid Z component from the shot at x=20.1 m. . . 81
9.6. Multi-parameter Rayleigh wave PFWI results from the parameter set (λ, K_s, K_f). 82
9.7. Data misfit changed with iterations. 82
9.8. Multi-parameter Rayleigh wave PFWI results from the parameter set (λ, K_s, K_f, ϕ). 83
9.9. Data misfit changed with iterations. 83

9.10. Multi-parameter Rayleigh wave PFWI results from the parameter set (μ, ρ_s, ρ_f, ϕ). 84

9.11. Data misfit changed with iterations. 84

9.12. Multi-parameter Rayleigh wave PFWI results from the parameter set (λ, μ, ϕ). 85

9.13. Data misfit changed with iterations. 85

9.14. Multi-parameter Love wave PFWI results from the parameter set (μ, ρ_s, ρ_f, ϕ). 87

9.15. Data misfit changed with iterations. 87

9.16. Seismic profiles of solid Y component from the shot at x=20.1 m. . . 88

9.17. Multi-parameter Love wave PFWI results from the parameter set (ρ_s, ρ_f, ϕ). 89

9.18. Data misfit changed with iterations. 89

9.19. Multi-parameter Love wave PFWI results from the parameter set (μ ϕ). 90

9.20. Data misfit changed with iterations. 90

10.1. Comparison of reconstructed μ by Love wave PFWI and EFWI. . . . 92

10.2. Comparisons of log profiles in the middle of the model for reconstructed μ and V_s. 92

10.3. Seismic data comparison of Love wave PFWI and EFWI. 93

A.1. Fréchet kernels of solid grain density ρ_s in SH equations at different source frequencies: (a) 30 Hz; (b) 40 Hz; (c) 80 Hz. 109

A.2. Fréchet kernels of solid grain density ρ_s in P-SV equations: (a) Without surface waves; (b) Containing Rayleigh waves. 110

A.3. Fréchet kernels of solid grain density ρ_s in SH equations: (a) Without surface waves; (b) Containing Love wave. 110

B.1. Comparisons of the gradients of λ in poroelastic P-SV equations before and after tapering. 111

C.1. Filtered Ricker wavelet comparison: The central frequency of original signal is 45 Hz, and the corner frequencies from stage 1 to 8 are 10 Hz, 20 Hz, 30 Hz, 45 Hz, 60 Hz, 80 Hz, 100 Hz, 130 Hz. 113

C.2. Frequency responses corresponding to the filtered signals in Fig. C.1. 114

D.1. Poroelastic full-waveform inversion (PFWI) results of an anomaly body $\delta\lambda$: (a) True model; (b) Obtained λ without surface waves; (c) Obtained λ containing Rayleigh waves. The yellow invert triangles are sources, while the red circles represent receivers. 115

D.2. Single anomaly reconstruct results comparison with/without surface waves. 116

List of Tables

3.1. Modeling parameters used for elastic benchmarking in section 3.4.1. The source signal is Ricker wavelet. 21
3.2. Modeling parameters used for poroelastic benchmarking in section 3.4.1 (Morency and Tromp 2008). 25
3.3. Modeling parameters used for SH forward solver benchmarking in section 3.4.2. The source signal is Ricker wavelet with the central frequency of 30 Hz. 29

5.1. Rock properties of the fluid-saturated porous medium for analyzing parameter sensitivities. 48

8.1. Poroelastic parameters of the anomaly. 66
8.2. Poroelastic parameters of the true 3-layer model. 70

9.1. CTM parameters used for multi-parameter reconstruction tests in chapter 9. 78

Acknowledgement

【夫夷以近，则游者众；险以远，则至者少。而世之奇伟、瑰怪，非常之观，常在于险远，而人之所罕至焉，故非有志者不能至也。】

——北宋·王安石《游褒禅山记》

The quote above comes from the reminiscence of the literary master in the Northern Song Dynasty, Wang, Anshi, "A Journey to Baochan Mountain" in A.D.1054.

Doing a Ph.D. is like a journey climbing mountains. With the end approaching, I would like to express my sincere thanks to the people help me finish my "journey". First and foremost, I would like to express my deepest gratitude to my supervisor Prof. Thomas Bohlen, who provides me with a professional and free research platform. His profound insights have benefited me a lot in the discussions we had. He always supports me in following my ideas and gives me encouragement. Without his remarkable guidance, I wouldn't have gone so far. Likewise, I am extremely grateful to Prof. Erik H. Sänger, who would like to spend time reviewing my thesis. It has been a great experience to talk with Erik at the poroelasticity minisymposium in Bochum.

So many thanks to Thomas Hertweck, Michael Frietsch, and Laura Gaßner, for their continuing IT support and management. I am also sincerely grateful to Claudia for her kind help with many document affairs.

Furthermore, I would like to thank all former and current members of our AG group: Niko, Tilman, Mark, Renat, Yudi, Lars, Sonia, and many others. I am lucky to be familiar with and work with you. I hope you are all in good fortune.

At last, I will give my deepest thanks to my mom. Every further progress I made is half due to her, at least. A special thanks to Jincheng Ma for his consistent companion. The transport tickets between Munich and Karlsruhe will be our treasured memory in Germany. Besides, China Scholarship Council is acknowledged for the financial support (No. CSC201806170055).